Diss. ETH No. 28251

Osteocyte Lacunar Biomarkers in Human Rare Bone Diseases

A thesis submitted to attain the degree of

DOCTOR OF SCIENCES of ETH ZURICH

(Dr. sc. ETH Zurich)

presented by

Elliott Goff

M.Sc. Mechanical Engineering, University of Missouri – Kansas City

born on 12.12.1990

citizen of the United States of America

accepted on the recommendation of

Prof. Dr. Ralph Müller, examiner

Prof. Dr. Adi Cohen, co-examiner

2022

“Patience and persistency always pays off”

-Reda Elghoul

© 2022 Elliott Goff

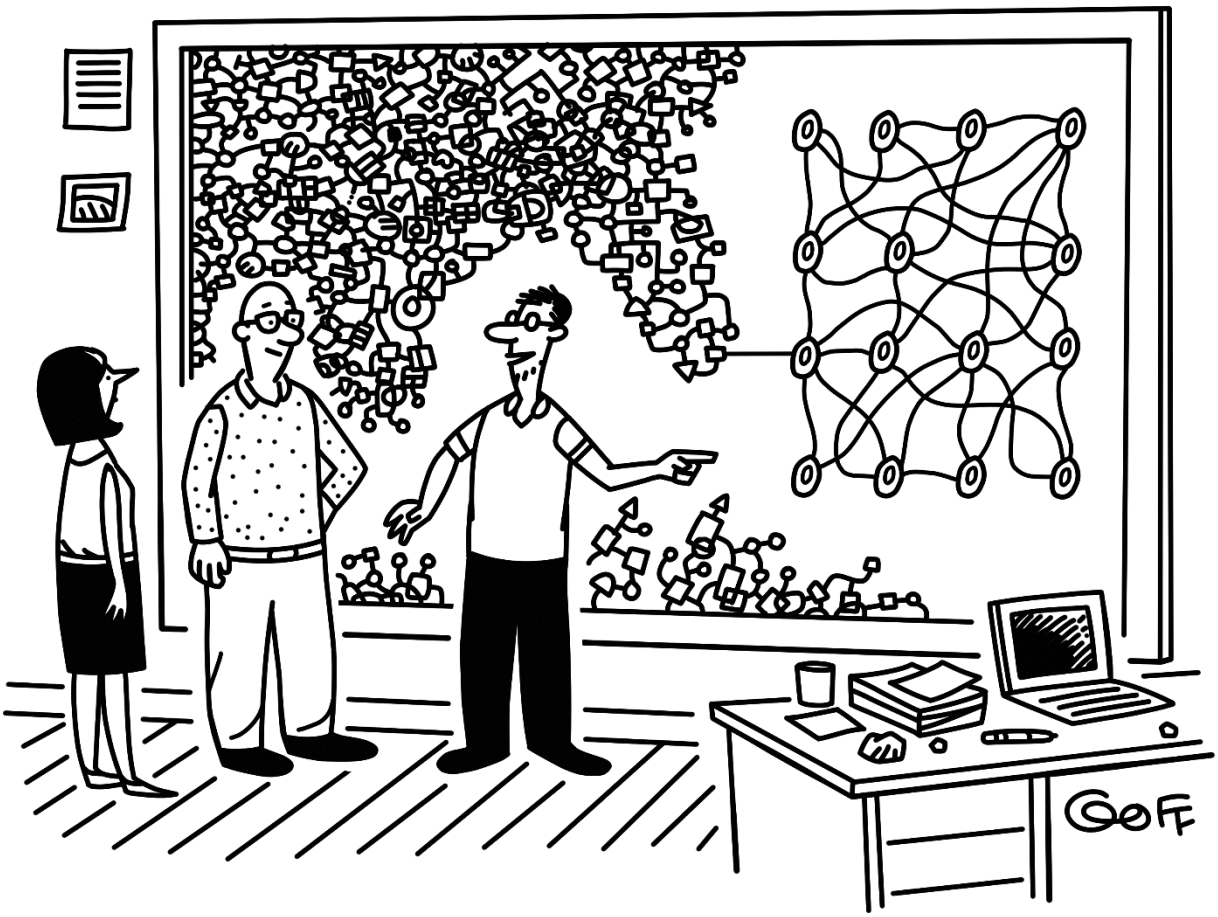

"And this was when I developed my lacunar analysis."

Table of Contents

Acknowledgements i

Summary v

Zusammenfassung ix

1 Introduction 1

1.1 Thesis motivation 2

1.2 Specific aims 4

1.3 Thesis outline 5

2 Background 11

2.1 Large-scale lacunar imaging and quantification 12

2.2 Lacunar mechanics and microcracking 18

2.3 Clinical importance 21

3 Imaging and quantification of osteocyte lacunar biomarkers 37

3.1 A novel shape filter for lacunar imaging in human bone using ultra-high-resolution desktop micro-CT 38

3.2 Large-scale quantification of human osteocyte lacunar morphological biomarkers as assessed by ultra-high-resolution desktop micro-computed tomography 47

3.3 Towards *in silico* biomechanical evaluation of microcracking and osteocyte lacunar biomarkers 85

4 Osteocyte lacunar biomarkers for the characterization of human rare bone diseases 108

4.1 Large-scale osteocyte lacunar morphological analysis of transiliac bone in normal and osteoporotic premenopausal women 109

4.2 Investigation of clinical adiposity using lacunar biomarkers 133

5 Synthesis **156**

5.1. Background 157

5.2 Main findings and implications 159

5.3 Limitations and future research 162

5.4 Conclusion 165

Curriculum Vitae **175**

Acknowledgements

The work presented in this thesis would not have been possible without the support from a number of people. I would like to express my profound gratitude to them.

First and foremost, I would like to thank Prof. Dr. Ralph Müller for giving me the opportunity to work at the Institute for Biomechanics in his Laboratory for Bone Biomechanics. His enthusiasm, motivation, and especially his ability to generate solutions through discussion have been inspirational throughout my years at the institute. I greatly appreciated his support, guidance, and experience, which have been enlightening, not only for my PhD but also in the greater context of life.

Special thanks to my team lead Dr. Gisela Kuhn, whose advice and reassurance has been invaluable in the latter half of my PhD journey. Thank you for all your inputs on my manuscripts, this thesis, and for keeping the biology side of the research present in my mind. Navigating the PhD was a difficult journey fraught with insecurities; thank you for keeping me calm and reminding me that my efforts are valued. We have been a solid team the past few years and I'll truly miss our camaraderie.

Thanks to Prof. Dr. Adi Cohen for being my co-referee and for her insightful discussions on the clinical relevance of this thesis. Our conversations were always a breath of fresh air for me. When I was locked into the technical shortcomings of my thesis, you always reminded me how important and valuable my work was for the patients and for creating a better understanding for rare bone conditions.

Thank you to Peter Schwilch for assisting with sample preparation and creating the custom engineering designs which allowed successful image acquisition. Big thanks to Dr. Tor Hildebrand, Andreas Bilger, and Peter Suter for their collaboration and help analyzing my large datasets by integrating my code into their XamFlow software.

Thanks to Francesco Vicintini, Federica Buccino, Chiara Bregoli, Alessandro Stagni, and Basil Aeppli who successfully completed their masters' theses under my supervision as well as Jonathan McKinley, Sebastian Zanner, Yvo Goette, Yujia Wang, and Sarthak Counsil who also succeeded with their projects and by doing so, improved the breadth and depth of this thesis.

Over my seven and a half years at the institute I've had the privilege of meeting and working with many brilliant individuals. I'd like to thank Dr. Sandro Badilatti, Dr. Duncan Tourolle, Dr. Patrik Christen, Dr. Jianhua Zhang, Dr. Graeme Paul, and Francisco Correia for being excellent office mates and companions over the years. Many of the ideas in this thesis stem from our insightful coffee-break and lunch discussions. Thank you to my senior PhD colleagues, Dr. Marios Georgiadis, Dr. Alina Levchuk, Dr. Zihui Li, Dr. Andreas Trüssel, Dr. Jolanda Vetsch, Dr. Carly Taylor, Dr. Alex Zwahlen, Dr. Sandro Badilatti, Dr. Niklas Ignasiak, and Dr. Duncan Tourolle, for their guidance and passing the torch to my PhD generation and contemporaries Dr. Felicitas Flohr, Dr. Nicholas Ohs, Dr. Graeme Paul, Dr. Gian Schaedli, Dr. Ariane Scheuren, Dr. Jianhua Zhang, of whom I am the youngest, and we now hand over to Daniele Boaretti, Francisco Correia, Christian Gehre, Wanwan Qiu, Matthias Walle, Jack Kendall, Doris Zauchner, Anke de Leeuw, Julia Griesbach, Charles Ledoux, and Dilara Yilmaz. I am confident in all of you and look forward to your achievements. Your patience and persistency will pay off.

Thank you to Prof. Dr. Stephen Ferguson and his group for accepting me as their "adopted" PhD child. I would always look forward to after-lunch espressos with Dr. Dmitriy Alexeev, Dr. Enrico De Pieri, Dr. Fabio D'Isidoro, Dr. Ingmar Fleps, Dr. Elena Cambria, Dr. William Enns-Bray, Dr. Aleksandra Sadowska, Pascal Behm, Dr. Dominika Ignasiak, Dr. Thomas Zumbrunn, Matthias Santschi, Jaka Pižorn, Thijs Smit, Stephanie Huber, Xiaoyu Du, Alexander Baker, Johanna Menze, and Elisa Bissacco.

A special thank you to Prof. Dr. Amber Rath Stern, Prof. Dr. Lynda Bonewald, and Prof. Dr. Gregory King for opening me to the exciting world of biomedical engineering and allowing me to stand on their shoulders to reach ETH.

I am forever indebted to Dr. Sandro Badilatti who originally convinced me to undertake a PhD at ETH. He has mentored me not only in the PhD and ETH but he has also been my guide through life in Switzerland and integrating with Swiss culture.

Furthermore, I'd like to thank Frischholz and Beast Jungs & Maedli for the friendship, skateboarding, and always patiently speaking German with me. For me the PhD journey was one step back, two steps forward, and allowing my brain to focus elsewhere with you all was important for my sanity.

I cannot express gratitude enough to my mother and father, Christine Droll and Ted Goff, who have molded me into the thoughtful human I have become today and for giving me the freedom to follow my own path. Thank you to my grandmother, Mary Droll, who has nurtured me over the decades through positivity and love. Thank you to my grandfather, Prof. Dr. Henry Droll, who first introduced me to the magical world of science as a child. Thank you to my Feighny and Campana cousins who are more like brothers and sisters to me. Thank you to my Droll aunties who were formative elements of my education during lively debates at Sunday family dinners. Thank you to Pius Sidler and Victor Escobar for the continuation of these educational dinners, including me in their lives, and making me feel like family when mine is so far away.

Finally, I would like to thank my partner, Lucia Sidler, who has stood by my side through thick and thin. Her unwavering support, affection, and love have carried me through the darkest times of my PhD journey and celebrated me in the moments of success. Thank you to her parents, Teresa and Thomas Sidler, for raising such a kind and loving daughter.

Zürich, February 2022

Elliott Goff

Summary

Osteoporosis is a metabolic disease that is characterized by an increased risk of skeletal fracture. While typically occurring in postmenopausal women, rare forms of the disease also manifest in younger premenopausal women such as idiopathic osteoporosis (IOP) and idiopathic low bone mineral density (ILBMD). The weakening of the skeletal system and subsequent increased fracture risk can be explained by a reduction of overall bone density as well as changes in the bone tissue microarchitecture. However, open questions remain regarding if and how the disease impacts bone on a cellular level – specially with respect to the morphology of the lacunar pores and their resident osteocytes. With recent developments in ultra-high-resolution micro-computed tomography (microCT), it is now possible to image embedded three-dimensional (3D) structures with a resolution on the order of one micrometer. This technology is uniquely positioned to image the cellular structures of ex-vivo bone biopsies, such as lacunae, with the resolution and scale of synchrotron computed tomography (SR-CT) without requiring an entire beamline facility. However, a rigorously validated methodology to image lacunar pores using ultra-high-resolution microCT remains to be developed.

Therefore, this thesis has been divided into three aims: (i) To develop a method to perform large-scale quantification of osteocyte lacunar morphological biomarkers (ii) To develop a method for the *in silico* quantification of osteocyte lacunar mechanical biomarkers (iii) To create osteocyte lacunar biomarkers for the characterization of human rare bone diseases.

With respect to the first aim, a method was developed to image, extract, and measure lacunar morphometries. First, a novel sample preparation methodology was developed to machine embedded human bone biopsies into a cylindrical format that fits within the physical constraints of the microCT device. Image acquisition was next optimized to create high quality images with clearly visible lacunae, which involved parameters such as x-ray beam energy and filter selection. Following image acquisition, a sample-specific imaging threshold was then applied to binarize the image and segment lacunar structures. Finally, 3D morphometric parameters were measured in both cortical and trabecular regions of a group of 31 transiliac biopsies originating from healthy premenopausal women. Lacunar morphometric parameters were categorized as global, local, and population-based measurements. Rigorous validation was performed for the entire methodology and included measures of lacunar detection accuracy

(true positives (TP), false positives (FP), false negatives (FN)), reproducibility (precision error (PE) and intraclass correlation coefficients (ICC)), and biological sensitivity (detectible lacunar differences between regions of cortical and trabecular bone).

The second aim investigated the biomechanical significance of the embedded lacunar structures. Two computational models were created that simulate microcrack initiation and propagation through mineralized bone tissue, which ultimately intersected several lacunae. These models were constructed by combining the microCT image data with micro-finite element analysis (microFE). The first model, called the microcrack gradient model (MGM), was based purely on 3D mechanical gradients derived from the original microCT image density values. The second model, named the scissor model (SM), explored the hypothetical release of interstitial fluid from the dense network of canaliculi as a microcrack propagates through the tissue matrix. Both models had unique advantages and disadvantages, however, the microcracking simulated with the SM resembled previous experimental results more closely than with the MGM.

The third and final aim of this thesis was to apply the validated imaging methodology developed in the first aim to a large set (103 in total) of three cohorts of transiliac bone biopsies: healthy cohort (n=39), IOP cohort (n=45), and ILBMD cohort (n=19). This was a true large-scale application of the imaging methodology, and the analysis included a total of 26.2 million lacunae. While lacunar morphometries did not significantly differ between cohorts, lacunae in cortical bone were significantly larger, flatter, and more densely packed together than in trabecular regions. This data corroborated the results of the lacunae examined in the first aim, which displayed the same trend of lacunar morphometries between regions in a healthy cohort. Across all three cohorts, lacunar sphericity was strongly negatively correlated with bone volume (BV/TV). While only a cross-sectional study, this strong correlation indicates that lacunar morphology is indeed connected with BV/TV. Finally, the same analysis was applied to the healthy cohort (n=39), but grouped according to adiposity (n_{low} = 13, n_{mid} = 14, n_{high} = 12). Similar to the first biopsy grouping, lacunar morphology differed between cortical and trabecular regions, but not between adiposity tertiles. Furthermore, a strong negative correlation persisted regarding lacunar sphericity and BV/TV.

To conclude, the application of the large-scale lacunar imaging methodology using microCT was successful and improved our understanding of lacunar morphology in premenopausal women suffering from rare forms of osteoporosis. Firstly, the imaging methodology was

demonstrated to be able to measure lacunar morphometries accurately, reproducibly, and sensitively in human transiliac bone biopsies using microCT technology. Secondly, the biomechanical importance of lacunar structures in the mineralized bone matrix with respect to simulated microcracking was explored and the importance of the canalicular network was highlighted. Finally, the validated lacunar imaging methodology was applied to both healthy vs. affected cohorts (healthy, IOP, ILBMD) as well as to the healthy cohort alone but divided into tertiles based on adiposity. Ultimately, the development, validation, and application of this large-scale lacunar imaging methodology using widely accessible microCT technology has two main accomplishments: it has revealed new insights into the lacunar morphology of premenopausal women with rare forms of osteoporosis and it has also empowered researchers with access to microCT systems to explore additional hypotheses related to lacunar morphology.

Zusammenfassung

Osteoporose ist eine metabolische Erkrankung, die durch ein erhöhtes Risiko für Knochenbrüche gekennzeichnet ist. In der Regel tritt sie bei Frauen nach der Menopause auf, jedoch manifestieren sich seltene Formen der Krankheit auch bei jüngeren Frauen vor der Menopause, wie die idiopathische Osteoporose (IOP) und die idiopathische niedrige Knochenmineraldichte (ILBMD). Die Schwächung des Skelettsystems und das damit verbundene erhöhte Frakturrisiko lassen sich durch eine Verringerung der Gesamtknochendichte sowie durch Veränderungen der Mikroarchitektur des Knochengewebes erklären. Es bleiben jedoch Fragen offen, ob und wie sich die Krankheit auf zellulärer Ebene auf den Knochen auswirkt - insbesondere im Hinblick auf die Morphologie der lakunären Poren und der darin lebenden Osteozyten. Mit den jüngsten Entwicklungen in der ultrahochauflösenden Mikro-Computertomographie (mikroCT) ist es nun möglich, eingebettete dreidimensionale (3D) Strukturen mit einer Auflösung in der Größenordnung von einem Mikrometer abzubilden. Diese Technologie ist in der Lage, die zellulären Strukturen von Ex-vivo-Knochenbiopsien, wie z. B. Lakunen, mit der Auflösung und dem Maßstab der Synchrotron-Computertomographie (SR-CT) abzubilden, ohne dass eine ganze Beamline-Anlage erforderlich ist. Eine rigoros validierte Methodik zur Abbildung von Lakunenporen mittels ultrahochauflösender Mikro-CT muss jedoch erst noch entwickelt werden.

Deshalb wurde diese Arbeit in drei Ziele unterteilt: (i) Entwicklung einer Methode zur großmaßstäblichen Quantifizierung von morphologischen Biomarkern für Lakunen (ii) Entwicklung einer Methode zur In-silico-Quantifizierung von mechanischen Biomarkern für Lakunen (iii) Entwicklung von Biomarkern für Lakunen zur Charakterisierung seltener menschlicher Knochenerkrankungen.

In Bezug auf das erste Ziel wurde eine Methode zur Abbildung, Extraktion und Messung der Morphometrie von Lakunen entwickelt. Zunächst wurde eine neuartige Probenvorbereitungsmethode entwickelt, um eingebettete menschliche Knochenbiopsien in ein zylindrisches Format zu bringen, das in die räumlich beschränkte Probenkammer des mikroCT-Geräts passt. Anschließend wurde die Bildaufnahme optimiert, um qualitativ hochwertige Bilder mit deutlich sichtbaren Lakunen zu erzeugen, wobei Parameter wie die Röntgenstrahlenenergie und die Filterauswahl berücksichtigt wurden. Nach der Bildaufnahme

wurde ein für jede Probe spezifischer Schwellenwert angewendet, um das Bild zu binarisieren und die Lakunenstrukturen zu segmentieren. Schließlich wurden die morphometrischen 3D-Parameter sowohl in den kortikalen als auch in den trabekulären Regionen einer Gruppe von 31 transiliakalen Biopsien von gesunden prämenopausalen Frauen gemessen. Die lakunären morphometrischen Parameter wurden als globale, lokale und populationsbasierte Messungen kategorisiert. Die gesamte Methodik wurde einer strengen Validierung unterzogen und umfasste Messungen der Erkennungsgenauigkeit von Lakunen (echte Positive (TP), falsch Positive (FP), falsch Negative (FN)), der Reproduzierbarkeit (Präzisionsfehler (PE) und Intraclass-Korrelationskoeffizienten (ICC)) und der biologischen Sensitivität (nachweisbare Uunterschiede der Lakunen zwischen Regionen aus kortikalem und trabekulärem Knochen).

Das zweite Ziel war die Untersuchung der biomechanischen Bedeutung der eingebetteten lakunären Strukturen. Es wurden zwei Berechnungsmodelle erstellt, die die Entstehung und Ausbreitung von Mikrorissen im mineralisierten Knochengewebe simulieren, welche schließlich mehrere Lakunen durchschnitten. Diese Modelle wurden durch Kombination der mikroCT-Bilddaten mit der Finite-Elemente-Mikroanalyse (mikroFE) erstellt. Das erste Modell, das so genannte Mikroriss-Gradienten-Modell (MGM), basierte ausschließlich auf mechanischen 3D-Gradienten, die aus den ursprünglichen Dichtewerten der mikroCT-Bilder abgeleitet wurden. Das zweite Modell, das so genannte Scherenmodell (SM), untersuchte die hypothetische Freisetzung von interstitieller Flüssigkeit aus den dendritischen Kanälchen des dichten Netzwerks, wenn sich ein Mikroriss durch die Gewebematrix ausbreitet. Beide Modelle hatten eindeutige Vor- und Nachteile, doch die mit dem SM simulierten Mikrorisse ähnelten früheren experimentellen Ergebnissen mehr als die des MGM.

Das dritte und letzte Ziel dieser Arbeit war die Anwendung der validierten Bildgebungsmethode, die im ersten Ziel entwickelt wurde, auf eine grosse Probenmenge (insgesamt 103) von drei Kohorten von transiliakalen Knochenbiopsien: gesunde Kohorte (n=39), IOP-Kohorte (n=45) und ILBMD-Kohorte (n=19). Dabei handelte es sich um eine wirklich groß angelegte Anwendung der Bildgebungsmethode, und die Analyse umfasste insgesamt 26,2 Millionen Lakunen. Während sich die Morphometrien der Lakunen zwischen den Kohorten nicht signifikant unterschieden, waren die Lakunen im kortikalen Knochen signifikant größer, flacher und dichter gepackt als in trabekulären Regionen. Diese Daten bestätigten die Ergebnisse zu den im Rahmen des ersten Ziels untersuchten Lakunen, die in einer gesunden Kohorte denselben Trend der Lakunenmorphometrie zwischen den Regionen

aufwiesen. In allen drei Kohorten war die lakunäre Sphärizität stark negativ mit dem Knochenvolumen (BV/TV) korreliert. Obwohl es sich nur um eine Querschnittsstudie handelt, deutet diese starke Korrelation darauf hin, dass die Lakunenmorphologie tatsächlich mit dem BV/TV zusammenhängt. Schließlich wurde dieselbe Analyse auf die gesunde Kohorte (n=39) angewandt, jedoch gruppiert nach Adipositas (n_{low} = 13, n_{mid} = 14, n_{high} = 12). Ähnlich wie bei der ersten Biopsiegruppierung unterschied sich die Lakunarmorphologie zwischen kortikalen und trabekulären Regionen, jedoch nicht zwischen den Tertilen der Adipositas. Außerdem bestand eine starke negative Korrelation zwischen der Sphärizität der Lakunen und dem BV/TV.

Zusammenfassend lässt sich sagen, dass die Anwendung der groß angelegten Bildgebungsmethode für Lakunen mittels mikroCT erfolgreich war und unser Verständnis der Lakunenmorphologie bei prämenopausalen Frauen, die an seltenen Formen der Osteoporose leiden, verbessert hat. Erstens konnte gezeigt werden, dass die Bildgebungsmethode in der Lage ist, die Lakunenmorphologie in menschlichen transiliakalen Knochenbiopsien mit der mikroCT-Technologie genau, reproduzierbar und empfindlich zu messen. Zweitens wurde die biomechanische Bedeutung von lakunären Strukturen in der mineralisierten Knochenmatrix im Hinblick auf simulierte Mikrorisse untersucht. Schließlich wurde die validierte Bildgebungsmethode für lakunäre Strukturen sowohl auf gesunde und erkrankte Kohorten (gesund, IOP, ILBMD) als auch auf die gesunde Kohorte allein, jedoch unterteilt in Tertile auf der Grundlage der Adipositas, angewendet. Letztendlich erbrachte die Entwicklung, Validierung und Anwendung dieser groß angelegten Lakunan-Imaging-Methode unter Verwendung der weithin zugänglichen mikroCT-Technologie zwei wesentliche Ergebnisse: Sie ermöglichte neue Einblicke in die Lakunanmorphologie prämenopausaler Frauen mit seltenen Formen der Osteoporose und versetzte Forscher mit Zugang zu mikroCT-Systemen in die Lage, zusätzliche Hypothesen zur Lakunanmorphologie zu untersuchen.

Chapter 1

Introduction

1.1 Thesis motivation

The United Nations estimates that by 2050, 1.5 billion people will be above 65 years of age – double today's 65 and above population. Women currently represent 55% of the global population over 65 years of age, and this overrepresentation increases with age, rising to 62% of the population above 80 years of age [1]. Medical resources will need to be allocated for this population shift, with a strong focus on women. One common disease in aging women is osteoporosis, which reduces the structural integrity of the skeleton and dramatically increases the risk of fracture. An estimated 1 in 3 women over 50 years of age will experience an osteoporotic fracture, as compared to 1 in 5 men [2].

Osteoporosis is a complex disease and does not solely affect the elderly. Osteoporosis is a metabolic disease that disrupts the bone renewing (known as remodeling) process and leads to a reduction in bone mass and an overall thinning of integral microstructures within the bone architecture, thus resulting in fragile fracture-prone bone [3]. While the disease is typically detected in postmenopausal women, rare forms of osteoporosis have also been observed in younger premenopausal women. One rare form of the disease is idiopathic osteoporosis (IOP), which manifests in premenopausal women and is characterized by a history of adult low trauma fracture(s) with low bone mineral density (BMD) with unknown etiology [4]. Derived from the Mayo Clinic's incidence data and the United States census for women aged 20 to 49 (assuming even age distribution), the IOP incidence rate is 2828/year with a prevalence of 68,184 cases in the United States [4, 5]. This remains below the threshold that defines an orphan (rare) disease: less than 200,000 cases. Like patients with other forms of osteoporosis, IOP patients are prone to spontaneous fractures. Few studies have explored this rare disease [6-8], and the main findings are comparable with postmenopausal osteoporotic studies: fewer, thinner, and more separated trabecular struts as well as thinner cortices in affected subjects as compared with controls [9-13]. Hence, our understanding of the disease and the potential biomarkers that could be used to indicate IOP is limited. It is important to identify and investigate the discontinuities in our knowledge about IOP before steps can be taken towards creating effective therapies. The goal of this thesis is to investigate the tissue and cellular microstructure of bone biopsies from IOP patients and determine specific biomarkers that could be used to differentiate between healthy and disease cases as well as provide clues towards indication of disease severity in IOP patients.

Bone is an extremely complex biological material and to maintain its structural integrity, the organ continuously remodels itself throughout an organism's lifespan. This process requires a conducive mechanical environment for the organ [14]. The bone then adapts its structure to the demands of its mechanical environment, which in turn enables the organ to withstand normal daily loads [15, 16]. Specifically, the components within the bone microstructure which are highly loaded adapt to their environment by locally forming additional bone, while components that are lowly loaded adapt through bone removal [17, 18]. This process is guided by three main cells: the osteoblast, the osteoclast, and the osteocyte. Osteoblasts form bone, osteoclasts resorb bone, and the osteocytes orchestrate the process of formation and resorption by sending molecular cues to osteoblasts and osteoclasts, respectively [19, 20]. Previous studies have shown that the osteocyte is sensitive to the mechanical milieu in which it inhabits and sends remodeling signals accordingly [20, 21]. Yet, the remodeling process is delicate and when compromised, bone is at increased risk for diseases such as osteoporosis to manifest, which ultimately leads to increased bone fragility and fractures.

Due to its geometry, an ideal structure to designate as a biomarker within the bone microarchitecture is the lacuna. Lacunae are ellipsoidal-shaped, individual cave-like structures embedded within the bone matrix where the osteocytes live. These lacunae are roughly 10 to 20 micrometers in diameter and are intricately connected within the interior of the bone matrix [22, 23]. Collectively, the lacunae and mechano-sensing osteocytes within constitute the lacunar-canalicular network (LCN) through which signals are passed between cells via dendrites, located within canaliculi, to coordinate bone remodeling with the nearby osteoblasts and osteoclasts on the surface [24]. Just as osteocytes base their signals on the mechanical environment, the lacunae which separate the osteocyte from the bone matrix must also play a role. Previous studies have shown that the ellipsoidal geometry of the lacuna is important, and stress concentrations form because of this geometry [25, 26]. Therefore, if the geometry of the lacuna is altered, the influence of the mechanical environment on the lacuna will also be distorted. Consequently, the osteocyte within the altered lacuna will experience an incorrect measure of its local mechanical environment, and this will affect the cascade of molecular signals that follow mechano-sensation and ultimately will change patterns of bone formation and resorption at the tissue level.

To adequately assess this, and as is described in further detail in aims 1 and 2, the lacunar biomarkers will be both morphological and mechanical in nature. Using micro-computed

tomography (microCT), clinical transiliac bone biopsies from both healthy and diseased human patients were imaged first with a nominal voxel resolution of 10 micrometers for the whole biopsy and then with a resolution of 1.2 micrometers for sub-volumes. This allowed the quantification of standard and specific lacunar morphological parameters such as the number, density, and shape of the lacunae. Following ultra-high-resolution imaging of the bone, a volume of interest was isolated from the center of the imaged biopsy and each voxel was transformed to an eight-node brick element for micro-finite element analysis (microFE) with a uniaxial compression load case applied in the medial-lateral direction. MicroFE simulation and analysis processes have been developed over a variety of similar research projects in our laboratory and provided a solid foundation for the investigation of the mechanical environment within the tissue microarchitecture [27-30]. Not only did our simulations reveal the mechanical environment of the bone microarchitecture, but also the mechanics surrounding each individual lacunar cavity, another potential biomarker. To understand the mechanical significance of the lacunar architecture and the heterogeneous mineral densities within the bone tissue, we developed a set of microcrack models to delve deeper into the hypotheses and assertions of previous studies [31-33]. Together, the morphological and mechanical analyses of lacunae and their environment provided a unique set of characteristics to compare IOP with control cohorts, which we explored in aim 3, while also creating a large dataset from which lacunar biomarkers could be derived.

1.2 Specific aims

To understand the role of osteocyte lacunae in human rare bone diseases, the structures must be measured, described, and quantified. The overarching objective of this thesis was to develop computational approaches that both morphologically and mechanically characterize these lacunae. The resulting set of unique parameters will allow for a detailed comparison between affected and control cohorts. Three specific aims were created to achieve this:

Aim 1: Develop a method to perform large-scale quantification of osteocyte lacunar morphological biomarkers.

Aim 2: Develop a method for the *in silico* quantification of osteocyte lacunar mechanical biomarkers.

Aim 3: Create osteocyte lacunar biomarkers for the characterization of human rare bone diseases.

1.3 Thesis outline

Five chapters comprise the thesis. The motivation and aims are described in the current chapter and a short summary of the following four chapters are as follows:

Chapter 2 provides background relevant to lacunar imaging and microcrack simulations in bone and the clinical relevance that can be ascertained. The first section describes previous imaging modalities to image lacunar structures and ranges from strategies using synchrotron radiation computed tomography (SR-CT) to confocal laser scanning microscopy (CLSM) and ultimately highlighting the advantages of desktop micro-computed tomography (microCT). The second section reviews previous experimental and computational modeling approaches used for exploring microcracking in bone and its interaction with lacunar structures. The final section ties in the importance of these lacunar structures to open clinical questions regarding IOP, idiopathic low bone mineral density (ILBMD), and adiposity.

Chapter 3 describes the methods developed and explored for imaging, extracting, and measuring lacunar morphometries as well as their surrounding mechanics. The first part details the exploration of an optimization method developed for accurately extracting lacunar structures and differentiating them from noise structures. The second part presents a fully validated approach to imaging lacunar structures in human bone biopsies. This included measures of accuracy, reproducibility, and sensitivity with respect to the acquisition of lacunar structures. Lacunar morphometric parameters were measured and compared between cortical and trabecular regions within a group of 31 transiliac biopsies extracted from healthy premenopausal women. These morphometric parameters were expressed as global, local, and population-based measures. The third part presents two computational models, which simulate microcracking in bone and are compared with previous experimental findings to move towards a mechanical characterization of lacunae.

Chapter 4 describes the application of imaging methodology developed in the previous chapter to analyze clinically relevant biopsies on a large scale. The first part of the chapter demonstrates the imaging methodology applied to a set of 103 transiliac biopsies to extract 26.2 million lacunae to contrast lacunar morphologies from IOP, ILBMD, and control cohorts in both

trabecular and cortical regions. Furthermore, relationships between lacunar morphometric parameters and tissue morphometric parameters were investigated. The second part applies the same lacunar morphometric analysis to the control cohort, but now divided into tertiles based on levels of adiposity to relate lacunar morphologies to overall trunk fat measured in each subject.

Chapter 5 provides a synthesis of this thesis and highlights the important findings, the limitations of this body of work, and directions for future research.

References

[1] U. Nations, World Population Ageing 2020 (ST/ESA/SER. A/444), Department of Economic and Social Affairs, Population Division. New York, USA (2021).

[2] T. Sözen, L. Özışık, N.Ç. Başaran, An overview and management of osteoporosis, European journal of rheumatology 4(1) (2017) 46.

[3] J.A. Kanis, L.J. Melton, C. Christiansen, C.C. Johnston, N. Khaltaev, Perspective - The Diagnosis of Osteoporosis, Journal of Bone and Mineral Research 9(8) (1994) 1137-1141.

[4] S. Khosla, E.G. Lufkin, S.F. Hodgson, L.A. Fitzpatrick, L.J. Melton, Epidemiology and clinical features of osteoporosis in young individuals, Bone 15(5) (1994) 551-555.

[5] U.S.B.o.t. Census, Census 2010, U.S. Government Printing Office, Washington, DC, 2010.

[6] A. Cohen, D.W. Dempster, R.R. Recker, E.M. Stein, J.M. Lappe, H. Zhou, A.J. Wirth, G.H. van Lenthe, T. Kohler, A. Zwahlen, R. Muller, C.J. Rosen, S. Cremers, T.L. Nickolas, D.J. McMahon, H. Rogers, R.B. Staron, J. LeMaster, E. Shane, Abnormal bone microarchitecture and evidence of osteoblast dysfunction in premenopausal women with idiopathic osteoporosis, J Clin Endocrinol Metab 96(10) (2011) 3095-105.

[7] A. Cohen, X.S. Liu, E.M. Stein, D.J. McMahon, H.F. Rogers, J. LeMaster, R.R. Recker, J.M. Lappe, X.E. Guo, E. Shane, Bone Microarchitecture and Stiffness in Premenopausal Women with Idiopathic Osteoporosis, J. Clin. Endocrinol. Metab. 94(11) (2009) 4351-4360.

[8] A. Cohen, R.R. Recker, J. Lappe, D.W. Dempster, S. Cremers, D.J. McMahon, E.M. Stein, J. Fleischer, C.J. Rosen, H. Rogers, R.B. Staron, J. Lemaster, E. Shane, Premenopausal women with idiopathic low-trauma fractures and/or low bone mineral density, Osteoporos Int 23(1) (2012) 171-82.

[9] A.M. Parfitt, C.H.E. Mathews, A.R. Villanueva, M. Kleerekoper, B. Frame, D.S. Rao, Relationships Between Surface, Volume, And Thickness Of Iliac Trabecular Bone In Aging And In Osteoporosis - Implications For The Microanatomic And Cellular Mechanisms Of Bone Loss, J. Clin. Invest. 72(4) (1983) 1396-1409.

[10] E. Legrand, D. Chappard, C. Pascaretti, M. Duquenne, S. Krebs, V. Rohmer, M.F. Basle, M. Audran, Trabecular bone microarchitecture, bone mineral density, and vertebral fractures in male osteoporosis, Journal of Bone and Mineral Research 15(1) (2000) 13-19.

[11] S. Majumdar, H. Genant, S. Grampp, D. Newitt, V.H. Truong, J. Lin, A. Mathur, Correlation of trabecular bone structure with age, bone mineral density, and osteoporotic status: in vivo studies in the distal radius using high resolution magnetic resonance imaging, Journal of Bone and Mineral Research 12(1) (1997) 111-118.

[12] H. Ritzel, M. Amling, M. Pösl, M. Hahn, G. Delling, The thickness of human vertebral cortical bone and its changes in aging and osteoporosis: A histomorphometric analysis of the complete spinal column from thirty-seven autopsy specimens, Journal of Bone and Mineral Research 12(1) (1997) 89-95.

[13] D. Hans, A.L. Goertzen, M.A. Krieg, W.D. Leslie, Bone microarchitecture assessed by TBS predicts osteoporotic fractures independent of bone density: the Manitoba study, Journal of Bone and Mineral Research 26(11) (2011) 2762-2769.

[14] J.Y. Rho, L. Kuhn-Spearing, P. Zioupos, Mechanical properties and the hierarchical structure of bone, Med. Eng. Phys. 20(2) (1998) 92-102.

[15] J. Wolff, Das Gesetz der Transformation der Knochen, DMW-Deutsche Medizinische Wochenschrift 19(47) (1892) 1222-1224.

[16] W. Roux, Der Kampf der Theile im Organismus: ein Beitrag zur Vervollständigung der mechanischen Zweckmässigkeitslehre, W. Engelmann1881.

[17] H.M. Frost, Bone "mass" and the "mechanostat": a proposal, Anat Rec 219(1) (1987) 1-9.

[18] R. Huiskes, R. Ruimerman, G.H. van Lenthe, J.D. Janssen, Effects of mechanical forces on maintenance and adaptation of form in trabecular bone, Nature 405(6787) (2000) 704-6.

[19] S.L. Dallas, M. Prideaux, L.F. Bonewald, The osteocyte: an endocrine cell ... and more, Endocr Rev 34(5) (2013) 658-90.

[20] L.F. Bonewald, The amazing osteocyte, J Bone Miner Res 26(2) (2011) 229-38.

[21] L. Lanyon, Osteocytes, strain detection, bone modeling and remodeling, Calcified tissue international 53(1) (1993) S102-S107.

[22] F.L. Bach-Gansmo, A. Bruel, M.V. Jensen, E.N. Ebbesen, H. Birkedal, J.S. Thomsen, Osteocyte lacunar properties and cortical microstructure in human iliac crest as a function of age and sex, Bone 91 (2016) 11-19.

[23] P. Dong, S. Haupert, B. Hesse, M. Langer, P.J. Gouttenoire, V. Bousson, F. Peyrin, 3D osteocyte lacunar morphometric properties and distributions in human femoral cortical bone using synchrotron radiation micro-CT images, Bone 60 (2014) 172-185.

[24] H. Kamioka, T. Honjo, T. Takano-Yamamoto, A three-dimensional distribution of osteocyte processes revealed by the combination of confocal laser scanning microscopy and differential interference contrast microscopy, Bone 28(2) (2001) 145-9.

[25] A.R. Stern, D.P. Nicolella, Measurement and estimation of osteocyte mechanical strain, Bone 54(2) (2013) 191-5.

[26] S.W. Verbruggen, T.J. Vaughan, L.M. McNamara, Strain amplification in bone mechanobiology: a computational investigation of the in vivo mechanics of osteocytes, Journal of the Royal Society Interface 9(75) (2012) 2735-2744.

[27] D. Webster, F.A. Schulte, F.M. Lambers, G. Kuhn, R. Muller, Strain energy density gradients in bone marrow predict osteoblast and osteoclast activity: a finite element study, J Biomech 48(5) (2015) 866-74.

[28] D.J. Webster, P.L. Morley, G.H. van Lenthe, R. Muller, A novel in vivo mouse model for mechanically stimulated bone adaptation--a combined experimental and computational validation study, Comput Methods Biomech Biomed Engin 11(5) (2008) 435-41.

[29] F.A. Schulte, D. Ruffoni, F.M. Lambers, D. Christen, D.J. Webster, G. Kuhn, R. Muller, Local mechanical stimuli regulate bone formation and resorption in mice at the tissue level, PLoS One 8(4) (2013) e62172.

[30] F.A. Schulte, A. Zwahlen, F.M. Lambers, G. Kuhn, D. Ruffoni, D. Betts, D.J. Webster, R. Muller, Strain-adaptive in silico modeling of bone adaptation--a computer simulation validated by in vivo micro-computed tomography data, Bone 52(1) (2013) 485-92.

[31] R. Voide, P. Schneider, M. Stauber, G.H. van Lenthe, M. Stampanoni, R. Muller, The importance of murine cortical bone microstructure for microcrack initiation and propagation, Bone 49(6) (2011) 1186-93.

[32] R. Voide, P. Schneider, M. Stauber, R. Wyss, M. Stampanoni, U. Sennhauser, G.H. van Lenthe, R. Muller, Time-lapsed assessment of microcrack initiation and propagation in murine cortical bone at submicrometer resolution, Bone 45(2) (2009) 164-173.

[33] F. Donaldson, D. Ruffoni, P. Schneider, A. Levchuk, A. Zwahlen, P. Pankaj, R. Muller, Modeling microdamage behavior of cortical bone, Biomech Model Mechanobiol 13(6) (2014) 1227-42.

Chapter 2

Background

2.1 Large-scale lacunar imaging and quantification

The lacunar-canalicular network (LCN) is an extremely dense three-dimensional network of pores, osteocytes occupying those pores, dendritic canals, and the thin biological processes enclosed in the dendritic canals that weave the skeletal system together. With respect to the connectivity of the network, the densely wired LCN resembles that of the brain [1]. Lacunar pores in humans typically range from 50μm^3 to 1500μm^3, although it is not a normally distributed range [2]. Yet, previous imaging studies demonstrate that the dendritic processes which compose the canalicular network are on the nanometer scale [3]. Therefore, the investigation of this porous network requires imaging technology that is powerful enough to zoom in on these tiny structures while still being able to capture a quantity that is large enough to perform meaningful analyses.

2.1.1 Imaging acquisition techniques for measuring lacunae

Beginning with the highest resolution imaging technologies, transmission electron microscopy (TEM) and scanning electron microscopy (SEM) have been previously implemented for imaging lacunae [3-7]. These technologies use a high-energy beam to rebound electrons from the surface of a material towards a detector that can reconstruct an image far past the limits of optical diffraction with a typical resolution in the range of 10nm [8]. Focused ion beam scanning electron microscopy (FIB-SEM) is an SEM variant that uses an ion beam to carefully cleave the surface of the material so that sequential SEM images can be reconstructed as a stack of 2D images that approximate a 3D image with the same nanometer resolution range [9-11]. However, this is a destructive imaging technique and is typically excluded with respect to samples that were difficult to acquire. Furthermore, while this technique can clearly image lacunar structures and their extending dendritic processes, the field of view is extremely narrow, and it is only possible to visualize several lacunae simultaneously. Therefore, this technology is reserved for small-scale analyses including only a few dozen lacunae [12, 13].

Confocal laser scanning microscopy (CLSM) is another high-resolution imaging technology that is capable of visualizing lacunar structures in detail. CLSM functions similarly to conventional microscopy with the difference that CLSM uses a laser beam in combination with filters and mirrors instead of a conventional lamp and set of glass lenses for optical

amplification of the sample [14, 15]. This allows for the limits of optical diffraction to be circumvented as well and for resolutions on the range of 100nm to be achieved. Lacunar structures can be clearly visualized while the canalicular processes are only dimly present [16-19]. CLSM, just like SEM technologies, again is limited regarding the number of lacunae which can be visualized and is on the scale of a few hundred per sample which includes a field of view depth of around 100µm [20].

For researchers that have access to synchrotron radiation computed tomography (SR-CT), objects can be imaged in high-resolution and on a large scale. This is because SR-CT uses an extremely stable monochromatic energized beam (x-ray) with a high photon count to project through an object on to a detector. This stability allows for image acquisition times in a sub 1-hour time window and achieve nanometer nominal voxel resolutions. The instruments required for SR-CT are both large and expensive, and consequently SR-CT technologies are typically housed at beamline facilities (for example the Swiss Light Source here in Switzerland). Most SR-CT facilities are in high demand which makes time on the SR-CT very competitive. Researchers typically must write a project proposal many months in advance for a short 24- to 72-hour window of facility use. Consequently, relatively few lacunar studies have been conducted with SR-CT [21-25].

Desktop micro-computed tomography (microCT) strikes an excellent balance between resolution and scale. This technology has been a cornerstone of bone research for more than 20 years and is a widely used imaging methodology for both researchers and clinicians alike [26-29]. The principle is the same as SR-CT (an x-ray beam is projected through a rotating object onto a detector), yet the instrument itself requires a fraction of the space and the finances to operate. Historically, microCT has been used for bone tissue morphometry because its resolution was on the range of 10-40 micrometers. Yet, recent advances in the technology have allowed microCT to achieve resolutions of up to 1 micrometer, allowing for clear visualization of the lacunar morphometry [30]. Combined with a sample carousel, researchers can automatically acquire images with millions of lacunae over multiple samples in a span of days. These advantages make desktop microCT an ideal technology for future lacunar studies.

2.1.2 Lacunar morphometry

Equally as important as the three-dimensional lacunar images acquired from the above-mentioned technologies are the scientific terms dedicated to describing the morphometry of a lacuna. It is important that the nomenclature is simple, logical, and uniform between studies. Uniformity of any field's terminology is difficult to achieve, but regarding bone tissue parameters, Dempster et al. published a comprehensive review article that attempts to standardize the symbols and meanings [31]. These efforts have unfortunately not been fully extended to the lacunar level and consequently many morphometric parameters exist under different names and symbols between research groups [30, 32, 33]. The work in this thesis looks to the Dempster et al. publication for guidance and adheres to their strict two-letter principle for morphometric descriptors [31]. The table below outlines each morphometric parameter and the associated definition and abbreviation which is continued throughout the thesis and conforms to the rules originally created by Dempster et al. [31].

Table 2.1.1: Nomenclature regarding lacunar morphometry. Abbreviations adhere to the strict guidelines that were most recently updated by Dempster et al. and thus provide a good foundation for terminology standardization [31].

Morphometric parameter	Abbreviation & Units	Definition
Lacunar Porosity	Lc.TV/BV (%)	Total lacunar volume divided by total bone volume.
Lacunar Number	Lc.N (1)	Total number of lacunae present in region
Lacunar Density	Lc.N/BV (1/mm^3)	Total number of lacunae divided by the bone volume of the region
Lacunar Volume	Lc.V (μm^3)	Volume measurement of individual lacunae
Lacunar Surface Area	Lc.S (μm^2)	Surface area measurement of individual lacunae
Lacunar Surface Area to Volume Ratio	Lc.S/Lc.V (1/μm)	Ratio between lacunar surface area and volume
Lacunar Stretch	Lc.St (1)	Elongation of the lacuna. Range from 0 to 1. Where 0 is a perfect sphere and 1 is an infinitely stretched rod.
Lacunar Oblateness	Lc.Ob (1)	Flatness or pancake resemblance of lacunae. Range from -1 to 1. Where -1 is a flat-pressed circular structure, and 1 an infinitely stretched rod.
Lacunar Sphericity	Lc.Sr (1)	Resemblance of lacuna to a sphere based on its ratio of surface area to volume when compared with that of an ideal sphere. Range from 0 to 1 where 0 is dissimilar to a sphere and 1 is identical to a sphere.
Lacunar Equancy	Lc.Eq (1)	Ratio between major and minor lacunar axes. Another way to express sphericity.
Lacunar Angle	Lc.θ (Degree)	Angle between lacunar major axis and arbitrarily defined vector extending through the image volume.

These definitions provide a good common ground for researchers to engage in meaningful exchanges regarding lacunar morphometry. At the minimum, it provides a methodical approach

to creating a standardized nomenclature that can be built upon in future studies of the lacuna and the mineralized matrix it inhabits.

2.1.3 Image processing

Appropriate post-processing of desktop microCT images is also necessary. Because the x-ray beam used in desktop microCT devices is polychromatic, the image must be filtered to reduce artifacts. The landmark Bouxsien et al. study recommends all microCT images to be filtered with a Gaussian filter, and many tissue studies choose the parameters of that filter to be a sigma of 1.2 [26]. The sigma relates to how narrow or wide the Gaussian distribution of the filter is and a wider distribution (larger sigma) results in a smoother image. While the filter with a sigma of 1.2 is ideal for many tissue analyses as it sufficiently smooths the bone surface, it blurs many micropores and consequently, also lacunar structures, beyond recognition. Therefore, a Gaussian filter with a smaller sigma value, in the range of 0.8, would benefit the researcher with respect to lacunar studies. This allows for the reduction of noise artifacts, which are inherent with polychromatic x-ray beams, while not blurring the lacunar pores beyond the point of recognition.

Segmentation of lacunae must also be carefully considered. This is a three-step process in which the bone is first segmented from the image background using a threshold, then inverted, and ultimately component labeled to catalog all pores resembling lacunar structures. For this, the selection of the image threshold is the critical step. Typical microCT studies investigating the bone microstructure refer again to the Bouxsein et al. study to choose an adequate threshold [26]. This threshold is a subjective measure which is identified visually for one sample, fixed, and then applied to all samples in a study. At very high resolution however, the distribution of tissue mineral density (TMD) values (directly converted from the linear attenuation values of the beam) varies greatly between samples, rendering a fixed threshold approach ineffective. While a standardized approach such as the Bouxsein et al. study [26] describes does not exist with respect to lacunar segmentation from high-resolution microCT images, previous studies have identified sample-specific thresholds based on relative values that are intrinsic to the sample. Such individually set thresholds typically include a clear landmark on the sample-specific TMD histogram which is, for example, a defined offset from the peak [34].

Even with the best approach to calculating a segmentation threshold, many segmented objects will not be lacunae. Other objects include small non-lacunar pores (less than 20μm^3), large, connected structures like Haversian canals and Volkmann's canals (greater than 2000μm^3), or thin elongated structures including noise artefacts (20-2000µm). Consequently, filters based on morphological features must be designed and applied. Upper limits of metrics such as Lc.St and Lc.Ob can be set to remove the thin elongated structures while Lc.V can be set to remove objects above and below certain values. Yet, this volumetric threshold differs widely between previous studies and has been as constrained as 50-610μm^3 or as inclusive as 175-2000μm^3 [23, 32, 35-38]. Of course, this is because the volumetric range of lacunae is extremely dependent on the species and anatomical site [39]. Absolute numbers are difficult to find in the literature because the nanometer resolution that is required for these studies (SEM, TEM, FIB-SEM) severely limits the lacunar population size and consequently limits generalizable Lc.V ranges to be considered as a "gold standard". As stated before, SR-CT strikes a good balance between scale and resolution; however, this tool has only been used to image a narrow range of species and anatomical sites.

2.1.4 Validation

Validation is extremely important for any methodology and highlights its relevance, credibility, and most importantly – the rigor that was involved with its development. Typically, validation is broken down into three categories: accuracy, reproducibility, and sensitivity.

Accuracy is defined as the proximity of the measured quantity to a previously defined ground truth. While a perfect (true) measurement can never be achieved, only approached asymptotically, a ground truth is held to be sufficient for the method and is usually measured with an instrument an order of magnitude more accurate than the experimental methodology (for example a Vernier caliper versus a yardstick). Regarding lacunar morphometry, an ideal accuracy measure would be the comparison between the experimental imaging technology, desktop microCT, and a higher resolution technology such as FIB/SEM. The measured difference between the two technologies is regarded as the error of the experimental method and is a standard accuracy metric [40]. Unfortunately, 3D registration of lacunar structures between imaging technologies and spatial scales is extremely difficult for several reasons and has not been pursued. The closest comparison between imaging technologies with respect to

lacunar data sets would be the Bland-Altman plots that Hemmatian et al. present for microporosity measured with CLSM and microCT [30]. However, accuracy in the lacunar context can be also considered as the error between an automatic segmentation algorithm (the experimental method) and a manual segmentation by a trained human observer (the ground truth) [34]. While not a description of morphological accuracy, this binary classification allows for accuracy calculations such as true positive rate (TPR), false positive rate (FPR), and false negative rate (FNR).

Reproducibility, otherwise known as precision, is the method's repeatability. In other words, how close do multiple measurements of the same quantity correspond to each other. Reproducibility is typically measured in terms of precision error (PE) and intraclass correlation coefficients (ICC). PE provides an indication of average deviation between measurements while ICC describes how closely measurements in the same category resemble each other [41, 42]. The spread of each, known as the coefficient of variation, can also be reported by means of calculating the Chi-square distribution. With respect to lacunar morphometry, it is important that basic morphometry such as lacunar porosity and lacunar volume are repeatable [30]. This typically requires a reproducibility experiment with no less than 20 DOF and repositioning of the sample between each measurement [43].

The third validation criterion is sensitivity. This is broadly defined as the method's ability to detect known and previously defined differences. Treating the method as a black box, modulating the known input should also alter the resulting output in a meaningful way. With respect to lacunae, previous studies have identified morphometric differences between lacunae originating from young and old bone [44-46] and also between cortical and trabecular bone [32, 47]. Therefore, it is important that the imaging methodology produces different morphometric outputs based on inputs that are known to be different such as the lacunae from cortical and trabecular regions.

2.2 Lacunar mechanics and microcracking

2.2.1 Lacunar shape to osteocyte mechanosensation

Three-dimensional geometry is inextricably linked to the mechanical load placed upon it, and osteocyte lacunae are no exception. As Figure 2.2.1 describes, idealized spherical geometries produce different strain patterns when compared with prolate and oblate ellipsoidal geometries [48]. Lacunae typically fall somewhere in this range between ellipsoidal and spherical geometries and the resulting deformation, and hence mechanical signal, within the lacunar space (and on the osteocyte) can differ drastically. A primary component of this osteocyte relevant mechanical signal is believed to be fluid-flow shear stress, and therefore, alterations in lacunar deformation will impact this signal [49-52]. On the extreme side, lacunar shape has been linked to interstitial fluid loss and osteocyte necrosis via microdamage initiation [53]. Bone remodeling then typically follows this microdamage [54]. Computational finite element models have been implemented to investigate the importance of lacunar orientation relative to loading and have been observed that lacunae parallel to the direction of loading were less affected by the subsequently induced microdamage than those that were oriented perpendicularly to the applied load [55].

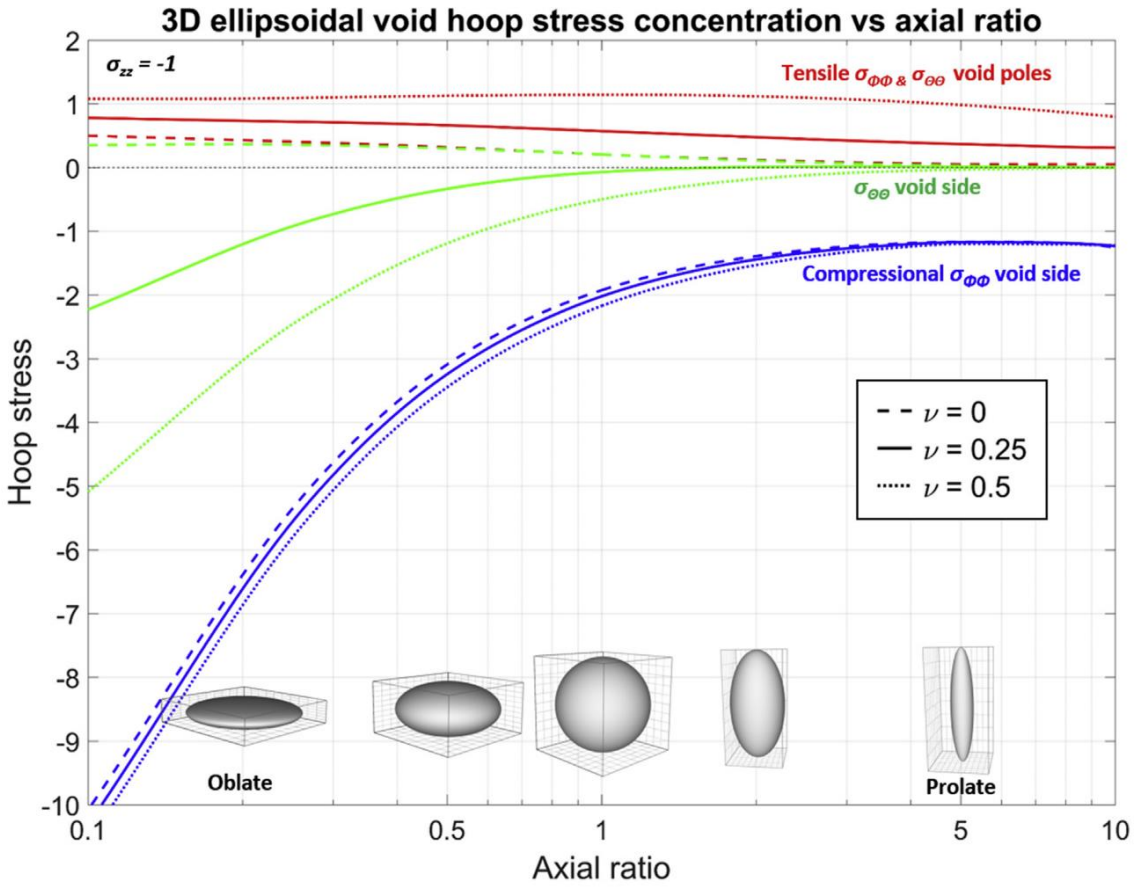

Figure 2.2.1: Illustrates a variety of ellipsoidal geometries and the differing hoop stress concentrations for each geometry based on vertical compressive stress. Reproduced from Davis et al. 2017 [48].

Previous in-vitro studies have investigated the possibility that differently shaped osteocytes under the same loading conditions will have differing degrees of mechanosensitivity. While the data in this thesis do not include osteocytes, mechanosensitivity was inferred via lacunar shape, and hypotheses were derived from previous in-vitro osteocyte studies. Bacabac et al. [56] created populations of round and flat osteocytes and compared their stiffness with optical tweezers. Round osteocytes were determined to be less stiff than flat osteocytes and hence, round osteocytes were concluded to have the more mechanosensitive geometry. Later studies approaching osteocyte mechanosensitivity from a fluid-flow perspective concluded with similar findings [57]. Furthermore, the stresses at lacunar apexes are strongly concentrated and are even stronger at the connection points to the surrounding canaliculi [58-62]. It appears that the loading patterns at the LCN scale are extremely heterogeneous and within these patterns lie important clues to how the system senses and responds to mechanical loading.

2.2.2 Microcracking

Microcracks within the bone tissue matrix are a normal progression within the bone remodeling process. From a purely mechanical perspective, the LCN has been observed to diffuse the mechanical energy generated from microcracks in normally loaded bone [24, 63-67]. The majority of these microcracks are small (10um – 1mm) and act as cues for subsequent local remodeling [68-70]. However, in cases of overloaded bone tissue, microcracks propagate rapidly through the matrix, ultimately resulting in stress fractures [71-75]. Since the embedded osteocytes are orders of magnitude softer than the surrounding mineralized matrix, the lacunae which house them consequently act as nodes attracting crack propagation just as ions in water create a path of least resistance for an electrical charge to pass through.

Experimental work has documented this phenomenon, most notably the studies conducted by Voide et al. regarding time-lapsed microcracking in murine bone which was illustrated with microCT images [76, 77]. Voide and his colleagues noted the following observations about microcracking: they were primarily linear, initiated at large canals, parallel to the axis of loading, and were guided by lacunar pores. While the experimental evidence on the topic beyond their studies is limited, these findings provide an excellent foundation for a computational model to be constructed. This is important because further experimental studies are difficult to justify since they require bone harvested from animals to extract additional data for testing more complex hypotheses when the same could be simulated using computers.

Computational models allow for experiments to be simulated (non-destructively) and for multiple hypotheses to be tested in a relatively short span of time. With respect to mechanical simulations, micro-finite element (microFE) models are extremely useful. MicroFE is a common computational modeling tool used for a variety of engineering applications which typically require factor-of-safety design calculation such as bridge structure design. As the structural support for the human body, bone is an ideal biological application for microFE simulations, and many studies have used it to explore its mechanical properties [78-80]. In general, these microFE simulations are based on the reconstructed 3D image voxels that are acquired from a 3D imaging technology. Each voxel possesses a gray-scale intensity value, directly linked to the raw signal (linear attenuation coefficient for microCT), which is then translated to a bone-specific material stiffness and converted to an element. Boundary

conditions are then applied to the model and the simulation is run to test the hypothesis conceived by the researcher.

Using these basic principles of microFE, multiple compressive iterations can be applied to an image volume to simulate failure and observe crack propagation. Several years after the experimental work of Voide et al. was performed [76, 77], Donaldson et al. created a microFE model based on Voide's findings [81]. Donaldson created several models to simulate crack growth in mouse bone and ultimately simulated microcracking that resembled what Voide observed experimentally. While this is the currently the established state-of-the-art model relative to the topic, the simulation is oversimplified because it uses a binarized image, which includes only elements with a uniform bone stiffness derived from previous experimental work [82] (~10.6GPa) and non-bone elements which are considered to have a stiffness of near zero. This ignores the crucial fact that bone is a heterogeneous material which encompasses a broad range of stiffnesses that will impact the loading of the bone and ultimately the development of the crack within the tissue. Consequently, there is ample room for this computational model to be improved upon and there are many more additional hypotheses to be tested.

2.3 Clinical importance

2.3.1 Rare bone disease

Many research groups have investigated osteoporosis in postmenopausal women [83-86]. However, there remains a relative paucity of knowledge surrounding osteoporosis in premenopausal women. Osteoporosis in premenopausal women is uncommon, and in most cases, is related to diseases or medication exposures associated with bone loss and bone fragility. Rarely, premenopausal women present with fractures or very low BMD in the absence of any such systemic disease or medication exposure. These conditions termed idiopathic osteoporosis (IOP) and idiopathic low bone mineral density (ILBMD) are of particular interest. IOP, defined by a history of low trauma fracture(s), is a rare bone condition that impacts the lives of young, otherwise healthy individuals and is by definition regarded as osteoporosis from an unknown origin [87]. It has an estimated prevalence of 68,184 cases (fewer than 200,000 is considered rare). [88]. Similarly, ILBMD subjects are described as having low bone mass (DXA

T score ≤2.5 or Z score ≤ 2.0 at the spine or hip) but without an adult fracture and are young and otherwise healthy individuals [89].

Cohen et al. have previously investigated and compared cohorts of IOP (n=45), ILBMD (n=19), and control (n=40) subjects and observed significant differences between their tissue microarchitectures [89]. Affected subjects overall (IOP and ILBMD) had fewer, thinner, and more separated trabecular structures when compared with the control group. Furthermore, the cortices in the affected population were also thinner than in the cohort of control subjects. An analogous study in men with IOP discovered that the disease was also associated with impaired osteoblast function [90, 91]. Reduced remodeling has also been found within IOP transiliac bone biopsies [92-96].

2.3.2 Aging and bone

Aging is also considered to be an important catalyst for changes in the morphology of osteocytes and their lacunar structures. Specifically, lacunar density has been demonstrated to decrease in human subjects relative to age by roughly 15–30% in the endosteal and periosteal regions [44, 45, 97-99]. Studies involving murine bone have corroborated these findings as well as noting a volumetric decrease in aged lacunae [100]. Furthermore, the rate of empty lacunae (lacunae without a resident osteocyte) also dramatically increases with age and consequently reduces the number of viable osteocytes in both human and murine bone [101-104].

2.3.3 Adiposity and bone

Obesity is an increasingly prevalent problem in society and places a large burden on the healthcare sector [105]. In addition to large cardiovascular risks, obesity also raises the risk of fracture for people of all ethnicities, sexes, and ages [106-110]. Several research groups have highlighted the importance of central adiposity in the fat/bone relationship by demonstrated the strong inverse relationship between bone mineral density (BMD) and abdominal fat when controlling for the body mass index (BMI) [111-117]. This abdominal fat can be divided into two types of fat: visceral adipose tissue (VAT) and subcutaneous adipose tissue (SAT). VAT is located in the abdominal region surrounding the internal organs, while SAT is the adipose tissue that lies directly beneath the skin. Clinically speaking, VAT is considered to be an

extremely important fat compartment and is related to an increased risk of diabetes, cardiovascular disease, and other debilitating illnesses [118, 119]. Furthermore, VAT has also been linked to bone with recent data connecting it with increased osteocytic expression of sclerostin, a protein that inhibits bone formation [120]. The type of tissue can be distinguished using abdominal computed tomography (CT), and previous studies have shown VAT to be connected with a decrease in BMD and overall bone quality [112, 114, 121, 122]. VAT can be approximated by measuring trunk fat with dual-energy x-ray absorptiometry (DXA) since the two are strongly correlated [123]. This is useful since DXA is a simpler technology with less radiation and is also more widely available than CT.

The relationship between bone quality and adiposity was explored in a study published by Cohen et al. with a cohort of 40 healthy women [123]. They surgically extracted a transiliac biopsy from each subject and subsequently imaged each using microCT to evaluate the 3D micro-architecture. These morphometric parameters were compared with central adiposity assessed using trunk fat from full body DXA scans and discovered that subjects with high VAT possessed fewer and thinner trabecular structures as well as an overall lower trabecular bone volume (BV/TV). Mechanics of the trabecular regions were also estimated using micro-finite element (microFE) analysis to calculate stiffness. Trabecular stiffness was also lower in subjects with high VAT. Within cortical regions, porosity (Ct.Po) was higher in subjects with high VAT. Finally, histology revealed that subjects with high VAT also showed a reduction in the rate of bone formation. The mechanism for this relationship between central adiposity and bone formation is not known, however, one important mediator may be the level of physical activity. Preliminary data suggests that women with high VAT also reported less physical activity and had higher serum sclerostin levels [120]. These findings highlight the relationship between body composition and bone health and provide a foundation to build a greater understanding of the relationship between bone and adipose tissue.

References

[1] P.R. Buenzli, N.A. Sims, Quantifying the osteocyte network in the human skeleton, Bone 75(79) (2015) 144-50.

[2] B.R. McCreadie, S.J. Hollister, M.B. Schaffler, S.A. Goldstein, Osteocyte lacuna size and shape in women with and without osteoporotic fracture, Journal of Biomechanics 37(4) (2004) 563-572.

[3] L.D. You, S. Weinbaum, S.C. Cowin, M.B. Schaffler, Ultrastructure of the osteocyte process and its pericellular matrix, Anat. Rec. Part A 278A(2) (2004) 505-513.

[4] W.R. Thompson, S. Modla, B.J. Grindel, K.J. Czymmek, C.B. Kirn-Safran, L.Y. Wang, R.L. Duncan, M.C. Farach-Carson, Perlecan/Hspg2 Deficiency Alters the Pericellular Space of the Lacunocanalicular System Surrounding Osteocytic Processes in Cortical Bone, Journal of Bone and Mineral Research 26(3) (2011) 618-629.

[5] S. Okada, S. Yoshida, S.H. Ashrafi, D.E. Schraufnagel, The canalicular structure of compact bone in the rat at different ages, Microsc. microanal. 8(2) (2002) 104-115.

[6] G. Marotti, M.A. Muglia, D. Zaffe, A SEM Study Of Osteocyte Orientation In Alternately Structured Osteons, Bone 6(5) (1985) 331-334.

[7] G. Marotti, V. Cane, S. Palazzini, C. Palumbo, Structure-function relationships in the osteocyte, Ital J Miner Electrolyte Metab 4(2) (1990) 93-106.

[8] A. Bogner, P.H. Jouneau, G. Thollet, D. Basset, C. Gauthier, A history of scanning electron microscopy developments: Towards "wet-STEM" imaging, Micron 38(4) (2007) 390-401.

[9] L. Holzer, M. Cantoni, Review of FIB-tomography, Nanofabrication using focused ion and electron beams: Principles and applications 559201222 (2012) 410-435.

[10] A. Kubis, G. Shiflet, R. Hull, D. Dunn, Focused ion-beam tomography, Metallurgical and Materials Transactions A 35(7) (2004) 1935-1943.

[11] W.J. MoberlyChan, D.P. Adams, M.J. Aziz, G. Hobler, T. Schenkel, Fundamentals of focused ion beam nanostructural processing: Below, at, and above the surface, MRS Bull. 32(5) (2007) 424-432.

[12] P. Schneider, M. Meier, R. Wepf, R. Muller, Serial FIB/SEM imaging for quantitative 3D assessment of the osteocyte lacuno-canalicular network, Bone 49(2) (2011) 304-11.

[13] D.J. Stokes, J. Tong, J. Juhasz, P. Midgley, S.M. Best, Characterisation and 3D visualisation of biomaterials and tissues using focused ion beam (E) SEM, Microsc. microanal. 11(S02) (2005) 1260-1261.

[14] J.-A. Conchello, J.W. Lichtman, Optical sectioning microscopy, Nat Methods 2(12) (2005) 920-931.

[15] Y. Garini, B.J. Vermolen, I.T. Young, From micro to nano: recent advances in high-resolution microscopy, Current opinion in biotechnology 16(1) (2005) 3-12.

[16] A. Vatsa, R.G. Breuls, C.M. Semeins, P.L. Salmon, T.H. Smit, J. Klein-Nulend, Osteocyte morphology in fibula and calvaria - Is there a role for mechanosensing?, Bone 43(3) (2008) 452-458.

[17] Y. Sugawara, R. Ando, H. Kamioka, Y. Ishihara, S.A. Murshid, K. Hashimoto, N. Kataoka, K. Tsujioka, F. Kajiya, T. Yamashiro, The alteration of a mechanical property of bone cells during the process of changing from osteoblasts to osteocytes, Bone 43(1) (2008) 19-24.

[18] Y. Sugawara, H. Kamioka, T. Honjo, K. Tezuka, T. Takano-Yamamoto, Three-dimensional reconstruction of chick calvarial osteocytes and their cell processes using confocal microscopy, Bone 36(5) (2005) 877-883.

[19] E.J. Anderson, S.M. Kreuzer, O. Small, M.L.K. Tate, Pairing computational and scaled physical models to determine permeability as a measure of cellular communication in micro- and nano-scale pericellular spaces, Microfluidics and nanofluidics 4(3) (2008) 193-204.

[20] C.W. Jones, D. Smolinski, A. Keogh, T. Kirk, M. Zheng, Confocal laser scanning microscopy in orthopaedic research, Progress in Histochemistry and Cytochemistry 40(1) (2005) 1-71.

[21] A. Carriero, M. Doube, M. Vogt, B. Busse, J. Zustin, A. Levchuk, P. Schneider, R. Muller, S.J. Shefelbine, Altered lacunar and vascular porosity in osteogenesis imperfecta mouse bone as revealed by synchrotron tomography contributes to bone fragility, Bone 61 (2014) 116-124.

[22] K.S. Mader, L.R. Donahue, R. Muller, M. Stampanoni, High-throughput phenotyping and genetic linkage of cortical bone microstructure in the mouse, Bmc Genomics 16 (2015) 11.

[23] K.S. Mader, P. Schneider, R. Muller, M. Stampanoni, A quantitative framework for the 3D characterization of the osteocyte lacunar system, Bone 57(1) (2013) 142-54.

[24] P. Schneider, M. Stauber, R. Voide, M. Stampanoni, L.R. Donahue, R. Muller, Ultrastructural properties in cortical bone vary greatly in two inbred strains of mice as assessed by synchrotron light based micro- and Nano-CT, Journal of Bone and Mineral Research 22(10) (2007) 1557-1570.

[25] P. Dong, S. Haupert, B. Hesse, M. Langer, P.J. Gouttenoire, V. Bousson, F. Peyrin, 3D osteocyte lacunar morphometric properties and distributions in human femoral cortical bone using synchrotron radiation micro-CT images, Bone 60 (2014) 172-185.

[26] M.L. Bouxsein, S.K. Boyd, B.A. Christiansen, R.E. Guldberg, K.J. Jepsen, R. Muller, Guidelines for Assessment of Bone Microstructure in Rodents Using Micro-Computed Tomography, Journal of Bone and Mineral Research 25(7) (2010) 1468-1486.

[27] T. Hildebrand, A. Laib, R. Muller, J. Dequeker, P. Ruegsegger, Direct three-dimensional morphometric analysis of human cancellous bone: Microstructural data from spine, femur, iliac crest, and calcaneus, Journal of Bone and Mineral Research 14(7) (1999) 1167-1174.

[28] P. Ruegsegger, B. Koller, R. Muller, A microtomographic system for the nondestructive evaluation of bone architecture, Calcified Tissue International 58(1) (1996) 24-29.

[29] A. Cohen, X.S. Liu, E.M. Stein, D.J. McMahon, H.F. Rogers, J. LeMaster, R.R. Recker, J.M. Lappe, X.E. Guo, E. Shane, Bone Microarchitecture and Stiffness in Premenopausal Women with Idiopathic Osteoporosis, J. Clin. Endocrinol. Metab. 94(11) (2009) 4351-4360.

[30] H. Hemmatian, M.R. Laurent, S. Ghazanfari, D. Vanderschueren, A.D. Bakker, J. Klein-Nulend, G.H. van Lenthe, Accuracy and reproducibility of mouse cortical bone microporosity as quantified by desktop microcomputed tomography, Plos One 12(8) (2017).

[31] D.W. Dempster, J.E. Compston, M.K. Drezner, F.H. Glorieux, J.A. Kanis, H. Malluche, P.J. Meunier, S.M. Ott, R.R. Recker, A.M. Parfitt, Standardized Nomenclature, Symbols, and Units for Bone Histomorphometry: A 2012 Update of the Report of the ASBMR Histomorphometry Nomenclature Committee, Journal of Bone and Mineral Research 28(1) (2013) 1-16.

[32] M.P. Akhter, D. Kimmel, J. Lappe, R. Recker, Effect of Macroanatomic Bone Type and Estrogen Loss on Osteocyte Lacunar Properties in Healthy Adult Women, Calcified Tissue International (2017) 1-12.

[33] B.L. Yu, A. Pacureanu, C. Olivier, P. Cloetens, F. Peyrin, Assessment of the human bone lacuno-canalicular network at the nanoscale and impact of spatial resolution, Sci Rep 10(1) (2020) 12.

[34] E.N. Cresswell, T.M. Nguyen, M.W. Horsfield, A.J. Alepuz, T.A. Metzger, G.L. Niebur, C.J. Hernandez, Mechanically induced bone formation is not sensitive to local osteocyte density in rat vertebral cancellous bone, J Orthop Res (2017).

[35] Y. Carter, C.D.L. Thomas, J.G. Clement, A.G. Peele, K. Hannah, D.M.L. Cooper, Variation in osteocyte lacunar morphology and density in the human femur - a synchrotron radiation micro-CT study, Bone 52(1) (2013) 126-132.

[36] F.L. Bach-Gansmo, A. Bruel, M.V. Jensen, E.N. Ebbesen, H. Birkedal, J.S. Thomsen, Osteocyte lacunar properties and cortical microstructure in human iliac crest as a function of age and sex, Bone 91 (2016) 11-19.

[37] A. Levchuk, P. Schneider, M. Meier, P. Vogel, F. Donaldson, R. Muller, An Automated Step-Wise Micro-Compression Device for 3D Dynamic Image-Guided Failure Assessment of Bone Tissue on a Microstructural Level Using Time-Lapsed Tomography, Frontiers in Materials 5 (2018) 14.

[38] S.M. Tommasini, A. Trinward, A.S. Acerbo, F. De Carlo, L.M. Miller, S. Judex, Changes in intracortical microporosities induced by pharmaceutical treatment of osteoporosis as detected by high resolution micro-CT, Bone 50(3) (2012) 596-604.

[39] P. Milovanovic, B. Busse, Inter-site Variability of the Human Osteocyte Lacunar Network: Implications for Bone Quality, Curr Osteoporos Rep (2019).

[40] J.A. Swets, Measuring The Accuracy Of Diagnostic Systems, Science 240(4857) (1988) 1285-1293.

[41] J.P. Weir, Quantifying test-retest reliability using the intraclass correlation coefficient and the SEM, J. Strength Cond. Res. 19(1) (2005) 231-240.

[42] P.E. Shrout, J.L. Fleiss, Intraclass Correlations - Uses In Assessing Rater Reliability, Psychol. Bull. 86(2) (1979) 420-428.

[43] C.-C. Glüer, G. Blake, Y. Lu, B. Blunt, M. Jergas, H. Genant, Accurate assessment of precision errors: how to measure the reproducibility of bone densitometry techniques, Osteoporosis International 5(4) (1995) 262-270.

[44] M. Mullender, D. Van der Meer, R. Huiskes, P. Lips, Osteocyte density changes in aging and osteoporosis, Bone 18(2) (1996) 109-113.

[45] D. Vashishth, O. Verborgt, G. Divine, M.B. Schaffler, D.P. Fyhrie, Decline in osteocyte lacunar density in human cortical bone is associated with accumulation of microcracks with age, Bone 26(4) (2000) 375-380.

[46] C.R. Dunstan, N.M. Somers, R.A. Evans, Rubin, Ott, Snyder, Davy, Schaffler, Parfitt, Goldstein, Osteocyte death and hip fracture, Calcified Tissue International 53 (1993) S113-S117.

[47] C.A. Baud, E. Auil, Osteocyte Differential Count In Normal Human Alveolar Bone, Acta Anat. 78(3) (1971) 321-+.

[48] T. Davis, D. Healy, A. Bubeck, R. Walker, Stress concentrations around voids in three dimensions: The roots of failure, J. Struct. Geol. 102 (2017) 193-207.

[49] S.C. Cowin, L. Moss-Salentijn, M.L. Moss, Candidates for the mechanosensory system in bone, Journal of biomechanical engineering 113(2) (1991) 191-197.

[50] E.H. Burger, J. Klein-Nulend, Mechanotransduction in bone - role of the lacuno-canalicular network, Faseb J. 13 (1999) S101-S112.

[51] S. Weinbaum, S.C. Cowin, Y. Zeng, A model for the excitation of osteocytes by mechanical loading-induced bone fluid shear stresses, J Biomech 27(3) (1994) 339-60.

[52] J. Klein-Nulend, A.D. Bakker, R.G. Bacabac, A. Vatsa, S. Weinbaum, Mechanosensation and transduction in osteocytes, Bone 54(2) (2013) 182-190.

[53] O. Verborgt, G.J. Gibson, M.B. Schaffler, Loss of osteocyte integrity in association with microdamage and bone remodeling after fatigue in vivo, Journal of Bone and Mineral Research 15(1) (2000) 60-67.

[54] D.B. Burr, R.B. Martin, M.B. Schaffler, E.L. Radin, Bone remodeling in response to invivo fatigue microdamage, Journal of Biomechanics 18(3) (1985) 189-&.

[55] P.J. Prendergast, R. Huiskes, Microdamage and osteocyte-lacuna strain in bone: A microstructural finite element analysis, J Biomech Eng-T Asme 118(2) (1996) 240-246.

[56] R.G. Bacabac, D. Mizuno, C.F. Schmidt, F.C. MacKintosh, J.J. Van Loon, J. Klein-Nulend, T.H. Smit, Round versus flat: bone cell morphology, elasticity, and mechanosensing, J Biomech 41(7) (2008) 1590-8.

[57] J. Qiu, A.D. Baik, X.L. Lu, E.M.C. Hillman, Z. Zhuang, C. Dong, X.E. Guo, A noninvasive approach to determine viscoelastic properties of an individual adherent cell under fluid flow, Journal of Biomechanics 47(6) (2014) 1537-1541.

[58] S.W. Verbruggen, T.J. Vaughan, L.M. McNamara, Strain amplification in bone mechanobiology: a computational investigation of the in vivo mechanics of osteocytes, Journal of the Royal Society Interface 9(75) (2012) 2735-2744.

[59] D.P. Nicolella, D.E. Moravits, A.M. Gale, L.F. Bonewald, J. Lankford, Osteocyte lacunae tissue strain in cortical bone, J Biomech 39(9) (2006) 1735-43.

[60] A.R. Stern, D.P. Nicolella, Measurement and estimation of osteocyte mechanical strain, Bone 54(2) (2013) 191-5.

[61] D. Christen, A. Levchuk, S. Schori, P. Schneider, S.K. Boyd, R. Muller, Deformable image registration and 3D strain mapping for the quantitative assessment of cortical bone microdamage, J Mech Behav Biomed Mater 8 (2012) 184-93.

[62] A.R. Bonivtch, L.F. Bonewald, D.P. Nicolella, Tissue strain amplification at the osteocyte lacuna: a microstructural finite element analysis, Journal of biomechanics 40(10) (2007) 2199-2206.

[63] R.W. McCalden, J.A. McGeough, M.B. Barker, Age-related changes in the tensile properties of cortical bone. The relative importance of changes in porosity, mineralization, and microstructure, The Journal of bone and joint surgery. American volume 75(8) (1993) 1193-1205.

[64] Y.N. Yeni, C.U. Brown, Z. Wang, T.L. Norman, The influence of bone morphology on fracture toughness of the human femur and tibia, Bone 21(5) (1997) 453-459.

[65] K.L. Bell, N. Loveridge, J. Power, N. Garrahan, B.F. Meggitt, J. Reeve, Regional differences in cortical porosity in the fractured femoral neck, Bone 24(1) (1999) 57-64.

[66] G. Jordan, N. Loveridge, K. Bell, J. Power, N. Rushton, J. Reeve, Spatial clustering of remodeling osteons in the femoral neck cortex: a cause of weakness in hip fracture?, Bone 26(3) (2000) 305-313.

[67] P. Schneider, R. Voide, M. Stampanoni, L.R. Donahue, R. Muller, The importance of the intracortical canal network for murine bone mechanics, Bone 53(1) (2013) 120-8.

[68] N.L. Fazzalari, M.R. Forwood, K. Smith, B.A. Manthey, P. Herreen, Assessment of cancellous bone quality in severe osteoarthrosis: Bone mineral density, mechanics, and microdamage, Bone 22(4) (1998) 381-388.

[69] T.C. Lee, S. Mohsin, D. Taylor, R. Parkesh, T. Gunnlaugsson, F.J. O'Brien, M. Giehl, W. Gowin, Detecting microdamage in bone, Journal of Anatomy 203(2) (2003) 161-172.

[70] F.J. O'Brien, D. Taylor, G.R. Dickson, T.C. Lee, Visualisation of three-dimensional microcracks in compact bone, Journal of Anatomy 197 (2000) 413-420.

[71] B.R. Beck, Tibial stress injuries - An aetiological review for the purposes of guiding management, Sports Med. 26(4) (1998) 265-279.

[72] D.B. Burr, Bone, Exercise, and Stress Fractures, Exercise and Sport Sciences Reviews 25(1) (1997) 171-194.

[73] S.W. Donahue, N.A. Sharkey, K.A. Modanlou, L.N. Sequeira, R.B. Martin, Bone strain and microcracks at stress fracture sites in human metatarsals, Bone 27(6) (2000) 827-833.

[74] J.G. Peloso, J.P. Watkins, S.R. Keele, E.L. Morris, Bilateral stress-fractures of the tibia in a racing american quarter horse, J. Am. Vet. Med. Assoc. 203(6) (1993) 801-803.

[75] D. Taylor, J.G. Hazenberg, T.C. Lee, Living with cracks: Damage and repair in human bone, Nat. Mater. 6(4) (2007) 263-268.

[76] R. Voide, P. Schneider, M. Stauber, G.H. van Lenthe, M. Stampanoni, R. Muller, The importance of murine cortical bone microstructure for microcrack initiation and propagation, Bone 49(6) (2011) 1186-93.

[77] R. Voide, P. Schneider, M. Stauber, R. Wyss, M. Stampanoni, U. Sennhauser, G.H. van Lenthe, R. Muller, Time-lapsed assessment of microcrack initiation and propagation in murine cortical bone at submicrometer resolution, Bone 45(2) (2009) 164-173.

[78] D. Ruffoni, G. Van Lenthe, 3.10 Finite element analysis in bone research: a computational method relating structure to mechanical function, Compr. Biomater. II 3 (2017) 169-196.

[79] P. Christen, K. Ito, R. Ellouz, S. Boutroy, E. Sornay-Rendu, R.D. Chapurlat, B. van Rietbergen, Bone remodelling in humans is load-driven but not lazy, Nat Commun 5 (2014) 4855.

[80] P. Christen, K. Ito, A.A. Santos, R. Muller, R. Bert van, Validation of a bone loading estimation algorithm for patient-specific bone remodelling simulations, J Biomech 46(5) (2013) 941-8.

[81] F. Donaldson, D. Ruffoni, P. Schneider, A. Levchuk, A. Zwahlen, P. Pankaj, R. Muller, Modeling microdamage behavior of cortical bone, Biomech Model Mechanobiol 13(6) (2014) 1227-42.

[82] U. Wolfram, H.J. Wilke, P.K. Zysset, Rehydration of vertebral trabecular bone: Influences on its anisotropy, its stiffness and the indentation work with a view to age, gender and vertebral level, Bone 46(2) (2010) 348-354.

[83] D.M. Black, C.J. Rosen, Postmenopausal osteoporosis, New England Journal of Medicine 374(3) (2016) 254-262.

[84] P.D. Delmas, Treatment of postmenopausal osteoporosis, The Lancet 359(9322) (2002) 2018-2026.

[85] P.J. Meunier, P.D. Delmas, R. Eastell, M.R. McClung, S. Papapoulos, R. Rizzoli, E. Seeman, R.D. Wasnich, Diagnosis and management of osteoporosis in postmenopausal women: clinical guidelines, Clinical therapeutics 21(6) (1999) 1025-1044.

[86] S.R. Cummings, J.S. Martin, M.R. McClung, E.S. Siris, R. Eastell, I.R. Reid, P. Delmas, H.B. Zoog, M. Austin, A. Wang, Denosumab for prevention of fractures in postmenopausal women with osteoporosis, New England Journal of Medicine 361(8) (2009) 756-765.

[87] H.M. Heshmati, S. Khosla, Idiopathic osteoporosis: a heterogeneous entity, Ann. Med. Interne 149(2) (1998) 77-81.

[88] S. Khosla, E.G. Lufkin, S.F. Hodgson, L.A. Fitzpatrick, L.J. Melton, Epidemiology and clinical features of osteoporosis in young individuals, Bone 15(5) (1994) 551-555.

[89] A. Cohen, D.W. Dempster, R.R. Recker, E.M. Stein, J.M. Lappe, H. Zhou, A.J. Wirth, G.H. van Lenthe, T. Kohler, A. Zwahlen, R. Muller, C.J. Rosen, S. Cremers, T.L. Nickolas, D.J. McMahon, H. Rogers, R.B. Staron, J. LeMaster, E. Shane, Abnormal bone microarchitecture and evidence of osteoblast dysfunction in premenopausal women with idiopathic osteoporosis, J Clin Endocrinol Metab 96(10) (2011) 3095-105.

[90] P.J. Marie, M.C. Devernejoul, D. Connes, M. Hott, Decreased Dna-Synthesis By Cultured Osteoblastic Cells In Eugonadal Osteoporotic Men With Defective Bone-Formation, J. Clin. Invest. 88(4) (1991) 1167-1172.

[91] S. Khosla, Idiopathic osteoporosis - Is the osteoblast to blame?, J. Clin. Endocrinol. Metab. 82(9) (1997) 2792-2794.

[92] A.G. Johansson, E.F. Eriksen, E. Lindh, B. Landahl, W.F. Blum, A. Lindahl, O. Ljunggren, S. Ljunghall, Reduced serum levels of the growth hormone-dependent insulin-like growth factor binding protein and a negative bone balance at the level of individual remodeling units in idiopathic osteoporosis in men, J. Clin. Endocrinol. Metab. 82(9) (1997) 2795-2798.

[93] E.S. Kurland, C.J. Rosen, F. Cosman, D. McMahon, F. Chan, E. Shane, R. Lindsay, D. Dempster, J.P. Bilezikian, Insulin-like growth factor-I in men with idiopathic osteoporosis, J. Clin. Endocrinol. Metab. 82(9) (1997) 2799-2805.

[94] Y. Pernow, E.M. Hauge, K. Linder, E. Dahl, M. Saaf, Bone Histomorphometry in Male Idiopathic Osteoporosis, Calcified Tissue International 84(6) (2009) 430-438.

[95] B.Y. Reed, J.E. Zerwekh, K. Sakhaee, N.A. Breslau, F. Gottschalk, C.Y.C. Pak, Serum Igf-1 Is Low And Correlated With Osteoblastic Surface In Idiopathic Osteoporosis, Journal of Bone and Mineral Research 10(8) (1995) 1218-1224.

[96] J.E. Zerwekh, K. Sakhaee, N.A. Breslau, F. Gottschalk, C.Y.C. Pak, Impaired Bone-Formation In Male Idiopathic Osteoporosis - Further Reduction In The Presence Of Concomitant Hypercalciuria, Osteoporosis International 2(3) (1992) 128-134.

[97] B. Busse, D. Djonic, P. Milovanovic, M. Hahn, K. Püschel, R.O. Ritchie, M. Djuric, M. Amling, Decrease in the osteocyte lacunar density accompanied by hypermineralized lacunar

occlusion reveals failure and delay of remodeling in aged human bone, Aging cell 9(6) (2010) 1065-1075.

[98] S. Qiu, D. Rao, S. Palnitkar, A. Parfitt, Age and distance from the surface but not menopause reduce osteocyte density in human cancellous bone, Bone 31(2) (2002) 313-318.

[99] S. Mori, R. Harruff, W. Ambrosius, D. Burr, Trabecular bone volume and microdamage accumulation in the femoral heads of women with and without femoral neck fractures, Bone 21(6) (1997) 521-526.

[100] C.M. Heveran, A. Rauff, K.B. King, R.D. Carpenter, V.L. Ferguson, A new open-source tool for measuring 3D osteocyte lacunar geometries from confocal laser scanning microscopy reveals age-related changes to lacunar size and shape in cortical mouse bone, Bone 110 (2018) 115-127.

[101] S. Qiu, D. Rao, S. Palnitkar, A. Parfitt, Relationships between osteocyte density and bone formation rate in human cancellous bone, Bone 31(6) (2002) 709-711.

[102] L.M. Tiede-Lewis, Y.X. Xie, M.A. Hulbert, R. Campos, M.R. Dallas, V. Dusevich, L.F. Bonewald, S.L. Dallas, Degeneration of the osteocyte network in the C57BL/6 mouse model of aging, Aging-US 9(10) (2017) 2187-+.

[103] M. Piemontese, M. Almeida, A.G. Robling, H.-N. Kim, J. Xiong, J.D. Thostenson, R.S. Weinstein, S.C. Manolagas, C.A. O'Brien, R.L. Jilka, Old age causes de novo intracortical bone remodeling and porosity in mice, JCI insight 2(17) (2017).

[104] L.B. Meakin, G.L. Galea, T. Sugiyama, L.E. Lanyon, J.S. Price, Age-related impairment of bones' adaptive response to loading in mice is associated with sex-related deficiencies in osteoblasts but no change in osteocytes, Journal of Bone and Mineral Research 29(8) (2014) 1859-1871.

[105] K.M. Flegal, M.D. Carroll, B.K. Kit, C.L. Ogden, Prevalence of obesity and trends in the distribution of body mass index among US adults, 1999-2010, Jama 307(5) (2012) 491-497.

[106] J.E. Compston, J. Flahive, D.W. Hosmer, N.B. Watts, E.S. Siris, S. Silverman, K.G. Saag, C. Roux, M. Rossini, J. Pfeilschifter, Relationship of weight, height, and body mass index with fracture risk at different sites in postmenopausal women: the Global Longitudinal study of

Osteoporosis in Women (GLOW), Journal of Bone and Mineral Research 29(2) (2014) 487-493.

[107] J.E. Compston, N.B. Watts, R. Chapurlat, C. Cooper, S. Boonen, S. Greenspan, J. Pfeilschifter, S. Silverman, A. Díez-Pérez, R. Lindsay, Obesity is not protective against fracture in postmenopausal women: GLOW, The American journal of medicine 124(11) (2011) 1043-1050.

[108] C.M. Nielson, L.M. Marshall, A.L. Adams, E.S. LeBlanc, P.M. Cawthon, K. Ensrud, M.L. Stefanick, E. Barrett-Connor, E.S. Orwoll, O.F.i.M.S.R. Group, BMI and fracture risk in older men: the osteoporotic fractures in men study (MrOS), Journal of Bone and Mineral Research 26(3) (2011) 496-502.

[109] L. Laslett, S.J. nee Foley, S. Quinn, T. Winzenberg, G. Jones, Excess body fat is associated with higher risk of vertebral deformities in older women but not in men: a cross-sectional study, Osteoporosis International 23(1) (2012) 67-74.

[110] A. Goulding, A.M. Grant, S.M. Williams, Bone and body composition of children and adolescents with repeated forearm fractures, Journal of Bone and Mineral Research 20(12) (2005) 2090-2096.

[111] L.-J. Zhao, Y.-J. Liu, P.-Y. Liu, J. Hamilton, R.R. Recker, H.-W. Deng, Relationship of obesity with osteoporosis, The Journal of Clinical Endocrinology & Metabolism 92(5) (2007) 1640-1646.

[112] M.A. Bredella, M. Torriani, R.H. Ghomi, B.J. Thomas, D.J. Brick, A.V. Gerweck, L.M. Harrington, A. Breggia, C.J. Rosen, K.K. Miller, Determinants of bone mineral density in obese premenopausal women, Bone 48(4) (2011) 748-754.

[113] M.A. Bredella, M. Torriani, R.H. Ghomi, B.J. Thomas, D.J. Brick, A.V. Gerweck, C.J. Rosen, A. Klibanski, K.K. Miller, Vertebral bone marrow fat is positively associated with visceral fat and inversely associated with IGF-1 in obese women, Obesity 19(1) (2011) 49-53.

[114] V. Gilsanz, J. Chalfant, A.O. Mo, D.C. Lee, F.J. Dorey, S.D. Mittelman, Reciprocal relations of subcutaneous and visceral fat to bone structure and strength, The Journal of Clinical Endocrinology & Metabolism 94(9) (2009) 3387-3393.

[115] N.K. Pollock, E. Laing, M.W. Hamrick, C. Baile, D. Hall, R. Lewis, Bone and fat relationships in postadolescent black females: a pQCT study, Osteoporosis international 22(2) (2011) 655-665.

[116] A. Janicka, T.A. Wren, M.M. Sanchez, F. Dorey, P.S. Kim, S.D. Mittelman, V. Gilsanz, Fat mass is not beneficial to bone in adolescents and young adults, The Journal of Clinical Endocrinology & Metabolism 92(1) (2007) 143-147.

[117] Y. Sheu, J.A. Cauley, The role of bone marrow and visceral fat on bone metabolism, Curr. Osteoporos. Rep. 9(2) (2011) 67-75.

[118] G.A. Bray, K.A. Jablonski, W.Y. Fujimoto, E. Barrett-Connor, S. Haffner, R.L. Hanson, J.O. Hill, V. Hubbard, A. Kriska, E. Stamm, Relation of central adiposity and body mass index to the development of diabetes in the Diabetes Prevention Program, The American journal of clinical nutrition 87(5) (2008) 1212-1218.

[119] G. Iacobellis, M.C. Ribaudo, F. Assael, E. Vecci, C. Tiberti, A. Zappaterreno, U. Di Mario, F. Leonetti, Echocardiographic epicardial adipose tissue is related to anthropometric and clinical parameters of metabolic syndrome: a new indicator of cardiovascular risk, The Journal of Clinical Endocrinology & Metabolism 88(11) (2003) 5163-5168.

[120] A. Cohen, A. Costa, R. Recker, J. Lappe, S. Cremers, D. Dempster, H. Zhou, A. Zwahlen, R. Mueller, E. Stein, Lower Bone Volume Fraction and Bone Formation Rate in Premenopausal Women with Abdominal Obesity Are Associated with Less Physical Activity and Higher Serum Sclerostin, Journal Of Bone And Mineral Research, Wiley-Blackwell 111 River St, Hoboken 07030-5774, NJ USA, 2013.

[121] M. Russell, N. Mendes, K.K. Miller, C.J. Rosen, H. Lee, A. Klibanski, M. Misra, Visceral fat is a negative predictor of bone density measures in obese adolescent girls, The Journal of Clinical Endocrinology & Metabolism 95(3) (2010) 1247-1255.

[122] H.S. Choi, K.J. Kim, K.M. Kim, N.W. Hur, Y. Rhee, D.S. Han, E.J. Lee, S.-K. Lim, Relationship between visceral adiposity and bone mineral density in Korean adults, Calcified tissue international 87(3) (2010) 218-225.

[123] A. Cohen, D.W. Dempster, R.R. Recker, J.M. Lappe, H. Zhou, A. Zwahlen, R. Muller, B. Zhao, X. Guo, T. Lang, I. Saeed, X.S. Liu, X.E. Guo, S. Cremers, C.J. Rosen, E.M. Stein,

T.L. Nickolas, D.J. McMahon, P. Young, E. Shane, Abdominal fat is associated with lower bone formation and inferior bone quality in healthy premenopausal women: a transiliac bone biopsy study, J Clin Endocrinol Metab 98(6) (2013) 2562-72.

Chapter 3

Imaging and quantification of osteocyte lacunar biomarkers

3.1 A novel shape filter for lacunar imaging in human bone using ultra-high-resolution desktop micro-CT

Elliott Goff [1], Basil Aeppli [1], and Ralph Müller [1]

[1] Institute for Biomechanics, ETH Zurich, Zurich, Switzerland

Conference proceeding published in:

6th International Conference on Computational and Mathematical Biomedical Engineering (CMBE 2019), Sendai City, Japan

Part of ISBN: 978-0-9562914-5-5

Postprint version according to publisher copyright policy

Abstract

Imaging the osteocyte-lacunar network is imperative for understanding its role in mechanosensation. Separating lacunar objects from noise structures is not a trivial task when using ultra-high-resolution desktop micro-computed tomography (micro-CT). Current studies use a simple object volume filter that excludes a substantial number of small lacunae from the analysis. This lacuna group is crucial for elucidating the small but important changes in their morphology, which may be triggered by age or disease. We present a novel shape filter that allows including small lacunae while effectively reducing noise as demonstrated through human visual inspection as a gold standard for lacunar segmentation.

Keywords:

Osteocyte-lacunar imaging, ultra-high-resolution micro-CT, shape filter

3.1.1 Introduction

The osteocyte network is one of the most vastly distributed interconnected systems in the body and consists of ≈3.7 trillion connections with the collective mass of their cell bodies and dendritic processes equating the mass of the brain [1]. This dense network has been shown to transduce mechanical ques into chemical signals and orchestrate the bone remodeling process via the coordination of bone formation and bone resorption [2-4]. Each osteocyte inhabits an individual cave-like structure known as lacuna, which hosts the unique geometry of each osteocyte and remains intact even after cell death. This allows imaging of these porous lacunar structures using x-ray radiation at the sub-micrometer resolution. Several studies have previously explored the lacunar network geometry using synchrotron radiation computed tomography (SR-CT) [5-7]. However, SR-CT is both an expensive and a scarce resource among researchers. Therefore, it is imperative that a lacunar imaging technique be developed for a more commonly available device: ultra-high-resolution desktop micro-computed tomography (micro-CT). Desktop micro-CT equipment possesses slightly lower resolution contrast compared to SR-CT making optimization of image acquisition and sample-specific processing a large challenge for this application [8, 9]. Furthermore, it is difficult to separate true lacunar objects from noise structures, which will typically also be segmented from the mineralized bone tissue using an individualized sample-specific threshold. More specifically, the distinction between small lacunar objects and noise structures is particularly difficult and recent studies typically choose a single volumetric threshold of $100\mu m^3$ – $175\mu m^3$ as the lower limit without any justification or investigation of how this threshold affects quantification the image data [10-13]. By applying such a coarse filter to the image, many small lacunae are excluded from subsequent analyses as a previous study has determined the lower limit of an osteocyte lacuna volume to be as small as $28\mu m^3$ [14]. Therefore, we present an improved method to separate lacunar objects from noise structures using a two-parameter shape filter that is optimized by visual inspection of every object and applies an exclusion criterion based upon both volume of the object and the ratio of the object's surface-to-volume ratio.

3.1.2 Materials and Methods

Four human iliac crest biopsies embedded in PMMA were imaged at a nominal voxel resolution of 1.2µm using a µCT50 imaging system (Scanco Medical, Bassersdorf Switzerland). A sub-volume of between 200µm^3 – 300µm^3, which consisted of roughly 250 objects, was selected from each sample with a total of 994 objects included across all four samples. A threshold was applied to each volume using a previously described sample-specific tissue mineral density (TMD) approach and all resulting objects were segmented, component labeled, and measured using a custom Python (3.7.1, Python Software Foundation, Delaware, USA) script (Figures 3.1.1a – 3.1.1c). [9]. The three-dimensional (3D) centroid location, volume, flatness, and surface area of each object were recorded into an overarching database that included all of these parameters for all objects. The 3D centroid location of each object was then used to locate and visualize the object in the original gray-scale image in each of the three orthogonal 2D planes (Figures 3.1.1d and 3.1.1e) using a custom interface in Python. Each object was visually inspected by an experienced human operator, who moved back and forth through several slices in each 2D orthogonal plane to determine if the object was a lacunar object (Figure 3.1.1d) or a noise structure (Figure 3.1.1e). This group designation from each visual inspection was also included in the database. Lacunar volume (Lc.V) and surface-to-volume ratio (Lc.S/Lc.V) were identified as the two best group separation parameters. Each parameter was iteratively applied as an object threshold and the sensitivity, specificity, and accuracy were calculated at each step. Theses plots and the value that optimized for sensitivity, specificity, and accuracy in each parameter was identified in Figure 3.1.2. These two values were then used in Figure 3.1.3 to construct a line that passes through zero and the intersection point of the two optimum parameters to separate the noise group from the lacuna group. The method was then evaluated using the leave-one-out-cross-validation (LOOCV) approach by treating the first three samples as training data to calculate the optimum linear separation of the two groups and then applying it to the fourth sample (Figure 3.1.3b).

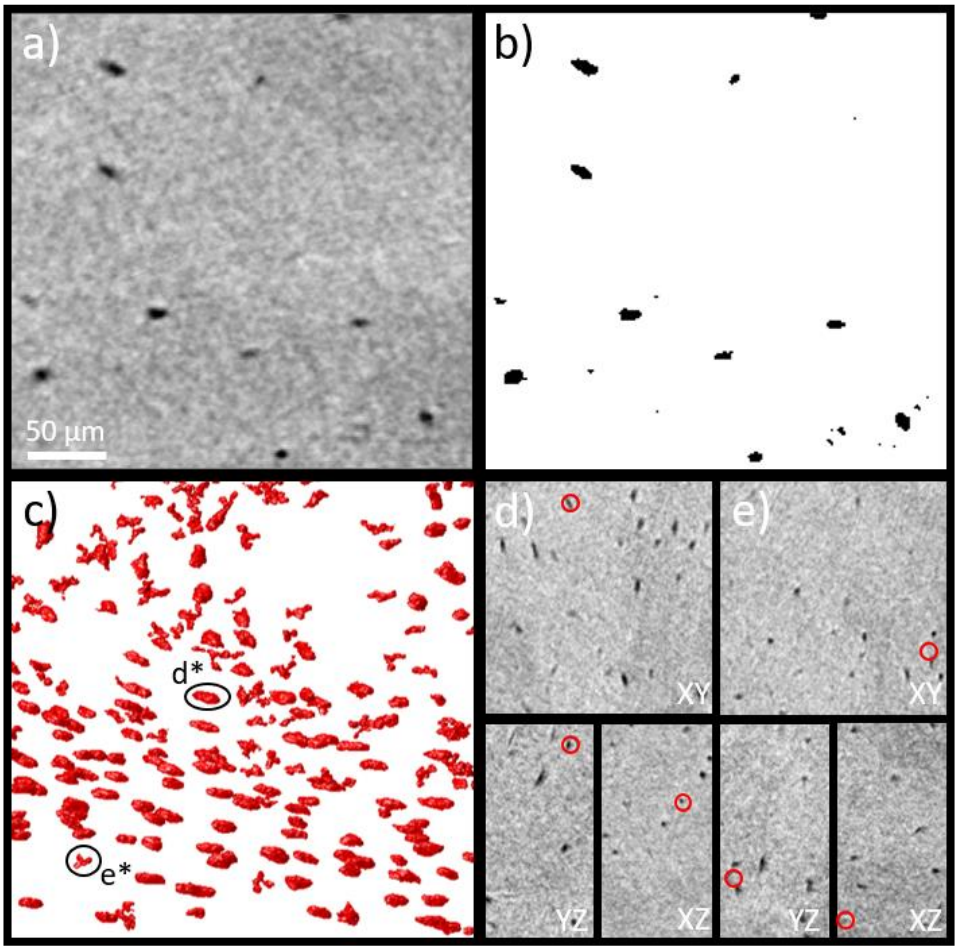

Figure 3.1.1: a) Original gray-scale micro-CT image. b) Segmented image using sample-specific TMD threshold. c) 3D visualization of segmented objects. d) 2D visualization of the 3D lacunar object d* in all three orthogonal planes of the original gray-scale image. e) 2D visualization of the 3D noise structure e* in all three orthogonal planes of the original gray-scale image.

3.1.3 Results

When optimizing for all three performance parameters, sensitivity, specificity, and accuracy, the best single parameter thresholds were calculated to be 58µm^3 for Lc.V and 1.59µm^3/µm^3 for Lc.S/Lc.V, respectively. The performance of each single threshold is tabulated in Table 3.1.1 and all three performance parameters range between 91% and 97%. Each single parameter is plotted on the corresponding axis in Figure 3.1.3 depicting how the group of accepted lacunar objects would be separated from the rejected noise structure group. The optimal 2-parameter linear separation line is shown as the dashed line in Figure 3.1.3 while the vertical dotted line in Figure 3.1.3 provides a visual comparison if the data were cut using a classical volumetric

filter of 100µm^3. The performance of the optimal linear separation of the two groups is roughly equal to that of each individual single parameter filter with sensitivity, specificity, and accuracy in the low to mid 90% range. Both single parameters and the two-parameter linear separator perform 7% to 9% better in sensitivity and accuracy, yet approximately 3% worse in specificity. Figure 3.1.3b displays the linear separator using the LOOCV method and confirms the strength of this method with sensitivity, specificity, and accuracy at 97%, 88%, and 98% respectively.

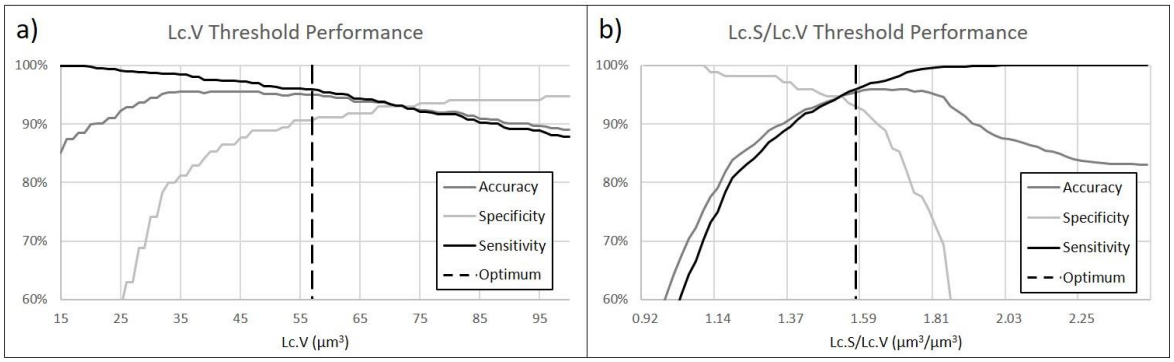

Figure 3.1.2: Accuracy, specificity, and sensitivity curves for Lc.V thresholds (a) and Lc.S/Lc.V thresholds (b) with the optimum value identified for each with the vertical dashed line.

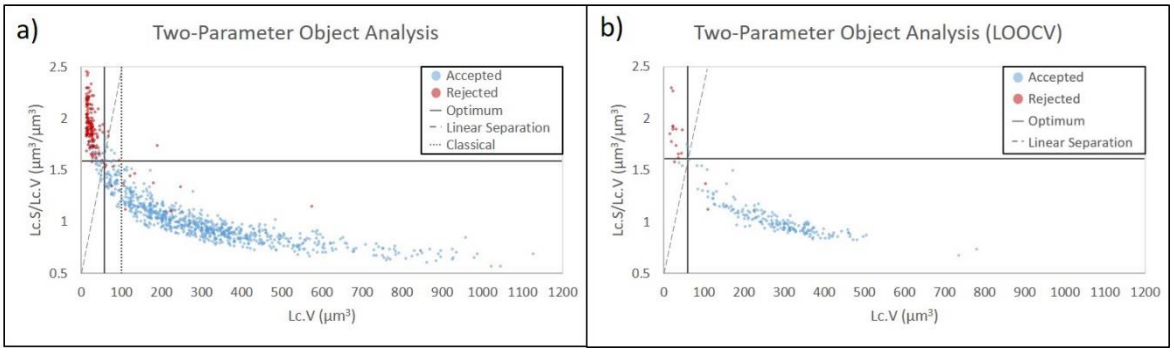

Figure 3.1.3: a) Two-parameter comparison of all objects (accepted lacunar objects and rejected noise structures). Optimum threshold of each parameter are a solid line; dashed line constructed from both optimums; classical 100µm^3 volumetric threshold as a dotted line. b) LOOCV approach by applying the optimum linear separation calculated from three samples on the fourth sample.

Table 3.1.1: Object threshold performance comparison.

Parameter	TP	TN	FP	FN	Sensitivity	Specificity	Accuracy
Optimum Lc.V (58μm^3)	789	155	15	35	95.8%	91.2%	95.0%
Optimum Lc.S/Lc.V (1.59)	795	157	13	29	96.5%	92.4%	95.8%
Linear Separation	788	155	15	36	95.6%	91.2%	94.9%
Classical Thresh (100μm^3)	724	161	9	100	87.9%	94.7%	89.0%
LOOCV Linear Separation	184	14	2	4	97.9%	87.5%	97.1%

3.1.4 Discussion

The importance of this new object separation method is twofold. When performing a lacunar analysis, it is crucial to include the small lacunae to detect where minute morphological changes occur with aging and disease. Tommasini et al. asserted that changes in these small pores could act as an indicator for changes in the canalicular morphology size and connectivity, which we believe could subsequently affect the mechanosensitivity of the osteocyte network [12]. Therefore, the sensitivity of the shape filter is critical and the new filter's 7.7% increase from the classical 100μm^3 filter is a marked improvement. We acknowledge the 3.5% reduction in specificity will allow additional non-lacunar structures to infiltrate the data but argue that this is worth the 7.7% gain in sensitivity and 4.0% gain in accuracy that the new filter provides. Furthermore, the ability to fine-tune a two-parameter linear separator is a big advantage for future datasets. Because both volume and surface-to-volume ratio thresholds are quite sensitive to changes as seen in Figure 3.1.2, it is important that a linear separator be rooted in the individual sample-specific distributions of both parameters. We are currently developing an approach for creating a custom shape filter for each sample based on these two parameters. Just as we choose a threshold that binarizes each image based on the inflection point of the specific sample's TMD histogram, we aim to link a similar measure to the object group demarcation. This will permit the construction of a sensitive, unique linear separator for each sample to split the lacunar objects from the noise structures without requiring an in-depth visual inspection of all objects in every sample.

References

[1] P.R. Buenzli and N.A. Sims. Quantifying the osteocyte network in the human skeleton. Bone, 75:144–150, 2015.

[2] J. Gluhak-Heinrich, L. Ye, L.F. Bonewald, J.Q. Feng, M. MacDougall, S.E. Harris, D. Pavlin. Mechanical loading stimulates dentin matrix protein 1 (DMP1) expression in osteocytes in vivo. J Bone Miner Res, 18:807–17, 2003.

[3] A.G. Robling, P.J. Niziolek, L.A. Baldridge, K.W. Condon, M.R. Allen, I. Alam, S.M. Mantila, J. Gluhak-Heinrich, T.M. Bellido, S.E. Harris, C.H. Turner. Mechanical stimulation of bone in vivo reduces osteocyte expression of Sost/sclerostin. J Biol Chem, 283:5866–75, 2008.

[4] T.M. Skerry, L. Bitensky, J. Chayen, L.E. Lanyon. Early strain-related changes in enzyme activity in osteocytes following bone loading in vivo. J Bone Miner Res, 4:783–8, 1989.

[5] P. Dong, S. Haupert, B. Hesse, M. Langer, P.-J. Gouttenoire, V. Bousson, F. Peyrin. 3D osteocyte lacunar morphometric properties and distributions in human femoral cortical bone using synchrotron radiation micro-CT images. Bone, 60:172–85, 2014.

[6] K.S. Mader, P. Schneider, R. Müller, M. Stampanoni. A quantitative framework for the 3D characterization of the osteocyte lacunar system. Bone, 57:142–54, 2013.

[7] K.S. Mader, L.R. Donahue, R. Müller, M. Stampanoni. High-throughput phenotyping and genetic linkage of cortical bone microstructure in the mouse. Bmc Genomics, 16:11 2015.

[8] E. Goff, D. Betts, P. Christen, R. Müller. Influence of µCT beam energy on cell lacunar imaging. 23rd Congress of the European Society of Biomechanics (ESB), 1667, 2017.

[9] E. Goff, J.P. McKinley, D.C. Betts, P. Christen, R. Müller. A novel histogram-based thresholding approach for accurate segmentation of osteocyte lacunae in micro-CT images of human bone biopsies. 8th World Congress of Biomechanics, O0418, 2018.

[10] H. Hemmatian, M.R. Laurent, S. Ghazanfari, D. Vanderschueren, A.D. Bakker, J. Klein-Nulend, G.H. van Lenthe. Accuracy and reproducibility of mouse cortical bone microporosity as quantified by desktop microcomputed tomography. Plos One 12:16 2017.

[11] C.M. Heveran, A. Rauff, K.B. King, R.D. Carpenter, V.L. Ferguson. A new open-source tool for measuring 3D osteocyte lacunar geometries from confocal laser scanning microscopy reveals age-related changes to lacunar size and shape in cortical mouse bone. Bone, 110:115–27, 2018.

[12] S.M. Tommasini, A. Trinward, A.S. Acerbo, F. De Carlo, L.M. Miller, S. Judex. Changes in intracortical microporosities induced by pharmaceutical treatment of osteoporosis as detected by high resolution micro-CT. Bone 50:596–604, 2012.

[13] A. Levchuk, P. Schneider, M. Meier, P. Vogel, F. Donaldson, R. Müller. An Automated Step-Wise Micro-Compression Device for 3D Dynamic Image-Guided Failure Assessment of Bone Tissue on a Microstructural Level Using Time-Lapsed Tomography. Frontiers in Materials, 5:14, 2018.

[14] B.R. McCreadie, S.J. Hollister, M.B. Schaffler, S.A. Goldstein. Osteocyte lacuna size and shape in women with and without osteoporotic fracture. Journal of Biomechanics, 37:563–572, 2004.

3.2 Large-scale quantification of human osteocyte lacunar morphological biomarkers as assessed by ultra-high-resolution desktop micro-computed tomography

Elliott Goff[1], Federica Buccino[1], Chiara Bregoli[1], Jonathan P. McKinley[1,2], Basil Aeppli[1], Robert R. Recker[3], Elizabeth Shane[4], Adi Cohen[4], Gisela Kuhn[1], Ralph Müller[1]

[1] Institute for Biomechanics, ETH Zurich, Zurich, Switzerland

[2] Department of Mechanical Engineering, University of California Berkeley, Berkeley, CA, USA

[3] Department of Medicine, Creighton University Medical Center, Omaha, NE, USA

[4] Department of Medicine, Columbia University College of Physicians & Surgeons, New York, NY, USA

Published in:

Bone (2021)

https://doi.org/10.1016/j.bone.2021.116094

Postprint version according to publisher copyright policy

Abstract

Ultra-high-resolution imaging of the osteocyte lacuno-canalicular network (LCN) three-dimensionally (3D) in a high-throughput fashion has greatly improved the morphological knowledge about the constituent structures – positioning them as potential biomarkers. Technologies such as serial focused ion beam/scanning electron microscopy (FIB/SEM) and confocal scanning laser microscopy (CLSM) can image in extremely high resolution, yet only capture a small number of lacunae. Synchrotron radiation computed tomography (SR-CT) can image with both high resolution and high throughput but has a limited availability. Desktop micro-computed tomography (micro-CT) provides an attractive balance: high-throughput imaging on the micron level without the restrictions of SR-CT availability.

In this study, accuracy, reproducibility, and sensitivity of large-scale quantification of human osteocyte lacunar morphometries were assessed by ultra-high-resolution desktop micro-computed tomography. For this purpose, thirty-one transiliac human bone biopsies containing trabecular and cortical regions were imaged using ultra-high-resolution desktop micro-CT at a nominal isotropic voxel resolution of 1.2µm. The resulting 3D images were segmented, component labeled, and the following morphometric parameters of 7.71 million lacunae were measured: Lacunar number (Lc.N), density (Lc.N/BV), porosity (Lc.TV/BV), volume (Lc.V), surface area (Lc.S), surface area to volume ratio (Lc.S/Lc.V), stretch (Lc.St), oblateness (Lc.Ob), sphericity (Lc.Sr), equancy (Lc.Eq), and angle (Lc.θ).

Accuracy was quantified by comparing automated lacunar identification to manual identification. Mean true positive rate (TPR), false positive rate (FPR), and false negative rate (FNR) were 89.0%, 3.4%, and 11.0%, respectively. Regarding the reproducibility of lacunar morphometry from repeated measurements, precision errors were low (0.2 – 3.0%) and intraclass correlation coefficients were high (0.960 – 0.999). Significant differences between cortical and trabecular regions ($p<0.001$) existed for Lc.N/BV, Lc.TV/BV, local lacunar surface area (<Lc.S>), and local lacunar volume (<Lc.V>), all of which demonstrate the sensitivity of the method and are possible biomarker candidates. This study provides the foundation required for future large-scale morphometric studies using ultra-high-resolution desktop micro-CT and high-throughput analysis of millions of osteocyte lacunae in human bone samples.

Keywords:

micro-CT, lacuna, morphometry, large-scale, human, osteocyte

Abbreviations:

- LCN: lacuno-canalicular network
- FIB/SEM: focused ion beam/scanning electron microscopy
- CLSM: confocal laser scanning microscopy
- SR-CT: synchrotron radiation computed tomography
- micro-CT: micro-computed tomography
- DXA: dual-energy x-ray absorptiometry
- BMD: bone mineral density
- PMMA: polymethylmethacrylate
- FOV: field of view
- SNR: signal to noise ratio
- IPL: image processing language software
- TMD: tissue mineral density
- BV: bone volume
- BV/TV: bone volume / total volume
- < >: denotes local lacunar parameter
- [ ]: denotes population lacunar parameter
- Lc.N/BV: lacunar density
- Lc.N: lacunar number
- Lc.TV: lacunar total volume
- Lc.TV/BV: lacunar porosity
- Lc.V: lacunar volume
- Lc.S: lacunar surface area
- Lc.St: lacunar stretch
- Lc.Ob: lacunar oblateness
- Lc.Eq: lacunar equancy
- Lc.Sr: lacunar sphericity
- Lc.θ: lacunar angle
- TPR: true positive rate
- FPR: false positive rate
- FNR: false negative rate
- DOF: degrees of freedom
- PE: precision error
- ICC: intraclass correlation coefficient
- σ_{PMMA}: standard deviation of the image background
- CTX: C-terminal telopeptide of type 1 collagen
- P1NP: Procollagen type I N-terminal propeptide

3.2.1 Introduction

Bone as an organ provides humans with the necessary structural support to sustain locomotion and dynamic movement in daily life. The organ is uniquely capable of adapting its structure to meet the mechanical demands that are placed upon it [1]. This adaptation of bone has been described by Roux as bone (re)modeling [2]. Central to this process are the osteocytes: the most abundant bone cell type, embedded deeply within the bone matrix, and each ensconced within individual compartments called lacunae [2, 3]. Woven together by a large number of dendrites that extend from each cell, the lacuno-canalicular network (LCN) is one of the most intricately connected networks in the human body, and the scale is comparable with the network of neurons in the human brain [4]. Compelling studies over the last thirty years have revealed and emphasized the functional importance of the cells and processes within the LCN to sense mechanical signals, to transduce them into chemical signals, and to orchestrate the bone (re)modeling process through guided bone formation and bone resorption [5-10].

After cell death, the fossilized lacuna remains intact, allowing the lacuna's three-dimensional (3D) geometry to be extracted via several imaging techniques at the sub-micrometer resolution. Today, serial focused ion beam/scanning electron microscopy (FIB/SEM) possesses the highest spatial resolution in the nanometer range. Yet, while this technology allows for features like individual dendritic processes to be resolved, the depth range is a major limitation, and only a few dozen lacunae in the tissue can be captured simultaneously [11-14]. Other researchers have implemented confocal laser scanning microscopy (CLSM) to investigate lacunar geometry in mice [15, 16] and in clinical bone biopsies [17], but again the shallow tissue depth that can be explored is a limitation and hence only small subsections of bone consisting of a few dozen to a few hundred lacunae can be measured with CLSM. Both FIB/SEM and CLSM suffer from a lack of scalability since the time required for a study with more than a few hundred lacunae makes the technologies impractical for any type of large-scale lacunar analysis. Alternatively, several groups have used high-resolution x-ray-based approaches such as synchrotron radiation computed tomography (SR-CT). Several studies, Mader et al. [18] in particular, have been successful in separating the porous lacunae from the surrounding matrix in a high-throughput fashion in complete intact mouse femurs [18-24]. However, SR-CT is an imaging tool that requires access to a beamline facility, of which only a few in the world exist, and hence the availability is limited for most researchers due to timing restrictions. A fourth imaging tool,

conventional x-ray based ultra-high-resolution desktop micro-computed tomography (micro-CT), provides a reasonable balance between CLSM and SR-CT. Ultra-high-resolution desktop micro-CT allows for the extraction of millions of lacunae from complete bone biopsies without the need to request approval for limited time slots or experienced personnel at beamline facilities. Furthermore, desktop micro-CT is an established and validated technology that has been implemented for laboratory-based bone research for several decades [25-28]. Therefore, it is necessary that a technique be developed for large-scale, high-throughput imaging of osteocyte lacunar networks in clinical bone biopsies.

Equally as important as the 3D images acquired are the individual structures that are extracted from these images as well as the accurate, reproducible, and sensitive quantification of their morphometry. Specifically, with ultra-high-resolution osteocyte imaging, it is imperative that the lacunar morphometric parameters are well defined and measured accordingly. Great strides have been made towards the standardization of these metrics in recent years, and several studies have explored different basic measures such as lacunar density, shape, and orientation [18, 20, 21, 29-34]. Mader et al. have most thoroughly described and validated both simple and abstract lacunar morphometric parameters, and hence this study follows their naming convention and mathematical definitions [18]. The combination of well-defined lacunar morphometric parameters and a validated imaging and analysis methodology allow for the emergence of biomarkers. These morphometric biomarkers have the potential to be used to differentiate between diseased and healthy bone, old and young bone, or even the region of bone within the body.

This study aims to provide researchers with a reliable method of large-scale lacunar imaging, accurate automated identification, and measurements of each resulting 3D lacunar structure using a technology that is widely accessible – ultra-high-resolution desktop micro-CT. Furthermore, we demonstrate the power of such a high-throughput analysis by measuring the morphometric parameters of millions of osteocyte lacunae in human bone samples, using the previously validated 3D lacunar metrics of Mader et al. [18]. The rigor of the method is confirmed by accurate lacunar identification, a standard precision study [35], and the sensitive detection of differences between cortical and trabecular regions. The demonstrated validation highlights the value of the imaging method, and we believe this study will provide a rigorous foundation for future large-scale lacunar investigations.

3.2.2 Materials and Methods

Human bone biopsy preparation

Thirty-one transiliac bone biopsy samples from premenopausal women already described in previous studies by Cohen et al. [36, 37] were used for this study. Biopsy samples had been obtained in women, aged 18-48, recruited as a reference population for studies of bone structure and metabolism in premenopausal women. Reference population subjects were required to have normal areal spine, hip, and forearm BMD by dual-energy x-ray absorptiometry (DXA; Z score ≥ -1.0 at all sites), no history of adult low trauma fracture, and no historical or biochemical evidence of diseases or conditions known to affect skeletal integrity [36, 37]. All subjects provided written informed consent; studies had been approved by the institutional review boards of all participating institutions.

A hemi-cylinder fraction of each biopsy core, containing both cortical and trabecular regions, was embedded in individual polymethylmethacrylate (PMMA) disks with a 25mm diameter. Subsections of each sample were prepared to fit in the desktop micro-CT scanner, which limits the diameter to a 4.0mm field of view (FOV) in the ultra-high-resolution mode. Hence, each PMMA embedded core was cut three times parallel to the longitudinal axis of the biopsy using a circular diamond blade (SCAN-DIA Minicut 40, SCAN-DIA GmbH & Co. KG, Germany) and custom-made mounts for sample fixation. This produced a rectangular block, which had the XY target dimensions of 4.25 +/- 0.1mm with the Z dimension depending on the original placement in the PMMA disk and ranging from 20-25mm. Each block was then turned on a conventional lathe (Schaublin 102, Bevilard, Switzerland) to create a final cylinder of 3.8 +/- 0.05mm diameter and a length ranging between 10 and 15mm. The biopsy cylinder was then tightly fit into a custom sample holder as seen in Figure 3.2.1 to minimize motion artifacts and to maximize the volume scannable within the 4.0mm diameter FOV.

Imaging acquisition

Biopsy subsamples were imaged with a µCT50 (Scanco Medical AG, Brüttisellen, Switzerland), operated with a 0.5mm aluminum filter, 72µA current, 4W power, 55kVp energy, 1.5s integration time, level 6 data averaging, and with a total of 1500 projections. Images were reconstructed at a nominal isotropic voxel resolution of 1.2µm with an anti-ring level 8 to minimize center ring artifacts using the manufacturer's scanner software. Each image consisted

of a cylindrical volume equal to the full diameter of the sample (3.8 +/- 0.05mm) and the height of one scan stack (909 slices = 1.09mm). The protocol for each sample consisted of three scans: 1. Prescan to warm the sample in the scanner gantry in an effort to reduce motion artifacts caused by thermal effects (1 hour) 2. Cortical region scan starting from the lowest point on the centerline of the sample and scanning up one stack (10 hours) 3. Trabecular region scan stack in the middle of the biopsy equidistant between both cortical walls (10 hours). A visual example of this scanning protocol and resulting images can be seen in Figure 3.2.1.

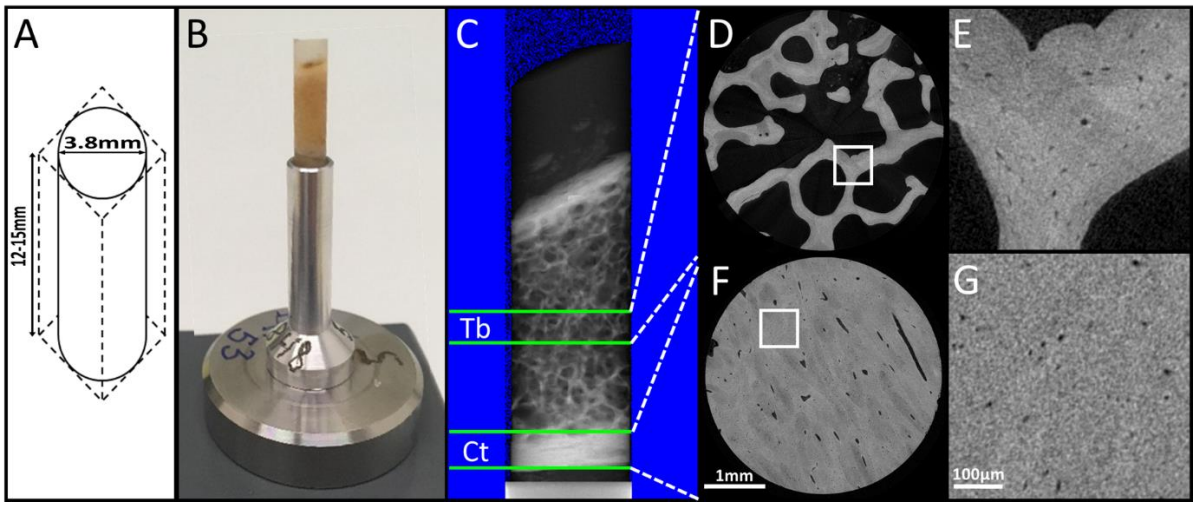

Figure 3.2.1: A) Schematic of sample core extraction from hemi-cylinder biopsy, which consisted of three linear cuts followed by a lathe turn. B) Photograph of final machined biopsy core inserted into a tolerance-fit sample holder. C) Scout-view overview of entire sample (XZ plane) with the trabecular (Tb) and cortical (Ct) scanned regions identified between the respectively labeled green lines. D) Ultra-high-resolution micro-CT scan of trabecular region cross-section (XY plane) and E) enlarged trabecular subregion. F) Ultra-high-resolution micro-CT scan of cortical region cross-section (XY plane) and G) enlarged cortical subregion.

To determine the optimal beam energy, three samples of trabecular bone were scanned at three beam energies: 55, 70, and 90kVp. These samples used for beam energy optimization originated from a separate study [38]; however, they were also human bone biopsies from the iliac crest and were considered to be comparable with our biopsy group. We aimed to maximize the image signal-to-noise ratio (SNR) just as previous studies relating to other anatomical bone sites had done [39]. The linear attenuation coefficient (raw signal) was measured for ten two-dimensional sub-regions (~0.25mm^2) at every beam energy in three samples for 90 regions in total. SNR was then calculated by adapting the Firbank equation to account for two distinct materials as

described in Equation 3.2.1 where μ is the average coefficient of linear attenuation of bone and the background (PMMA) and σ is the standard deviation of the background [40].

$$SNR = 0.655 \frac{\mu_{bone} - \mu_{PMMA}}{\sigma_{PMMA}} \quad (3.2.1)$$

Image preprocessing

Preprocessing of each image consisted of a constrained 3D Gaussian low pass filter (σ=0.8, support =1) to reduce noise and was applied using IPL (Scanco Medical AG, Brüttisellen, Switzerland). Segmentation of lacunar structures was performed by inverting the image after applying a threshold that was individualized for each image volume, which was necessary due to the large variation in tissue mineral density (TMD) distributions between samples at this resolution. The lacunar threshold was determined by fitting a Gaussian distribution to each sample's raw TMD distribution data and calculating the first critical point (g') of the fitted distribution using a custom Python script (3.7.1, Python Software Foundation, Delaware, USA). Bone volume (BV) was determined by fixing a threshold of 520mg HA/ccm, applying to all samples, performing a closing operation, and calculating the resulting BV using IPL software (Scanco Medical AG, Brüttisellen, Switzerland).

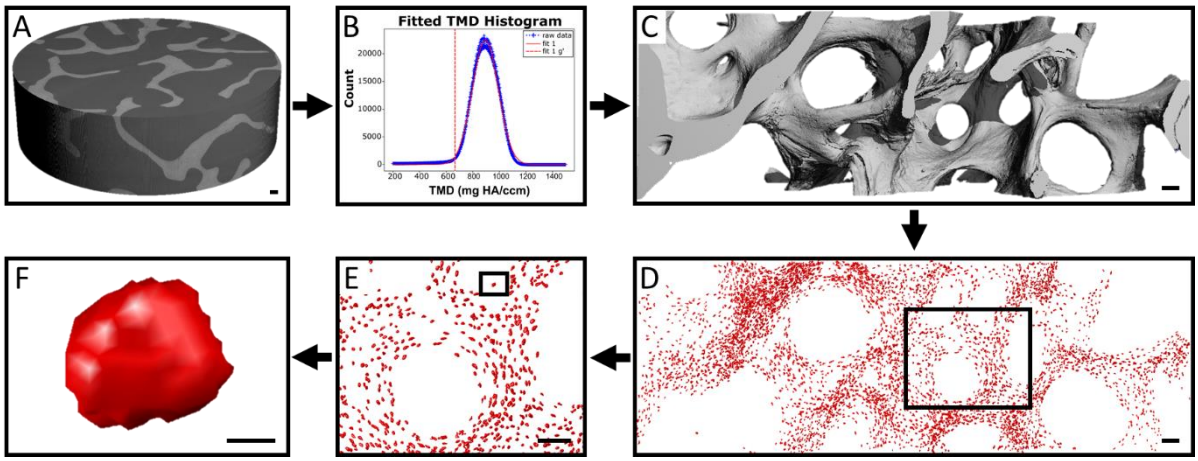

Figure 3.2.2: Visual overview of large-scale lacunar segmentation. A) Gaussian filtered, unsegmented, complete micro-CT image stack. B) Sample specific histogram of tissue mineral density (TMD) values fitted by a Gaussian function. A unique lacunar threshold is chosen for each sample at the first critical point of the respective fit by calculating the maximum of the first derivative (g'). C) Lacunar threshold calculated with (B) applied to (A). D) Image (C) inverted and component labeled to identify lacunae. E) Enlarged subregion group of lacunae. F) Single visualized lacuna. Scale bar lengths: A-E) 100μm F) 10μm.

All objects smaller than 50µm^3 and larger than 2000µm^3 were removed as to reflect the range of human lacunar volumes reported in previous histological studies [41]. The lower bound filters out noise structures while the upper bound excludes larger porosities like Haversian and Volkmann canals. Similar volumetric ranges have also been implemented in previous studies [42, 43]. Several microcracks, blood vessels, and image ring artifacts escaped the volumetric filter, yet all exhibited similar thin structures with a high object-elongation value. Therefore, these were excluded by removing all objects with an elongation above a threshold (Lc.St > 0.85). All objects sharing a border with the image edge were also removed to exclude partially cutoff objects.

Image morphometry

The lacunar morphometries were calculated with a custom Python script, which first component labeled all lacunar objects, applied a surface mesh to each, and then measured basic individual parameters. Lacunar density (Lc.N/BV) was calculated by normalizing the number of lacunae (Lc.N) to the bone volume (BV) and lacunar porosity (Lc.TV/BV) by dividing the total volume of all lacunae by the respective BV. Local parameters (denoted with <> and first defined by Stauber et al. [44]) were each normalized to the sample Lc.N while population-based parameters (denoted with []) were not normalized. Individual lacunar volume (Lc.V), lacunar surface area (Lc.S), and the Eigen vectors were determined from the object specific mesh. This mesh was calculated by performing a triangulation of the surface voxels of the object using Lewiner marching cubes (3.7.1, Python Software Foundation, scikit-image library, Delaware, USA). The Eigen vectors were then used to quantify more complex parameters including lacunar stretch (Lc.St) and lacunar oblateness (Lc.Ob), which were first defined by Mader et al. [18]. Lacunar equancy (Lc.Eq) was the ratio between the smallest and largest Eigen vectors (E3/E1) [21, 45] while lacunar sphericity (Lc.Sr) related the lacunar object to a sphere via the ratio between Lc.S and Lc.V [43]. Lacunar angle (Lc.θ) was measured in degrees and ranged between 0 and 180 degree in relation to an arbitrarily created unit vector that was held consistent between images.

Validation: Accuracy of automated lacunar identification

To evaluate the accuracy of the automated threshold approach, lacunae from five sample sub-volumes consisting of roughly 200 lacunae per region were manually identified by a trained observer by moving through stacks of slices and then compared with the automatically

identified lacunae at the corresponding sample-specific g' threshold to calculate true positive, false positive, and false negative rates (TPR, FPR, FNR). All objects were verified in 3D as depicted in Figure 3.2.3 and falsely classified objects were reclassified when appropriate. The geometry of false negatives was evaluated in 2D while the respective center voxel position of the objects could be evaluated in 3D in relation to successfully segmented true positive and false positive objects. Objects which were characterized as false positives typically were jagged, irregular in shape, and did not generally resemble lacunae in both 2D and 3D.

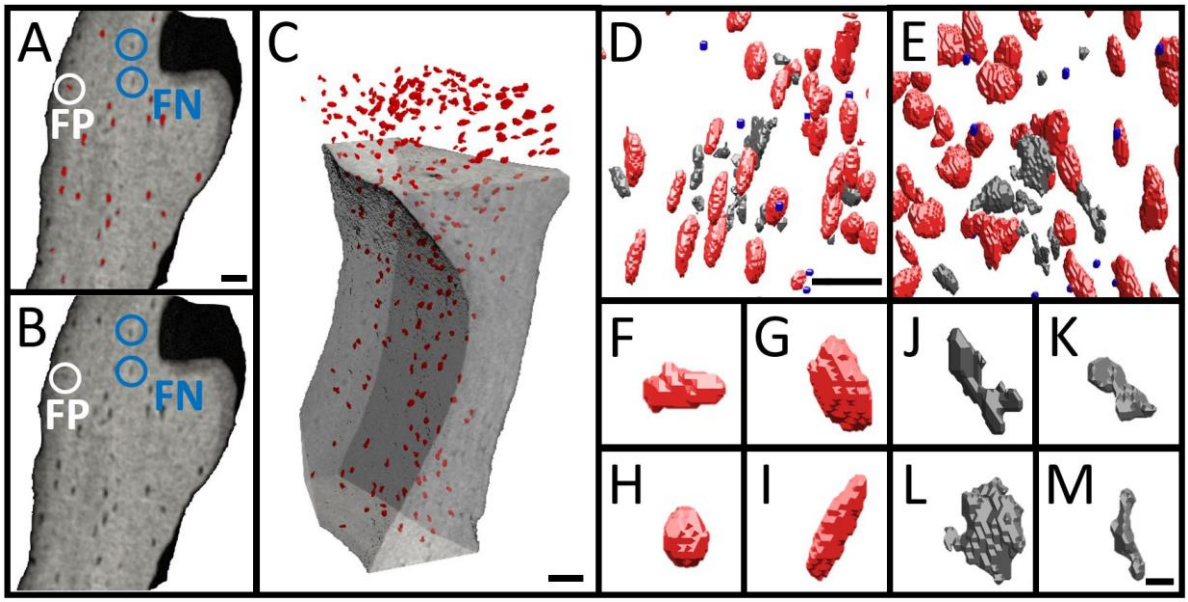

Figure 3.2.3: Manual vs. automatic lacunar identification. A) 3D cutplane of trabecular subregion with automatically segmented objects highlighted in red. Examples of false negatives (FN) circled in blue, false positives (FP) circled in white. B) Same cutplane as (A) used for visual comparison regarding classification of automatically segmented objects, showing same FP and FN as in (A). C) 3D orthographic projection of (A&B) with automatically segmented objects in red. D&E) 3D visualization comparing manual and automatic lacunar identification. Red objects = true positives (TP); objects identified as lacunae both manually and automatically. Gray objects = false positives (FP); objects identified as lacunae automatically but rejected manually. Blue spheres = false negatives (FN); center voxel of objects manually identified as lacunae but rejected by the automatic method. F-I) TP examples. J-M) FP examples. Scalebar A-E) = 50µm; F-M) = 10µm.

Validation: Reproducibility of repeated measurements

In accordance with repeated measurements literature that recommends a sufficient number of degrees of freedom (DOF) to produce an upper confidence limit of the precision error that is

40% greater than the mean precision error [35], six samples were measured five times and repositioned between each measurement for a total of 20 DOF. Reproducibility of repeated measurements was evaluated by calculating the precision error ($PE_{\%CV}$) using Equation 3.2.2 – 3.2.3 where m is the quantity of subjects, SD represents the standard deviation of m repeated measures on subject j, and CV is the coefficient of variation. The intraclass correlation coefficient (ICC) for the measured lacunar indices was calculated using Equation 3.2.4 where n represents the number of repetitions and F_0 represents the ratio of the residual within-subject mean squares and the between-subject mean squares.

$$PE_{SD} = \sqrt{\sum_{j=1}^{m} \frac{SD_j^2}{m}} \tag{3.2.2}$$

$$PE_{\%CV} = \sqrt{\sum_{j=1}^{m} \frac{\%CV_j^2}{m}} \tag{3.2.3}$$

$$ICC = \frac{F_0 - 1}{F_0 + (n-1)} \tag{3.2.4}$$

Validation: Sensitivity to biological differences

To assess the method's sensitivity to biological differences, lacunar morphometric parameters from cortical and trabecular regions were compared as there are known physiological differences between the distribution and shape of lacunae in these regions in humans [43, 46]. Because each individual biopsy contained both cortical and trabecular regions, it was possible to compare lacunae both within samples and between samples. This sensitivity analysis was

inspired by the previous work of Nebuloni et al. [47] and we extend the definition here to be the ability to detect biological differences, in this case regional lacunar differences, which have been previously identified [43,46].

Statistical analysis

A paired Student t-test with the necessary Bonferroni correction was performed with respect to energy-dependent imaging parameters in Table 3.2.1. With respect to the precision test, the 95% confidence interval was calculated for each morphometric parameter using a chi-squared distribution to gain an understanding of certainty with respect to the PE and ICC reported values in Table 3.2.3. Creating two-parameter plots of the data presented in Table 3.2.3 is another way to evaluate the reproducibility of the imaging method by means of clustering as is depicted in Figure 3.2.5. A paired Student's t-test was performed to evaluate regional differences between lacunar parameters that were normalized to tissue indices ($p<0.001$). Population-based parameters were not normally distributed following a Kolmogorov-Smirnov test, and so a non-parametric Mann-Whitney U test was performed to evaluate population differences ($p<0.001$). The inter-quartile ranges and medians were computed for each morphometric parameter.

3.2.3 Results

Image acquisition

Images captured with a 55kVp beam energy exhibited a significantly higher SNR when compared to images obtained with a beam energy of 90kVp ($p<0.005$). The SNR measured with the 70kVp beam energy fell in between the high and low beam energy values and did not differ significantly from the other energies.

Table 3.2.1: Energy dependency of imaging parameters. Energy level 55kVp used as baseline and paired t-test with the necessary Bonferroni correction used to test for significant differences between energy levels in the three following categories: contrast, standard deviation of the image background (σ_{PMMA}), and signal-to-noise ratio (SNR). Significantly different ($p<0.005$) from baseline denoted with (*) and from 70kVp with (#).

Energy (kVp)	**Contrast (n=30)**	**σ_{PMMA} (n=30)**	**SNR (n=30)**
55	1.84±0.46	0.14±0.02	8.34±2.20
70	1.33±0.33*	0.11±0.01*	7.65±1.88
90	0.92±0.23*#	0.09±0.01*#	6.67±1.60*

As shown in Table 3.2.1, both contrast and standard deviation of the background (PMMA in this case) were inversely proportional to the beam energy. Specifically, the inverse proportionality was approximately linear with contrast while σ_{PMMA} was quadratic (Figure 3.2.4), both important for the computation of SNR as given in Equation 3.2.1. As a ratio of both noise and the standard deviation of the image background (Equation 3.2.1), SNR was less dramatically affected by increasing beam energy. We therefore set the beam energy to 55kVp for all scans in the study because this setting produced the highest quality images with the highest contrast at acceptable noise levels.

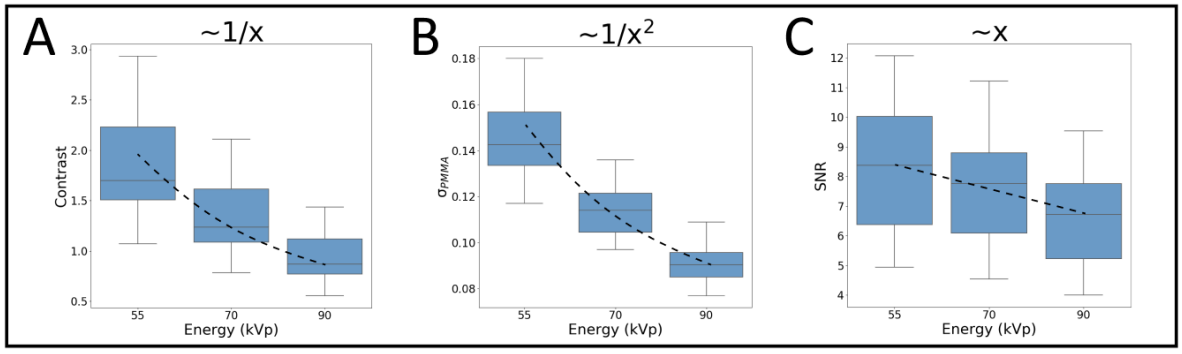

Figure 3.2.4: Beam physics relationships. Ten subregions measured at each energy (30 measurements in total). A) Contrast exhibits an inverse relationship with beam energy. B) Standard deviation of the background (σ_{PMMA}) has an approximate quadratic relationship with beam energy. C) Signal-to-noise ratio is linearly related to beam energy as expected since it is defined as the contrast divided by the σ_{PMMA}.

Validation: Accuracy of automated lacunar identification

Automatically identified objects were compared with the manually identified objects to evaluate the true positive rate (TPR), false positive rate (FPR), and false negative rate (FNR) measures as seen in Table 3.2.2. Objects identified automatically in each sample revealed a strong agreement with the lacunae counted manually as is evident by the high TPR and low FPR and low FNR. Roughly 200 lacunae were present in each sample subregion with sample 1 exhibiting the highest TPR (93.9%) and lowest FNR (6.1%). Sample 4 had the lowest FPR (0.5%) while sample 3 the lowest TPR (77.3%). The final lacunar identification accuracy measure was calculated as the mean of the five samples and was computed to be 89.0% TPR, 3.4% FPR, and 11.0% FNR.

Table 3.2.2: Quantification of accuracy measures and their corresponding rates obtained via comparison between manual and automatic lacunar identification methods. TPR = True Positive Rate; FPR = False Positive Rate; FNR = False Negative Rate.

Sample	**TP**	**FP**	**FN**	**TPR (%)**	**FPR (%)**	**FNR (%)**
1	155	9	10	93.9	5.5	6.1
2	182	11	14	92.9	5.7	7.1
3	133	3	39	77.3	2.2	22.7
4	202	1	16	92.7	0.5	7.3
5	205	7	27	88.4	3.3	11.6
Mean	175	6	21	89.0	3.4	11.0

Validation: Reproducibility of repeated measurements

Repeated measures reproducibility is crucial for validation and was quantified for lacunar indices. Across all lacunar morphometric parameters, precision errors were very low (below 3%) and the ICC were very high (above 0.980), which indicate that the measurements of these lacunar parameters are extremely reproducible. The 95% confidence interval range for precision errors was between 0.67% and 3.68% while the range for ICC values were between 0.883 and 1.000, which indicates extremely low measurement variability and high reproducibility.

Table 3.2.3: Reported values from the reproducibility analysis (n=6, five repeated measurements). Morphometric parameters include: lacunar total volume (Lc.TV), lacunar porosity (Lc.TV/BV), lacunar number (Lc.N), lacunar density (Lc.N/BV), local lacunar volume (<Lc.V>), local lacunar surface area (<Lc.S>), local lacunar stretch (<Lc.St>), local lacunar oblateness (<Lc.Ob>), local lacunar sphericity (<Lc.Sr>), local lacunar equancy (<Lc.Eq>), and local lacunar angle (<Lc.θ>). In addition to mean values of each morphometric parameter across the samples, we report the following for precision errors (PE): standard deviation (PE_{SD}) in absolute values, coefficient of variation ($PE_{\%CV}$) of the repeated experiments, and the 95% confidence interval of the variation (95% CI $PE_{\%CV}$). Also reported are the intraclass correlation coefficients (ICC) and the 95% confidence interval of the ICC for each respective morphometric parameter.

Morphometric parameter	**Mean**	**PE_{SD}**	**$PE_{\%CV}$**	**95% CI $PE_{\%CV}$**	**ICC**	**95% CI ICC**
Lc.TV (1000*µm^3)	2,119.3	40.2	2.77%	2.11-4.05%	0.997	0.992-1.000
Lc.TV/BV (%)	0.5	0.009	2.52%	1.91-3.68%	0.989	0.966-0.998
Lc.N (1000)	10.03	0.2	1.86%	1.41-2.72%	0.999	0.996-1.000
Lc.N/BV (1000/mm^3)	22.09	0.3	1.48%	1.12-2.16%	0.984	0.952-0.997
<Lc.V> (µm^3)	210.5	2.5	1.33%	1.01-1.95%	0.991	0.970-0.999
<Lc.S> (µm^2)	207.5	1.7	0.88%	0.67-1.29%	0.990	0.968-0.998
<Lc.St> (1)	0.6	0.001	0.17%	0.13-0.25%	0.989	0.963-0.998
<Lc.Ob> (1)	-0.4	0.006	1.59%	1.21-2.32%	0.960	0.883-0.994
<Lc.Sr> (1)	0.8	0.002	0.24%	0.18-0.35%	0.938	0.816-0.990
<Lc.Eq> (1)	0.3	0.001	0.43%	0.33-0.63%	0.994	0.980-0.999
<Lc.θ> (Degree)	113.8	0.8	0.66%	0.50-0.97%	0.980	0.938-0.997

Clustering of the individual repeated measurements indicates reproducibility of lacunar morphometry and is especially apparent in Figure 3.2.5A-B. These parameters also exhibited a very high correlation, which illustrated that as bone volume increases so will the number of lacunae and the total lacunar volume. The clustering in Figure 3.2.5C-D was not nearly as evident across all six samples due to the fact that <Lc.V> and <Lc.St> were more difficult to reproduce. As BV/TV increases in Figure 3.2.5C-D, measured variability decreases between the first and second cluster and then remains approximately constant. The strong correlation of Lc.N (R^2 = 0.99) and Lc.TV (R^2 = 0.98) with BV/TV position them as potential lacunar biomarker candidates. <Lc.V> and <Lc.St> were more independent of BV/TV and no correlation was found.

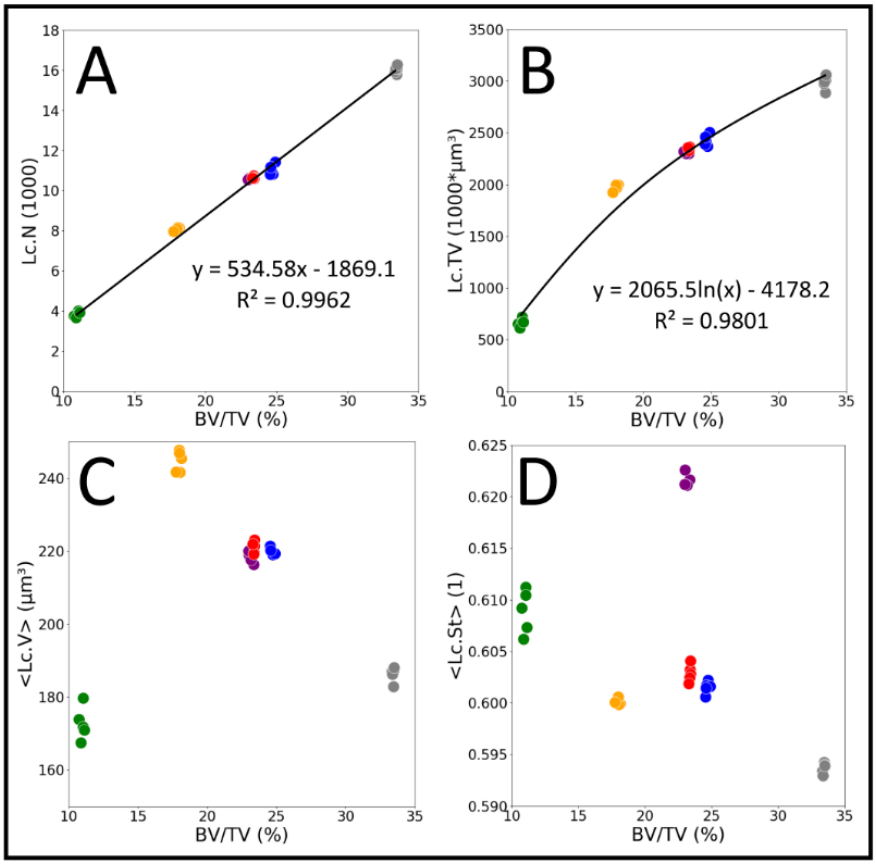

Figure 3.2.5: Two-parameter plots that demonstrate the reproducibility of the imaging method. Each color represents an individual sample and each data point represents a specific measurement (n=6, with 5 repeated measurements). A) Lacunar number (Lc.N) vs. bone volume (BV/TV). B) Lacunar total volume (Lc.TV) vs. bone volume (BV/TV). C) Local lacunar volume (<Lc.V>) vs. bone volume (BV/TV). D) Local lacunar stretch (<Lc.St>) vs. bone volume (BV/TV).

Validation: Sensitivity to biological differences

Cortical and trabecular bone regions were measured and compared to evaluate the sensitivity of the method to biological differences. More bone was present, and consequently, more lacunae were present in cortical bone when compared to trabecular bone. Measured tissue values such as BV, and BV/TV in trabecular regions were consistently lower than cortical regions as expected since trabecular bone is sparse and cortical bone is compact. Regarding the global morphometries, which were normally distributed, Lc.N/BV median value in trabecular bone was nearly half of what it was observed to be in cortical bone (16,611 vs. 26,429, $p<0.001$). Similarly, the median value of Lc.TV/BV in trabecular bone was also nearly half of what it was in cortical bone (0.30% vs. 0.58%, $p<0.001$), again indicating that cortical bone has a significantly higher lacunar porosity than trabecular bone. Furthermore, we report in Table 3.2.4 that the normalized local parameters <Lc.V> and <Lc.S> are significantly greater ($p<0.001$) in cortical bone (<Lc.V> = 223μm^3 ; <Lc.S> = 233μm^2) than in trabecular bone (<Lc.V> = 178μm^3 ; <Lc.S> = 194μm^2). Most population-based morphometric parameters were not normally distributed, and consequently we reported the median values as well as the interquartile range for all indices to provide a sense of the distribution of each parameter in Table 3.2.4.

Table 3.2.4: Large-scale lacunar morphometric parameters (n=6.57 million for cortical and n=1.14 million for trabecular). Reported values are the median with interquartile range (25^{th} percentile – 75^{th} percentile). Morphometric parameters include: total image volume (TV), total bone volume (BV), ratio of bone volume to total volume (BV/TV), lacunar porosity (Lc.TV/BV), lacunar number (Lc.N), lacunar density (Lc.N/BV), local lacunar volume (<Lc.V>), local lacunar surface area (<Lc.S>), population lacunar volume ([Lc.V]), population lacunar surface area ([Lc.S]), population lacunar surface area to volume ratio ([Lc.S/Lc.V]), population lacunar stretch ([Lc.St]), population lacunar oblateness ([Lc.Ob]), population lacunar sphericity ([Lc.Sr]), population lacunar equancy ([Lc.Eq]), and population lacunar angle ([Lc.θ]). Paired t-test performed for the normally distributed global and local parameters, (*) indicates p<0.001. Mann-Whitney U test performed on population-based parameters and (*) indicates p<0.001.

Morphometric parameter	**Trabecular**	**Cortical**
TV (mm^3)	15.7 (15.1–15.8)	15.7 (15.6–15.9)
BV (mm^3)	2.11 (1.54–2.46)*	7.68 (6.33–9.70)
BV/TV (%)	14.0 (10.2–18.4)*	57.8 (43.7–64.9)
Lc.TV/BV (%)	0.30 (0.22–0.38)*	0.58 (0.51–0.65)
Lc.N (1000)	41.2 (27.7–67.9)*	252 (175–266)
Lc.N/BV ($1000/mm^3$)	16.6 (14.1–18.7)*	26.4 (23.7–29.3)
<Lc.V> (μm^3)	178 (159–197)*	223 (189–245)
<Lc.S> (μm^2)	194 (178–211)*	233 (216–248)
[Lc.V] (μm^3)	123 (70.1–230)*	116 (63.0–272)
[Lc.S] (μm^2)	161 (109–245)*	164 (105–290)
[Lc.S]/[Lc.V] (1/μm)	1.30 (1.05–1.56)*	1.41 (1.06–1.66)
[Lc.St] (1)	0.62 (0.53–0.69)*	0.61 (0.51–0.69)
[Lc.Ob] (1)	-0.44 (-0.67– -0.13)*	-0.49 (-0.71– -0.17)
[Lc.Sr] (1)	0.76 (0.70–0.81)*	0.73 (0.66–0.79)
[Lc.Eq] (1)	0.29 (0.19–0.45)*	0.31 (0.19–0.47)
[Lc.θ] (Degree)	104 (76.0–131)*	107 (77.4–134)

Population-based lacunar parameters were not normally distributed. The interquartile ranges between regions were similar, yet a non-parametric Mann-Whitney U test revealed significant differences between cortical and trabecular regions ($p<0.001$). The measure of sphericity ([Lc.Sr]) was approximately 0.75 for both regions of bone, indicating similarities between the measured ellipsoids and an idealized sphere. The additional parameters [Lc.Eq], [Lc.St] and [Lc.Ob] allow for the ellipsoidal lacunar shape to be described in more detail, and the median reported values suggest that these are indeed ellipsoidal structures in both trabecular and cortical regions. The range of [Lc.Ob] in trabecular bone was slightly higher than in cortical bone.

Figure 3.2.6 depicts selected global, local, and population-based morphometries from both cortical and trabecular regions. When normalized to the analyzed tissue volume, both the lacunar density and porosity were significantly different between cortical and trabecular regions (Figure 3.2.6A-B) across all 31 samples, further supporting their potential as biomarkers. Local morphometries (<Lc.V> & <Lc.S>) were also significantly different between the two regions (Figure 3.2.6C-D), yet not as clearly separated as the global morphometries. Population-based morphometries (Figure 3.2.6E-F) included all lacunar observations across all 31 samples: 1.14 million lacunae in trabecular bone and 6.57 million lacunae in cortical bone. The shape indices [Lc.St] and [Lc.Sr] were chosen to compare between regions and were also significantly different. A visual comparison is presented in Figure 3.2.6G-H between the samples containing the median Lc.N/BV values from Figure 3.2.6A, further illustrating the differences between anatomical regions.

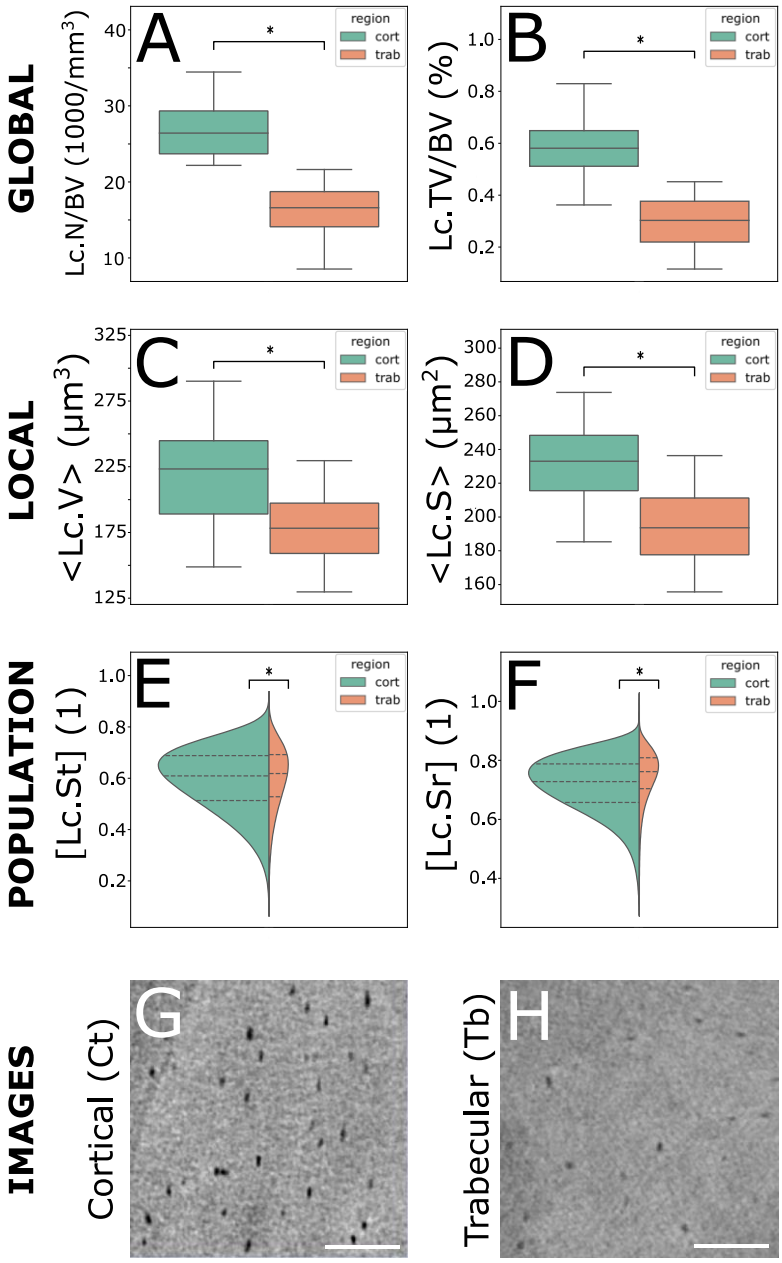

Figure 3.2.6: Comparison of cortical and trabecular regions regarding lacunar morphometric parameters. Included in the analysis were 31 samples which comprised of 6.57 million cortical lacunae and 1.14 million trabecular lacunae. A) Lacunar density (Lc.N/BV). B) Lacunar porosity (Lc.TV/BV). C) Local lacunar volume (<Lc.V>) normalized to sample. D) Local lacunar surface area (<Lc.S>) normalized to sample. E) Population-based local lacunar stretch ([Lc.St]) not normalized to sample. F) Population-based local lacunar sphericity ([Lc.Sr]) not normalized to sample. G&H) Micro-CT images from cortical and trabecular regions representing the median values from plot (A) respectively, scale bar = 100µm. Paired t-test performed on normalized parameter plots (A-D) and (*) indicates $p<0.001$. Mann-Whitney U test performed on population-based parameters (E-F) and (*) indicates $p<0.001$.

3.2.4 Discussion

Detailed examination of the LCN on a large scale demands a high-resolution 3D-imaging methodology that is accurate, reproducible, and sensitive. Lacunae must be identified accurately and morphometric indices measured repeatably. Therefore, it is paramount that researchers select a validated imaging methodology for the large-scale assessment of osteocyte lacunar morphometry. High-resolution desktop micro-CT is an ideal technology for large-scale investigation of the lacunar network due to its wide accessibility. Micro-CT has been employed for decades as a standard technology for bone tissue morphometry with nominal voxel resolutions in the range of 10-40μm [25-28]. However, this technology has evolved in recent years, and with it, the ability to image higher resolutions on the order of 1μm [48]. Hence, the development of validated image acquisition, processing, and analysis tools to image lacunar morphometry is a logical progression of the science as well as being crucial to understanding the biological impact of the LCN on bone at other hierarchical levels.

Identifying the lacunar structures to be analyzed required a landmark-based threshold to be applied to the image that accounted for sample-specific mineralization heterogeneities. Typically, a single threshold is chosen by the user via visual inspection and then applied to all samples in a study. At the tissue level this method is acceptable when recommended guidelines are carefully followed [49] and was how BV was calculated in this study. However, due to the wide variation of the TMD distributions between samples at the 1.2μm resolution, this single-threshold method cannot be applied to all samples when imaging lacunae (Figure 3.2.S1). Therefore, our approach was to pragmatically locate a threshold that was intrinsically linked to the sample specific TMD distribution, compare the resulting lacunar identification with manual identification, and quantify the accuracy. Previous studies have tried similar individual threshold approaches, which are offset from a reference point of the TMD histogram such as the mean [50], but we found our specific images responded best to selecting the TMD histogram critical point as a landmark for segmentation (Figure 3.2.S1). In addition, the critical point is a clear and calculable landmark on every TMD histogram, which is less prone to error than an offset. This produced an adequate automated segmentation of lacunar structures as is depicted in Figure 3.2.3. Alternative descriptors of the TMD distribution were investigated such as the width of the distribution but did not prove to be as effective as the first critical point (Figure 3.2.S2). It is important to note that the TMD distribution can be very heterogeneous around

osteocyte lacunae and that adjustments to the algorithm would need to be made when investigating topics like osteocytic osteolysis which changes the mineral surrounding the lacunar structures. The μCT50 machine was calibrated weekly with a multi-material phantom to minimize measurement errors with respect to scaling the raw signal attenuation to values of hydroxyapatite for the TMD histograms.

The range of considered object volumes was also important for lacunar identification. This range varies substantially between studies and could be as narrow as 50-610μm^3 or as wide as 175-2000μm^3 [18, 21, 42, 43, 51, 52]. Previous examinations of histological slides have estimated the human lacunae to be between 28μm^3 and 1713μm^3, yet lacunae observed below 50μm^3 were only found in fracture callus [41]. After evaluating several different volume ranges and comparing both qualitatively with 2D and 3D images and quantitatively with accuracy measures such as TPR, FPR, and FNR, we determined a lower limit of 50μm^3 to be optimal for lacunar identification in human trabecular and cortical bone [53]. The upper limit was chosen to be 2000μm^3 in line with a similar study [21]. This range has a large impact on the number of lacunae analyzed and is particularly sensitive on the lower limit. This problem is especially pronounced with respect to desktop micro-CT due to the limited photon count of its X-ray beam technology. Relative to studies conducted with synchrotron CT systems [18, 42], the desktop micro-CT X-ray beam creates image projections with fewer photons, which increases the resulting noise, reduces the image quality, and makes visualization of small lacunae more difficult. A Gaussian filter with a low sigma value of 0.8 was applied so noise would be reduced while the borders of the lacunae would not be blurred beyond the recognition of a trained human observer. Several extremely elongated ring artifacts were observed in segmentations and were successfully removed by implementing an anti-ring reconstruction filter and applying a shape filter that removed objects with a Lc.St value greater than 0.85 [54].

We used ultra-high-resolution desktop micro-CT to image 7.71 million osteocyte lacunae across cortical and trabecular regions in 31 human iliac crest biopsies. We have observed that morphometric differences exist between lacunae in cortical and trabecular regions of bone, which has also been shown in previous studies [43, 46]. Currently, only Akhter et al. [43] have reported sample matched trabecular and cortical lacunar morphometric parameters in human iliac crest biopsies. In contrast to their study, we report higher values of Lc.N/BV and Lc.TV/BV in cortical bone when compared to trabecular bone. However, the narrow volume range they evaluate (50-610μm) and their analysis of less than 1% of the number of lacunae

that we examine severely limits the range of variation that they could potentially consider. Additionally, we have proven our desktop micro-CT imaging technique to be accurate for lacunar identification, reproducible for repeated measures, and sensitive for lacunar parameters between anatomically distinct regions.

We evaluated not only global lacunar parameters related to tissue measures (Figure 3.2.6A-B), but also local (Figure 3.2.6C-D) and population-based (Figure 3.2.6E-F) values. Population-based morphometry was not normalized and presents the reader with an undistorted perspective of the natural variation of certain morphometric indices across millions of lacunae (Figure 3.2.6E-F). This further illustrates the method's sensitivity to biological differences that we see in Figures 3.2.6A-D and also demonstrates the method's ability to capture the natural variation of lacunae in a large-scale analysis.

Manual identification was used as our gold-standard for calculating accuracy, because registration between micro-CT images and typical morphological gold-standards like histology is extremely difficult. However, we were careful to create the best manual identification dataset possible for comparison. Cresswell et al. have used similar accuracy comparisons in previous studies and in fact, achieve similar rates of TP, FP, and FN to ours [50]. Interestingly, sample 3 in our accuracy calculation exhibited an inordinately low TPR and high FNR. This was due to a suboptimal selection of the sample's subregion near the bone surface, which made manual identification of lacunae slightly more difficult. Ultimately, this resulted in a slight reduction of the overall accuracy of lacunar identification. We did not investigate the impact this poor sample had on the resulting segmented morphometry as we only used these five samples to evaluate the accuracy of our method relative to lacunar identification. FN objects could only be visualized in 2D as the machine incorrectly did not segment these objects. However, the 3D position of the center voxel in the FN objects could still be evaluated in relation to TP and FP objects as this was the coordinate of the voxel chosen by the trained observer. Objects determined to be FP resembled noise structures and were either image artifacts or non-lacunar micropores.

We observed very low precision errors and high intraclass correlation coefficients with respect to our five consecutive measurements of six samples. These values were in the same range as in the study of Hemmatian et al. who investigated the reproducibility of desktop micro-CT for imaging murine lacunae [48]. The tight clustering of data points when creating two-parameter

plots as seen in Figure 3.2.5 further proves the reproducibility of the method. Figure 3.2.5A and 3.2.5B both exhibit tight clustering within the measurements for each sample which is what we expect when comparing lacunar parameters with tissue values like BV/TV. Bone tissue volume is a quantity that micro-CT is excellent at measuring and hence we would expect it to be extremely reproducible. Physiologically speaking, we would also expect Lc.N and Lc.TV to increase with increasing total bone volume, which explains the strong correlation, further adds credibility to the imaging modality, and even positions the two lacunar parameters as potential biomarker candidates. Previous research has demonstrated osteocytic osteolysis plays a role in bone health, disease, and mechanisms of medication response; this also poises the lacunar microarchitecture as a potential biomarker from the perspective of osteocyte-controlled bone remodeling [55]. Furthermore, a variety of chemically-based bone biomarkers, such as serum CTX and P1NP, currently exist for the clinical assessment of osteoporosis/bone remodeling and lacunar parameters like Lc.N and Lc.TV could potentially be used in conjunction with those recently outlined by Kuo et al. for investigation of disease mechanisms [56]. Yet in Figure 3.2.5C and 3.2.5D, we note that the values of each sample are slightly less clustered in comparison with Figure 3.2.5A and 3.2.5B and are not correlated. More specifically, we note that BV/TV remains very consistent but the <Lc.V> and <Lc.St> varies. Smaller lacunar objects are difficult to mesh and more prone to measurement errors due to the comparatively large voxel size. Consequently, these small objects have a relatively coarser mesh. Both <Lc.V> and <Lc.St> are dependent on the object mesh which would explain the reduced reproducibility in comparison to Lc.N and Lc.TV. Hemmatian et al. also found lacunar measures such as <Lc.V> to be less reproducible than tissue measures such as BV/TV [48]. Consequently, <Lc.V> and <Lc.St> do not appear to be good biomarker candidates.

Previous studies have demonstrated that lacunar morphometric parameters differ between trabecular and cortical regions of bone [43, 46, 57]. We used this observation to evaluate the sensitivity of our method to biological differences by the ability to differentiate lacunae between anatomically distinct regions. This was based upon the analysis performed by Nebuloni et al. regarding the sensitivity of microCT to detect biological differences relative to vascular imaging [47]. We report significant differences between global, local, and population-based parameters including Lc.TV/BV, Lc.N/BV, <Lc.V>, <Lc.S>, [Lc.St], and [Lc.Sr] as seen in Table 3.2.4 and Figures 3.2.6A-F. Furthermore, Figures 3.2.6G-H provide a visual confirmation of the difference that we report in Figure 3.2.6A. Not only do we see that lacunar density is

lower in trabecular regions, but also the lacunae themselves look to be slightly smaller relative to the cortical regions. This would indicate that lacunae in trabecular regions also consist of lower total porosity (Lc.TV/BV), volume (<Lc.V>), and surface area (<Lc.S>). These visual differences further support our claim that the method is sensitive to previously studied regional differences and reflects the statistically significant differences that we report in Figures 3.2.6A-D. Kegelman et al. found similar lacunar morphometries in a recent study; however, overall their lacunae were slightly smaller, likely because they were of murine origin [57].

While we were able to evaluate the accuracy of lacunar identification between human and machine counting, we did not address the accuracy of the segmentation of the lacunar structures as other studies have done [48]. This is a limitation of our study and would be interesting to quantify. However, because lacunar segmentation is resolution dependent and Hemmatian et al. demonstrated that lacunar geometry is correlated, but not accurate, between desktop microCT and CLSM, we believe lacunar identification accuracy is more meaningful [48]. Additionally, the lacunar data were very sensitive to the selection of the lower volumetric bound. This was difficult to select since volumetric data from previous studies regarding the distinction between a lacuna and a micropore is limited. Furthermore, we must acknowledge the fact that partial volume effects generate error with respect to the segmented lacunar structures. Considering many lacunae have a diameter of roughly 10μm, these partial volume effects are accentuated at the 1.2μm voxel resolution. Finally, the precision study required weeks of scanning time and consequently was only performed on trabecular bone.

We present a new high-throughput method that is reproducible and sensitive to assess osteocyte lacunar morphometry in human bone samples. We use ultra-high-resolution desktop micro-CT, an individualized histogram-based segmentation procedure, and a custom evaluation algorithm to calculate global and local morphometric parameters of 7.71 million lacunae in two distinct regions of 31 human iliac crest bone samples, revealing two potential biomarkers. The validation of our method demonstrates accurate lacunar identification, reproducibility of repeated measurements, and sensitivity between anatomically distinct regions. Therefore, our new image acquisition and evaluation methodologies expand the number of investigable hypotheses surrounding osteocyte lacunae, while simultaneously employing a widely accessible and mature imaging technology – desktop micro-CT.

Acknowledgements

The authors would like to thank the Joint Scoliosis Research Center of The Chinese University of Hong Kong and Nanjing University, Hong Kong & Nanjing, China for their joint efforts on providing and processing the bone biopsies used for beam energy optimization. We thank Lucid AG for assisting with the resolution dependency study using XamFlow. We would also like to thank Peter Schwilch for assisting with biopsy machining and Dr. Patrik Christen for his mentoring.

Conflict of Interest

The authors declare no conflict of interest.

Supplementary Materials and Methods

Below are several figures which provide additional information regarding the specifics of the imaging methodology.

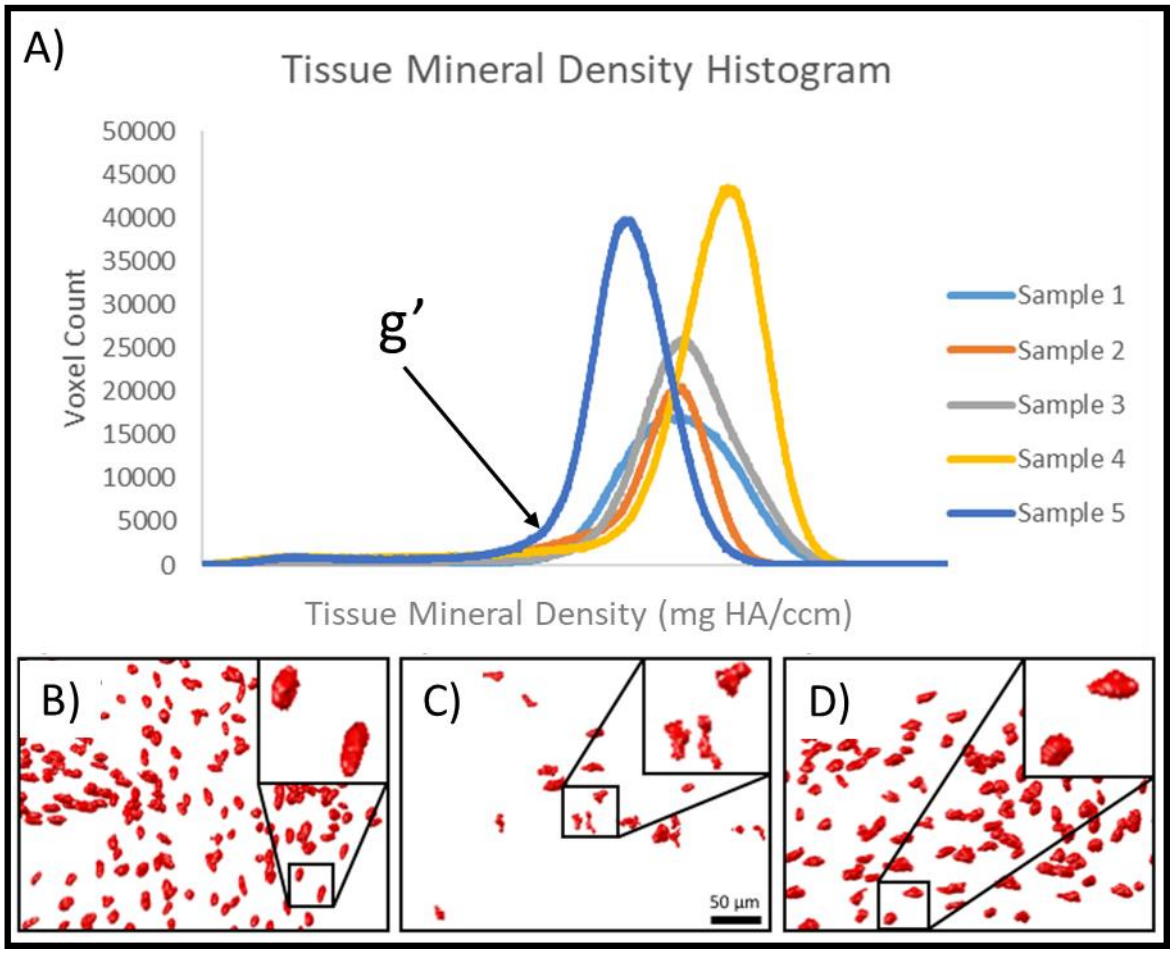

Figure 3.2.S1: A) TMD histograms for several samples where g' is the critical point. B) Segmented lacunae using a fixed threshold applied to sample 1. C) Segmented lacunae using the same fixed threshold that was applied to sample 1 to sample 2. D) Individualized threshold approach (g') calculated for sample 2 and the resulting segmented lacunae.

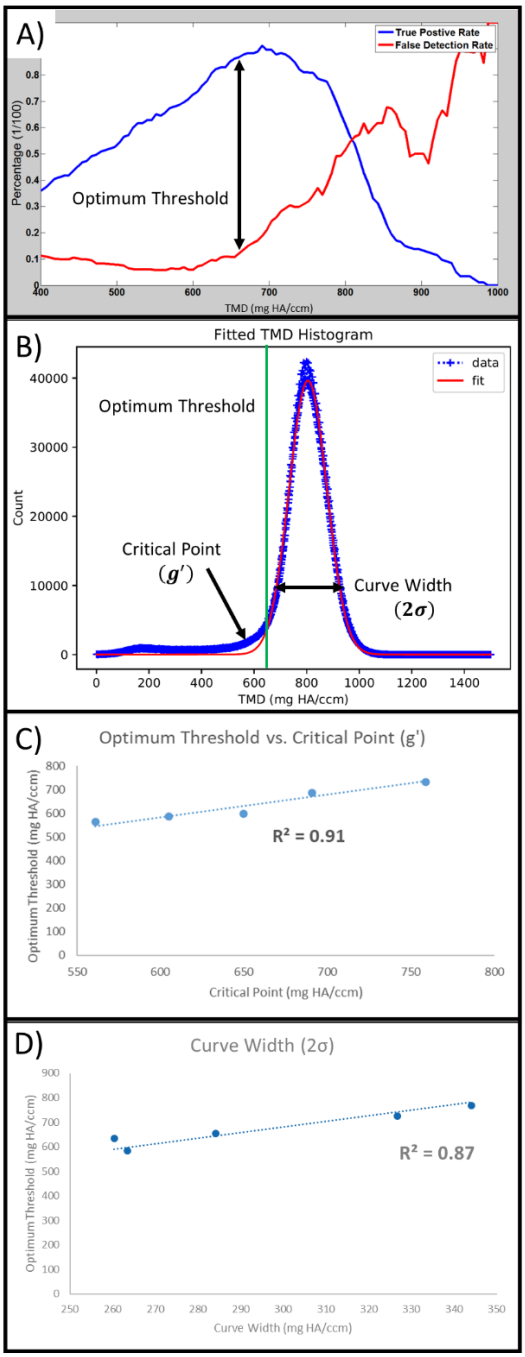

Figure 3.2.S2: Individualized threshold selection. A) Iterative application of many single thresholds and each compared with the manual identification 3D coordinates of a given image subregion. Optimum threshold was defined as the single threshold that maximized the true positive rate and minimized the false detection rate. B) Typical TMD histogram of the bone biopsy's micro-CT image. Optimum threshold (green) determined from (A) and the distribution characteristics including the critical point (g') and curve width (2sigma) were calculated from the Gaussian fit of the data. C) Correlation between the optimum threshold for each of the five manually segmented subregions and the corresponding critical point (g') from each respective TMD histogram. D) Correlation between the optimum threshold for each of the five manually segmented subregions and the corresponding distribution width (2sigma) from each respective TMD histogram.

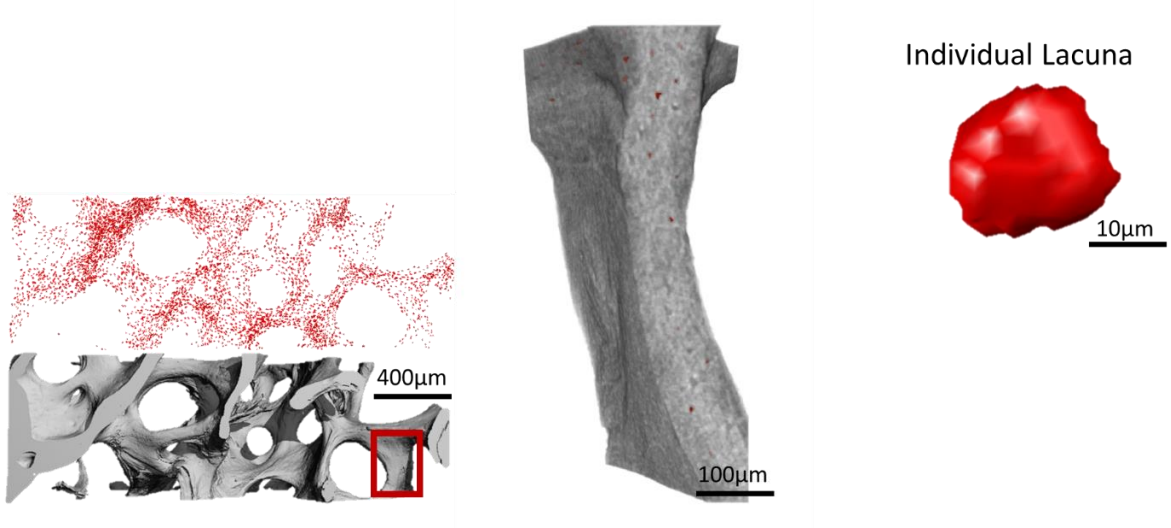

Figure 3.2.S3: Lacunar segmentation from the tissue level down to the individual cell level

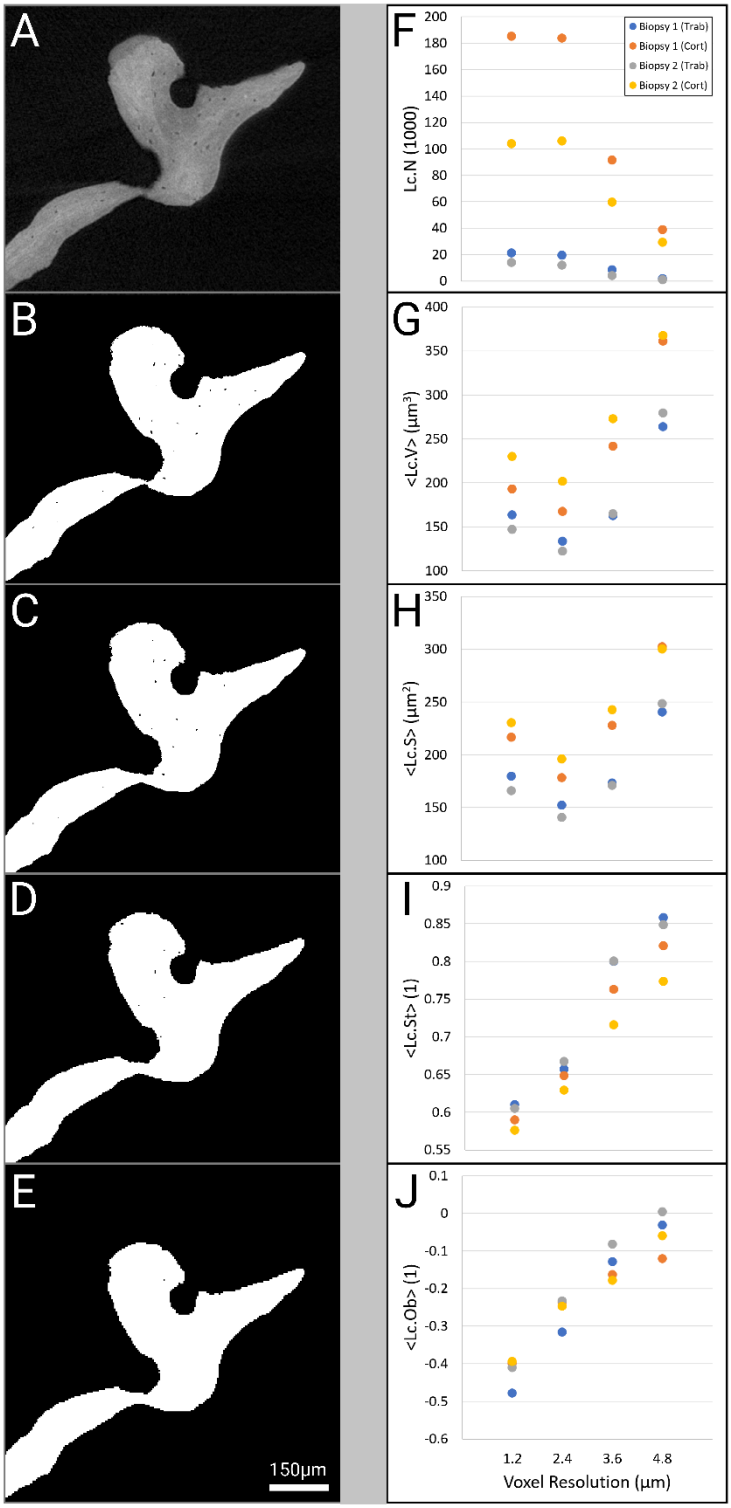

Figure 3.2.S4: Lacunar morphometry resolution dependency. A) Original microCT grayscale filtered image of trabecular bone scanned at 1.2µm resolution. B) Thresholded image at original 1.2µm resolution. C) Thresholded image at downscaled 2.4µm resolution. D) Thresholded image at downscaled 3.6µm resolution. E) Thresholded image at downscaled 4.8µm resolution. Two region-matched biopsies (four regions in total) were analyzed at all four resolutions and morphometries plotted for F) lacunar number, G) lacunar volume, H) lacunar surface area, I) lacunar stretch, and J) lacunar oblateness.

References

[1] J. Wolff, Das Gesetz der Transformation der Knochen, DMW-Deutsche Medizinische Wochenschrift 19(47) (1892) 1222-1224.

[2] W. Roux, Der Kampf der Theile im Organismus: ein Beitrag zur Vervollständigung der mechanischen Zweckmässigkeitslehre, W. Engelmann1881.

[3] L.F. Bonewald, The amazing osteocyte, J Bone Miner Res 26(2) (2011) 229-38.

[4] P.R. Buenzli, N.A. Sims, Quantifying the osteocyte network in the human skeleton, Bone 75(79) (2015) 144-50.

[5] J. Gluhak-Heinrich, L. Ye, L.F. Bonewald, J.Q. Feng, M. MacDougall, S.E. Harris, D. Pavlin, Mechanical loading stimulates dentin matrix protein 1 (DMP1) expression in osteocytes in vivo, J Bone Miner Res 18(5) (2003) 807-17.

[6] A.G. Robling, P.J. Niziolek, L.A. Baldridge, K.W. Condon, M.R. Allen, I. Alam, S.M. Mantila, J. Gluhak-Heinrich, T.M. Bellido, S.E. Harris, C.H. Turner, Mechanical stimulation of bone in vivo reduces osteocyte expression of Sost/sclerostin, J Biol Chem 283(9) (2008) 5866-75.

[7] T.M. Skerry, L. Bitensky, J. Chayen, L.E. Lanyon, Early strain-related changes in enzyme activity in osteocytes following bone loading in vivo, J Bone Miner Res 4(5) (1989) 783-8.

[8] L. Lanyon, Osteocytes, strain detection, bone modeling and remodeling, Calcified tissue international 53(1) (1993) S102-S107.

[9] F.A. Schulte, D. Ruffoni, F.M. Lambers, D. Christen, D.J. Webster, G. Kuhn, R. Muller, Local mechanical stimuli regulate bone formation and resorption in mice at the tissue level, PLoS One 8(4) (2013) e62172.

[10] R. Huiskes, R. Ruimerman, G.H. van Lenthe, J.D. Janssen, Effects of mechanical forces on maintenance and adaptation of form in trabecular bone, Nature 405(6787) (2000) 704-6.

[11] S. Hirose, M. Li, T. Kojima, P. Henrique, L. de Freitas, S. Ubaidus, K. Oda, C. Saito, N. Amizuka, A histological assessment on the distribution of the osteocytic lacunar canalicular system using silver staining, J. Bone Miner. Metab. 25(6) (2007) 374-382.

[12] C. Palumbo, A 3-dimensional ultrastructural-study of osteoid-osteocytes in the tibia of chick-embryos, Cell Tissue Res. 246(1) (1986) 125-131.

[13] G. Marotti, F. Remaggi, D. Zaffe, Quantitative investigation on osteocyte canaliculi in human compact and spongy bone, Bone 6(5) (1985) 335-337.

[14] D.J. Kubek, V.H. Gattone, M.R. Allen, Methodological Assessment of Acid-Etching for Visualizing the Osteocyte Lacunar-Canalicular Networks Using Scanning Electron Microscopy, Microsc. Res. Tech. 73(3) (2010) 182-186.

[15] C.M. Heveran, A. Rauff, K.B. King, R.D. Carpenter, V.L. Ferguson, A new open-source tool for measuring 3D osteocyte lacunar geometries from confocal laser scanning microscopy reveals age-related changes to lacunar size and shape in cortical mouse bone, Bone 110 (2018) 115-127.

[16] X.H. Lai, C. Price, S. Modla, W.R. Thompson, J. Caplan, C.B. Kirn-Safran, L.Y. Wang, The dependences of osteocyte network on bone compartment, age, and disease, Bone Res. 3 (2015) 11.

[17] F. Repp, P. Kollmannsberger, A. Roschger, M. Kerschnitzki, A. Berzlanovich, G.M. Gruber, P. Roschger, W. Wagermaier, R. Weinkamer, Spatial heterogeneity in the canalicular density of the osteocyte network in human osteons, Bone reports 6 (2017) 101-108.

[18] K.S. Mader, P. Schneider, R. Muller, M. Stampanoni, A quantitative framework for the 3D characterization of the osteocyte lacunar system, Bone 57(1) (2013) 142-54.

[19] M.G. Ascenzi, J. Gill, A. Lomovtsev, Orientation of collagen at the osteocyte lacunae in human secondary osteons, Journal of Biomechanics 41(16) (2008) 3426-3435.

[20] H.M. Britz, Y. Carter, J. Jokihaara, O.V. Leppanen, T.L.N. Jarvinen, G. Belev, D.M.L. Cooper, Prolonged unloading in growing rats reduces cortical osteocyte lacunar density and volume in the distal tibia, Bone 51(5) (2012) 913-919.

[21] Y. Carter, C.D.L. Thomas, J.G. Clement, A.G. Peele, K. Hannah, D.M.L. Cooper, Variation in osteocyte lacunar morphology and density in the human femur - a synchrotron radiation micro-CT study, Bone 52(1) (2013) 126-132.

[22] P. Schneider, M. Meier, R. Wepf, R. Muller, Towards quantitative 3D imaging of the osteocyte lacuno-canalicular network, Bone 47(5) (2010) 848-858.

[23] M. Langer, A. Pacureanu, H. Suhonen, Q. Grimal, P. Cloetens, F. Peyrin, X-Ray Phase Nanotomography Resolves the 3D Human Bone Ultrastructure, Plos One 7(8) (2012) 7.

[24] M. Kerschnitzki, W. Wagermaier, P. Roschger, J. Seto, R. Shahar, G.N. Duda, S. Mundlos, P. Fratzl, The organization of the osteocyte network mirrors the extracellular matrix orientation in bone, J Struct Biol 173(2) (2011) 303-311.

[25] L.P. Bakalova, C.M. Andreasen, J.S. Thomsen, A. Bruel, E.M. Hauge, B.J. Kiil, J.M. Delaisse, T.L. Andersen, D.M. Ph, Relating Intracortical Bone Mechanics to Pore Morphology and Remodeling Characteristics in the Human Fibula, J Bone Miner Res (2018).

[26] M.L. Bouxsein, S.K. Boyd, B.A. Christiansen, R.E. Guldberg, K.J. Jepsen, R. Muller, Guidelines for Assessment of Bone Microstructure in Rodents Using Micro-Computed Tomography, Journal of Bone and Mineral Research 25(7) (2010) 1468-1486.

[27] T. Hildebrand, A. Laib, R. Muller, J. Dequeker, P. Ruegsegger, Direct three-dimensional morphometric analysis of human cancellous bone: Microstructural data from spine, femur, iliac crest, and calcaneus, Journal of Bone and Mineral Research 14(7) (1999) 1167-1174.

[28] R. Muller, H. Van Campenhout, B. Van Damme, G. Van Der Perre, J. Dequeker, T. Hildebrand, P. Ruegsegger, Morphometric analysis of human bone biopsies: A quantitative structural comparison of histological sections and micro-computed tomography, Bone 23(1) (1998) 59-66.

[29] P. Schneider, M. Stauber, R. Voide, M. Stampanoni, L.R. Donahue, R. Muller, Ultrastructural properties in cortical bone vary greatly in two inbred strains of mice as assessed by synchrotron light based micro- and Nano-CT, Journal of Bone and Mineral Research 22(10) (2007) 1557-1570.

[30] Y. Sugawara, H. Kamioka, T. Honjo, K. Tezuka, T. Takano-Yamamoto, Three-dimensional reconstruction of chick calvarial osteocytes and their cell processes using confocal microscopy, Bone 36(5) (2005) 877-883.

[31] R.P. van Hove, P.A. Nolte, A. Vatsa, C.M. Semeins, P.L. Salmon, T.H. Smit, J. Klein-Nulend, Osteocyte morphology in human tibiae of different bone pathologies with different bone mineral density - Is there a role for mechanosensing?, Bone 45(2) (2009) 321-329.

[32] A. Vatsa, R.G. Breuls, C.M. Semeins, P.L. Salmon, T.H. Smit, J. Klein-Nulend, Osteocyte morphology in fibula and calvaria - Is there a role for mechanosensing?, Bone 43(3) (2008) 452-458.

[33] S. Suniaga, T. Rolvien, A. vom Scheidt, I.A.K. Fiedler, H.A. Bale, A. Huysseune, P.E. Witten, M. Amling, B. Busse, Increased mechanical loading through controlled swimming exercise induces bone formation and mineralization in adult zebrafish, Sci Rep 8 (2018) 13.

[34] B. Ay, K. Parolia, R.S. Liddell, Y.S. Qiu, G. Grasselli, D.M.L. Cooper, J.E. Davies, Hyperglycemia compromises Rat Cortical Bone by Increasing Osteocyte Lacunar Density and Decreasing Vascular Canal Volume, Commun. Biol. 3(1) (2020) 9.

[35] C.-C. Glüer, G. Blake, Y. Lu, B. Blunt, M. Jergas, H. Genant, Accurate assessment of precision errors: how to measure the reproducibility of bone densitometry techniques, Osteoporosis International 5(4) (1995) 262-270.

[36] A. Cohen, D.W. Dempster, R.R. Recker, E.M. Stein, J.M. Lappe, H. Zhou, A.J. Wirth, G.H. van Lenthe, T. Kohler, A. Zwahlen, R. Muller, C.J. Rosen, S. Cremers, T.L. Nickolas, D.J. McMahon, H. Rogers, R.B. Staron, J. LeMaster, E. Shane, Abnormal bone microarchitecture and evidence of osteoblast dysfunction in premenopausal women with idiopathic osteoporosis, J Clin Endocrinol Metab 96(10) (2011) 3095-105.

[37] A. Cohen, R.R. Recker, J. Lappe, D.W. Dempster, S. Cremers, D.J. McMahon, E.M. Stein, J. Fleischer, C.J. Rosen, H. Rogers, R.B. Staron, J. Lemaster, E. Shane, Premenopausal women with idiopathic low-trauma fractures and/or low bone mineral density, Osteoporos Int 23(1) (2012) 171-82.

[38] H.X. Chen, J.J. Zhang, Y.J. Wang, K.Y. Cheuk, A.L.H. Hung, T.P. Lam, Y. Qiu, J.Q. Feng, W.Y.W. Lee, J.C.Y. Cheng, Abnormal lacuno-canalicular network and negative correlation between serum osteocalcin and Cobb angle indicate abnormal osteocyte function in adolescent idiopathic scoliosis, Faseb J. 33(12) (2019) 13882-13892.

[39] M. Mashiatulla, R.D. Ross, D.R. Sumner, Validation of cortical bone mineral density distribution using micro-computed tomography, Bone 99 (2017) 53-61.

[40] M. Firbank, A. Coulthard, R. Harrison, E. Williams, A comparison of two methods for measuring the signal to noise ratio on MR images, Physics in medicine and biology 44(12) (1999) N261.

[41] B.R. McCreadie, S.J. Hollister, M.B. Schaffler, S.A. Goldstein, Osteocyte lacuna size and shape in women with and without osteoporotic fracture, Journal of Biomechanics 37(4) (2004) 563-572.

[42] F.L. Bach-Gansmo, A. Bruel, M.V. Jensen, E.N. Ebbesen, H. Birkedal, J.S. Thomsen, Osteocyte lacunar properties and cortical microstructure in human iliac crest as a function of age and sex, Bone 91 (2016) 11-19.

[43] M.P. Akhter, D. Kimmel, J. Lappe, R. Recker, Effect of Macroanatomic Bone Type and Estrogen Loss on Osteocyte Lacunar Properties in Healthy Adult Women, Calcified Tissue International (2017) 1-12.

[44] M. Stauber, R. Muller, Volumetric spatial decomposition of trabecular bone into rods and plates - A new method for local bone morphometry, Bone 38(4) (2006) 475-484.

[45] A. Carriero, M. Doube, M. Vogt, B. Busse, J. Zustin, A. Levchuk, P. Schneider, R. Muller, S.J. Shefelbine, Altered lacunar and vascular porosity in osteogenesis imperfecta mouse bone as revealed by synchrotron tomography contributes to bone fragility, Bone 61 (2014) 116-124.

[46] P. Milovanovic, B. Busse, Inter-site Variability of the Human Osteocyte Lacunar Network: Implications for Bone Quality, Curr Osteoporos Rep (2019).

[47] L. Nebuloni, G.A. Kuhn, J. Vogel, R. Muller, A Novel In Vivo Vascular Imaging Approach for Hierarchical Quantification of Vasculature Using Contrast Enhanced Micro-Computed Tomography, Plos One 9(1) (2014) 10.

[48] H. Hemmatian, M.R. Laurent, S. Ghazanfari, D. Vanderschueren, A.D. Bakker, J. Klein-Nulend, G.H. van Lenthe, Accuracy and reproducibility of mouse cortical bone microporosity as quantified by desktop microcomputed tomography, Plos One 12(8) (2017).

[49] M.L. Bouxsein, S.K. Boyd, B.A. Christiansen, R.E. Guldberg, K.J. Jepsen, R. Muller, Guidelines for assessment of bone microstructure in rodents using micro-computed tomography, J Bone Miner Res 25(7) (2010) 1468-86.

[50] E.N. Cresswell, T.M. Nguyen, M.W. Horsfield, A.J. Alepuz, T.A. Metzger, G.L. Niebur, C.J. Hernandez, Mechanically induced bone formation is not sensitive to local osteocyte density in rat vertebral cancellous bone, J Orthop Res (2017).

[51] A. Levchuk, P. Schneider, M. Meier, P. Vogel, F. Donaldson, R. Muller, An Automated Step-Wise Micro-Compression Device for 3D Dynamic Image-Guided Failure Assessment of Bone Tissue on a Microstructural Level Using Time-Lapsed Tomography, Frontiers in Materials 5 (2018) 14.

[52] S.M. Tommasini, A. Trinward, A.S. Acerbo, F. De Carlo, L.M. Miller, S. Judex, Changes in intracortical microporosities induced by pharmaceutical treatment of osteoporosis as detected by high resolution micro-CT, Bone 50(3) (2012) 596-604.

[53] B.A.a.R.M. E. Goff, A novel shape filter for lacunar imaging in human bone using ultra-high-resolution desktop micro-CT, in: M.O. P. Nithiarasu, and M. Oshima (Ed.) 6th International Conference on Computational and Mathematical Biomedical Engineering (CMBE 2019), Sendai City, Japan, 2019, pp. 651-654.

[54] J. Sijbers, A. Postnov, Reduction of ring artefacts in high resolution micro-CT reconstructions, Physics in Medicine and Biology 49(14) (2004) N247-N253.

[55] E. Tsourdi, K. Jahn, M. Rauner, B. Busse, L.F. Bonewald, Physiological and pathological osteocytic osteolysis, J. Musculoskelet. Neuronal Interact. 18(3) (2018) 292-303.

[56] T.R. Kuo, C.H. Chen, Bone biomarker for the clinical assessment of osteoporosis: recent developments and future perspectives, Biomark Res 5 (2017) 18.

[57] C.D. Kegelman, J.C. Coulombe, K.M. Jordan, D.J. Horan, L. Qin, A.G. Robling, V.L. Ferguson, T.M. Bellido, J.D. Boerckel, YAP and TAZ Mediate Osteocyte Perilacunar/Canalicular Remodeling, J Bone Miner Res 35(1) (2020) 196-210.

3.3 Towards *in silico* biomechanical evaluation of microcracking and osteocyte lacunar biomarkers

Abstract

When bone is loaded, microcracks within the tissue are typically initiated and propagated through the mineralized matrix and consequently, through the densely connected osteocyte lacunar-canalicular network (LCN). The osteocytes residing within the lacunar pores of this network are primarily thought of as the orchestrators of mechanobiological signaling processes. The LCN is also biomechanically important for bone because of its interaction with the microcracks that propagate through the tissue. Lacunar structures are relatively soft compared with the surrounding mineralized matrix, and previous experimental studies have demonstrated that lacunae guide the microcrack and partially absorb its energy. However, animal experiments requiring lab facilities and personnel are costly and time consuming – necessitating computational models.

To investigate the relationship between microcracking and the LCN, we created two micro-finite element (microFE) modeling approaches, and each model was simulated in a three-dimensional (3D) image sub-volume of human cortical bone acquired with ultra-high-resolution micro-computed tomography (microCT) to evaluate microcrack behavior relative to lacunar structures. The microcrack's path was governed by stress gradients in both models, the main difference between the models being if the canalicular connections were incorporated. We observed that when assumptions relating the canaliculi to the fluid inside the channels were included in the model, microcracking behavior more closely resembled previously published experimental results. This opens the possibility to evaluate the dynamic stress patterns surrounding the lacunar structures as an avenue towards the creation of a mechanics-centric osteocyte lacunar biomarker, or in other words, an indicator of biological changes within the bone tissue that can be derived from either global or local mechanics.

3.3.1 Introduction

Bone optimizes its structure at multiple hierarchical levels, creating an extremely high strength-to-weight ratio, with the primary material being hydroxy-apatite. Bone's interior regions consist of a special architecture. Trabecular struts create a dense web throughout the interior of the organ significantly adding to its strength. Furthermore, the interior microarchitecture undergoes continuous adaptation and optimization because it contains living cells, which sense mechanical signals (osteocytes) and regulate remodeling. These osteocytes live within individual lacunar structures that compose the densely connected and highly organized osteocyte network embedded within the matrix: the lacunar-canalicular network (LCN) [1, 2]. Since this network is softer relative to the surrounding hard mineralized tissue matrix, the LCN also minorly contributes to bone's strength as it passively absorbs some of the energy generated by propagating microcracks. Each osteocyte resides within a single lacunar pore and extends dozens of dendritic processes to connect with neighboring osteocytes, each sheathed in canalicular tubes [3, 4]. Both the osteocyte body and cell processes are separated from their lacunar-canalicular walls by interstitial fluid. Osteocytes are known to sense their mechanical environment and the flow of the fluid in the LCN has been hypothesized to be a primary mode of mechanosensation [5].

Lacunar morphologies generally resemble ellipsoids and consequently do not experience mechanical loading uniformly [6, 7]. Several studies have investigated stress concentrations at the lacunar apexes as well as at the even smaller radii of the canalicular connections [8-12]. These stress concentrations then create an amplification effect on the cell body, dendritic processes, and interstitial fluid – all of which are important to osteocyte mechanosensation [5, 13, 14]. Furthermore, the mechanics surrounding the lacunar structures may unlock the ability to use lacunae as biomarkers – a tool capable of disease recognition as has been asserted in a recent study [15].

The presence of a densely interconnected network of pores also affects the biomechanical properties of the mineralized tissue matrix and its ability to dissipate mechanical energy [16-21]. It has been demonstrated that mechanically overloading bone creates microcracks within the tissue, which subsequently propagate through the matrix and result in stress fractures [22-26]. However, many microcracks are created in the range of normal locomotion, remain small (10um – 1mm), and are integral to the bone remodeling process [27-29]. Therefore, the

investigation of the interaction between microcracking and the LCN may further support the biomechanical importance of the network and the interior osteocytes, with respect to energy dissipation and may also provide a broader insight as to how bone biomechanics is coupled with bone mechanobiology.

Voide et al. have conducted several experiments in the late 2000s that investigate time-lapsed microcracking in murine bone imaged with micro-computed tomography (microCT), and their work reflects our current understanding of the phenomenon [30, 31]. They observed microcracking to be primarily linear, parallel to the loading axis, initiating at large canals, and guided by lacunar pores. The attraction to and propagation along lacunar structures illustrate the biomechanical significance of the individual pores and, perhaps more importantly, of the collective network of pores.

However, these types of animal experiments typically consume a great deal of resources and consequently there has been a recent push towards computational micro-finite element (microFE) modeling of bone's mechanical behavior [32-34]. MicroFE models are composed of thousands to millions of elements (converted from image voxels), originating from a three-dimensional (3D) high-resolution imaging technology such as microCT [35, 36]. These models allow multiple hypotheses to be simulated on biopsies and cadaver bone samples and has led to the successful prediction of bone's behavior in the linear elastic and non-linear plastic deformation ranges [37-40]. Failure models then manipulate elemental material properties by implementing a yield criterion to act as threshold. This criterion remains a point of contention in the research community; non-linear elasticity, plasticity, and sequential damage of the mineral/collagen matrix have all been previously selected and justified [38, 40-42].

Most recently, Donaldson et al. have constructed an microFE model to simulate microcracking in microCT images of murine bone and refer to Voide's experimental work as the gold standard [43]. This is the current state-of-the-art model and employs a gradient method of steepest descent to guide a microcrack in a binarized 3D image. Several of the resulting microcracks do resemble Voide's experimental work and demonstrate a linear microcrack path that connects several lacunae when compression is simulated. Yet while the resulting microcrack is visually striking, the microcrack path is oversimplified as the input image was binarized to include only bone and void. Their model overlooks both the heterogeneous nature of the mineralized tissue matrix as well as the biomechanical importance of the underlying canalicular network.

Therefore, we created two novel microFE damage models that include the natural variation of bone mineral densities; with the ultimate goal to evaluate the importance of the LCN for microcrack development in a human biopsy based on several computer simulations.

3.3.2 Materials and Methods

MicroCT imaging of biopsy sub-volume

The cortical region of an intact human iliac crest biopsy core embedded in PMMA was imaged using a μCT50 (Scanco Medical AG, Brüttisellen, Switzerland) with a voxel resolution of 1.2μm. The 3D image was acquired using the following scanner parameters: 72 μA current, 4 W power, 55 kVp energy, 1.5 s integration time, 0.5 mm aluminum filter, level 6 data averaging, and with a total of 1500 projections. Acquired images were reconstructed with an anti-ring level 8 using the scanner software to minimize ring artifacts. A cubic sub-volume with a side dimension of 180 μm (150 voxels) was selected, which included a vascular canal and several dozen lacunae. The vascular canal and lacunae were segmented with the same threshold which was selected based on the individual distribution of bone mineral density (BMD) values as described in greater detail in the recent publication from Goff et al. [15]. All simulations were run on a standard desktop computer.

MicroFE model parameters

The image volume was meshed with a custom microFE solver, ParOSol, and the element stiffness was assigned proportional to the measured BMD values calculated using the relationship defined by Morgan et al. [44]. The yield strain was set to be 0.8% as also previously established [45]. The volume was modeled as an isotropic linear elastic material with a Poisson's ratio of 0.3. While no experimentally validated value exists currently for lacunar stiffness, we chose to set lacunae to a stiffness value of 0.05MPa based on Wang et al. who modeled the lacunar stiffness as being several orders of magnitude softer than the surrounding tissue matrix [46]. With respect to the boundary conditions, the bottom of the sub-volume was fixed and uniaxial vertical compression in the form of displacement was applied. Microcrack initiation was defined as voxels exceeding the yield strain (a maximum principal strain of 0.8%) and were defined as "critical voxels". Global compression began at 2.0% strain and the models

iterated until the microcrack ceased to grow. At this point, compression would be incremented by 0.1% strain and would continue until failure as described in the flow chart (Figure 3.3.1).

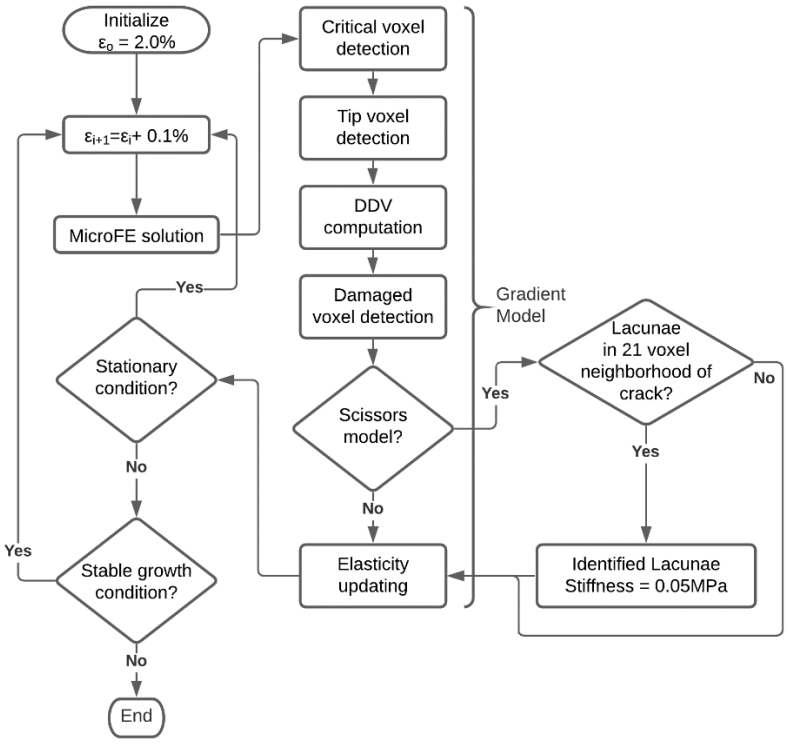

Figure 3.3.1: Detailed flow chart depicting the microcrack gradient model (MGM) and scissor model (SM).

Microcrack gradient model

The first model we created simulated microcrack propagation driven by the gradient of stresses in the sub-volume, which we named self-evidently: microcrack gradient model (MGM). "Tip voxels" in the MGM were defined as the voxels existing within the Moore neighborhood of a "critical voxel" and the "damaged voxels" from all earlier iterations. However, voxels comprising lacunar structures were excluded from the set of "tip voxels" to prevent the microcrack from initiating at the lacunar space. We also created a "sensation" region of the microcrack which originates at the "tip voxels" and is constructed by creating a 3D hemisphere on a plane normal to the "tip voxel" as depicted in Figure 3.3.2E. This concept was an extension of the microcrack propagation model from Donaldson et al., which identified a region

surrounding the microcrack tip and considered the stiffness of the included voxels [43]. Essentially, the initial hemisphere was constructed to be dependent on the global boundary conditions, and the vector normal to the plane approximates the general direction of microcrack initiation. For model simplification purposes, this hemisphere of possible directionality was modeled always to be perpendicular to the vertical axis since we assumed the microcrack direction to be primarily vertical. Voxels within the constructed hemispheric "sensing" region that exceeded 25MPa were categorized as "relevant voxels" since this stress threshold was sufficiently below the "critical voxel" failure threshold and was defined *a priori*. The hemispheric "sensing" region was chosen to be a radius of 25μm (21 voxels) and was equivalent to the distance used in the model from Donaldson et al. [43]. Once the voxels within the hemispheric sensing region have been evaluated, the deletion direction vector (DDV) which approximates the microcrack path was then guided by these "relevant voxels" throughout each iteration of the simulation. Figure 3.3.2E visually describes the process of the simulated microcrack propagation.

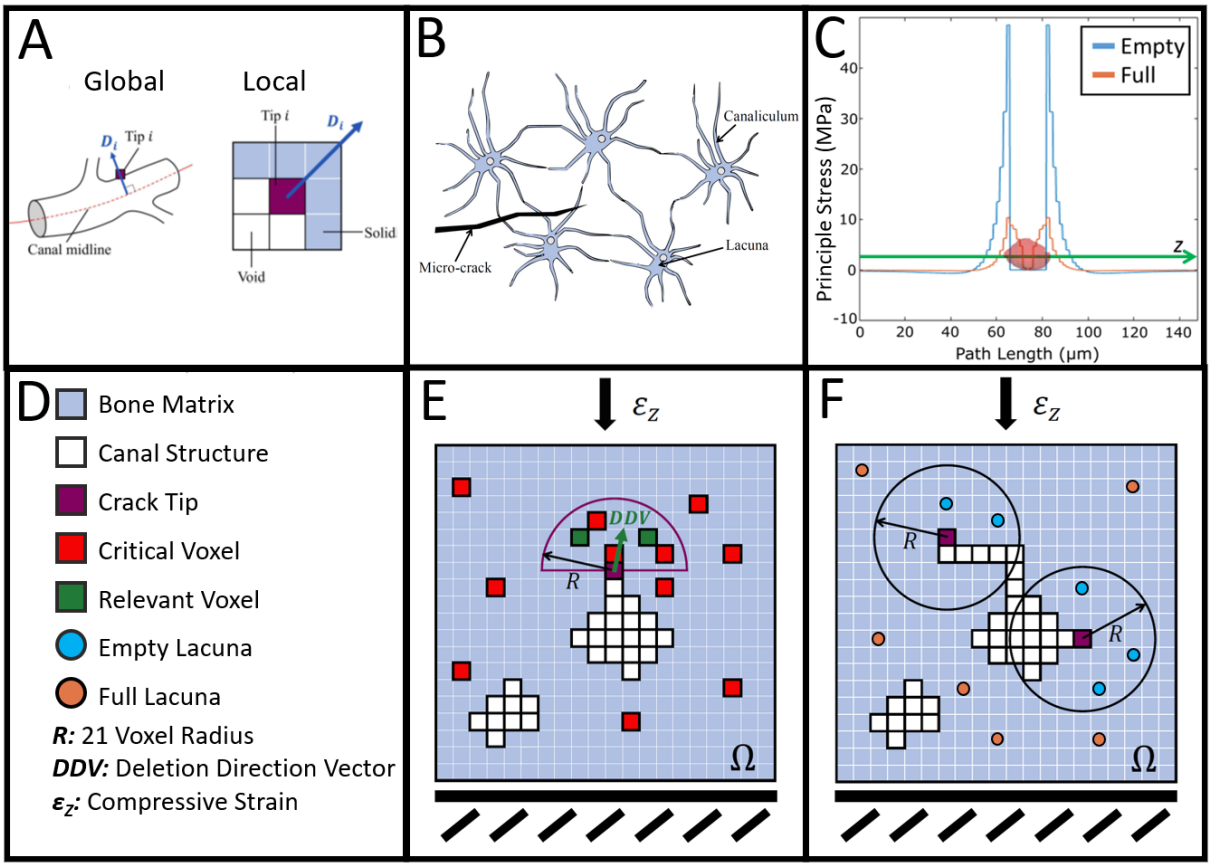

Figure 3.3.2: A) Global and local microcrack tip directions. Experimental work demonstrated that microcracks initiate at large canals (global) and propagate roughly perpendicularly to the midline in the direction of the tissue matrix at which point we consider the (local) progression and only consider the immediate neighborhood of voxels. B) Illustration of the biomechanical phenomenon of a microcrack severing lacunar canalicular processes. Adapted from Acevedo et al. 2018. C) Stress concentrations that occur in the perilacunar region for a real lacuna (red) if it contained a lacuna (full) or did not contain a lacuna (empty). D) Legend for E&F. E) 2D representation of gradient microcrack model progression through bone matrix. Microcrack tip extends from a canal along the deletion direction vector (DDV) in the path of "relevant" and "critical" voxels and evaluates voxels to be deleted. F) Depiction of how the SM computational model simulates the "scissor" phenomenon in (B). When microcrack "tip voxels" propagate within radius R of nearby lacunar pores, the lacunar fluid is emptied, the pore stiffness reduced, and the microcrack is attracted in this direction following the steepest ascent of the amplified stress gradient. The lacunae located beyond the radius R from the microcrack tip remain full and consequently do not change in stiffness.

Scissor model

The basic structure of the second microcrack model we created was very similar to the MGM. This model was created to explore the effect of the microcrack damaging and/or severing the canalicular dendritic processes and resulting stiffness reduction in the nearby lacunae – called

the scissor model (SM). Lacunar voxels in the SM were no longer restricted from the set of microcrack "tip voxels" as this requirement was naturally satisfied by the model. Furthermore, the stiffness of lacunar voxels began as being proportional to the microCT density values and only were reduced to the 0.05MPa if the microcrack tip was sufficiently near the lacuna; therefore, theoretically cutting the surrounding canaliculi, releasing the interstitial fluid, and ultimately reducing the pressure within the osteocyte pericellular matrix (PCM). While no data currently exists on the exact stiffness of the PCM, previous computational models have substituted the stiffness of chondrocyte PCM [8] which is roughly 10x stiffer than the cell body [47]. Consequently, we assumed that the fluid pressure in the PCM accounts for most of the lacunar stiffness when considering both the cell body and the PCM. Therefore, when the microcrack comes within 25μm of an osteocyte lacuna (at the edge of the hemispheric sensing region), we assumed the connecting canalicular processes to be damaged and/or severed, reducing the fluid pressure in the PCM. We then modeled this reduction in fluid pressure in the microcrack-neighborhood lacunae in the SM as a reduction in overall lacunar stiffness. This was performed by replacing the density dependent stiffness values of the voxels within the lacuna with a uniform stiffness of only the cell body, which was chosen to be the same value as in the MGM. Just as in the MGM, these low stiffness voxels that composed the nearby lacunae created stress raisers around the lacunae, which naturally drew the microcrack in the direction of the lacunar pores.

Rotations

Since only one biopsy sub-region was available for analysis, we chose the strategy of creating several rotated images from the same sub-region to compare the MGM and SM models. Each rotated region was cut from a slightly larger image volume as shown in Figure 3.3.3A to allow the microcrack propagation to be slightly different in each rotated sub-volume and to avoid the cropping problem that the corners would introduce. Furthermore, each rotated image sub-volume had slightly different canal volumes and lacunar numbers which adds to the heterogeneity of each sub-region; the differences are listed in Table 3.3.11.

3.3.3 Results

The tissue sub-volumes for both MGM and SM approaches were rotated according to the visualization in Figure 3.3.3A from 0 to 90 degrees in increments of 10 degrees and then subsequently simulated. The resulting microcrack for each was examined qualitatively and quantitatively. Figure 3.3.3B visualizes four instances of the rotated sub-volume simulated until failure in both models at 0, 20, 40, and 60 degrees. The microcrack from both MGM and SM models connected with lacunae in most cases, but in very different patterns. In the original image (0-degree rotation), the microcrack in the MGM did not visibly connect with lacunae while the microcrack in the SM diverged from the vertical z-plane to propagate through two lacunae in the y-plane. The same occurred in the 20-degree rotation, and in this instance the microcrack extended over most of the vascular canal surface in both the MGM and the SM. In the 40-degree rotation, the MGM connected through to multiple lacunae, yet the microcrack covered only a small portion of the center of the vascular canal. Conversely, the corresponding SM's microcrack had a more regular appearance as it covered most of the horizontal vascular canal while still being pulled through a single lacuna at the edge of the microcrack in the z-plane. A similar contrast between the MGM and SM was apparent in the 60-degree rotation: the SM's microcrack covered more of the vascular canal while the MGM's microcrack only covered a portion and exhibited a thin microcrack extension to an adjacent lacuna.

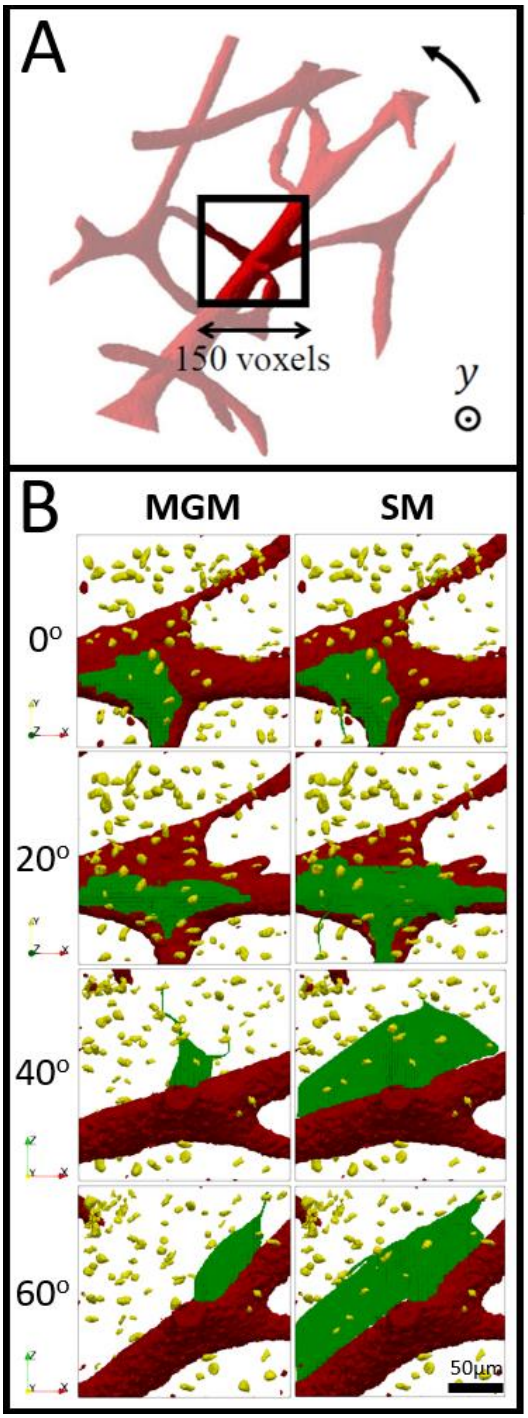

Figure 3.3.3: Microcrack model comparisons between the microcrack gradient model (MGM) and the scissor model (SM). A) Sub-regions in (B) were cut from a larger image that was first rotated around the in the y-axis counterclockwise around the origin, yielding four distinct sub-regions from approximately the same region of the sample. B) Four distinct image sub-region rotations where the microcrack (green) begins at a large canal (red) and propagates through multiple lacunae (yellow).

By rotating the sub-volume according to Figure 3.3.3A (i.e. cutting the sub-volume from a rotated larger volume), properties were slightly altered such as: canal volume per total cortical volume (Ca.V/Ct.V), total lacunar volume per total cortical volume (Lc.TV/Ct.V), lacunar number per total cortical volume (Lc.N/Ct.V). These parameters were quantified in Table 3.3.1 and varied slightly between rotations. The sub-volume rotated 40 degrees possessed the largest Lc.N/Ct.V while the 50-degree rotation included the largest Lc.TV/Ct.V and Ca.V/Ct.V. The geometries and inclusions of the 40- and 50-degree rotations were least similar to the original and final (0- and 90-degree) rotations.

Table 3.3.1: Additional extracted microdamage parameters for models including: Ca.V/Ct.V: Canal volume per total cortical volume, Lc.TV/Ct.V: total lacunar volume per total cortical volume, Lc.N/Ct.V: Lacunar number per total cortical volume.

Rotation	Ca.V/Ct.V (%)	Lc.TV/Ct.V (%)	Lc.N/Ct.V (10^3 mm^{-3})
0°	5.21	0.358	15.3
10°	5.02	0.368	15.1
20°	5.01	0.365	14.7
30°	5.11	0.359	16.3
40°	5.20	0.394	17.0
50°	5.45	0.408	16.1
60°	5.42	0.336	15.3
70°	5.29	0.348	16.3
80°	5.29	0.364	16.1
90°	5.20	0.359	15.4

The SM's ability to damage or sever canalicular processes was visualized in detail in Figure 3.3.4. Figure 3.3.4A-B display an orthographic view of the SM with and without lacunae to provide a visual connection between the three-dimensionally segmented lacunar structure and the heterogeneous stiffness gradient that each represents within the tissue sub-volume. These stiffness gradients guided the microcrack in the MGM and were also important for the SM. The difference being that the SM included a modeling of the pressure reduction that was hypothesized to occur in the perilacunar region when canaliculi were severed by the microcrack. This was visualized in Figure 3.3.4C-D where the microcrack was drawn to the lacunar structure on the left as opposed to the lacunar structure on the right. Figure 3.3.4D reveals the difference

between the image-based heterogeneous stiffness gradient present in the lacuna on the right as opposed to the lacuna on the left for which the "severed" condition had been satisfied. This resulted in a minimum stiffness (0.05MPa) being applied to all voxels of that lacuna, thus assigning it a homogeneous low stiffness value, which in turn provided a stronger attraction of the microcrack. This condition was also satisfied for the two smaller lacunae near the base of the microcrack in Figure 3.3.4D since the microcrack was sufficiently close, and consequently the canalicular processes connecting those lacunae were modeled as damaged or severed.

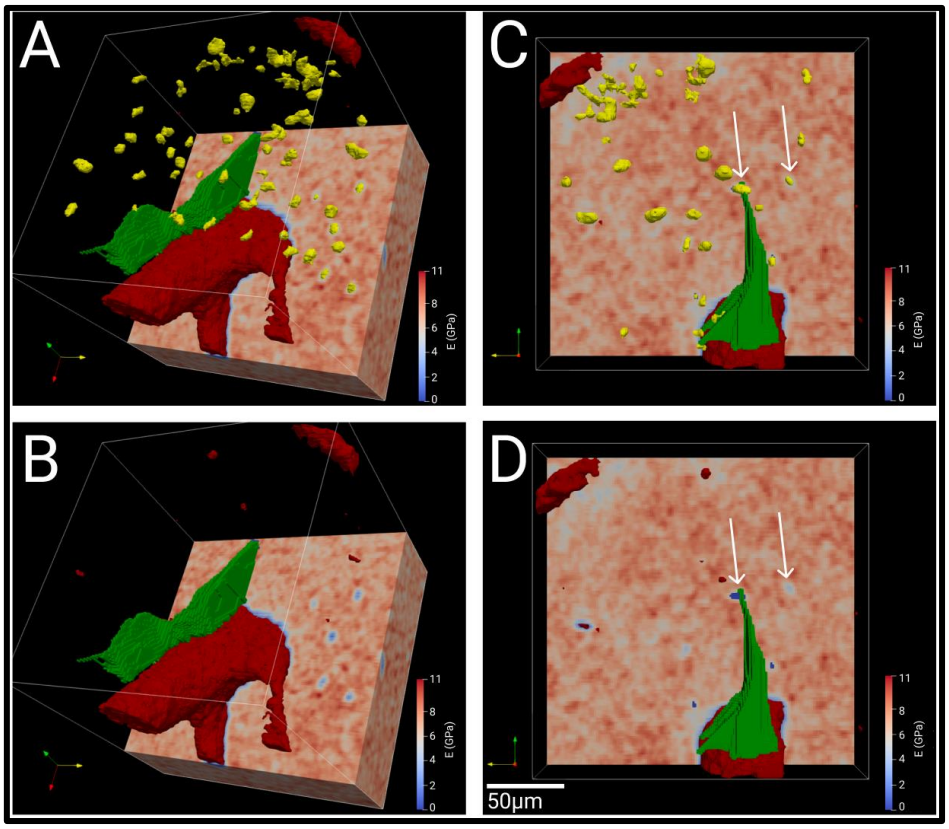

Figure 3.3.4: Three-dimensional SM of the microcrack (green) originating from vasculature (red) and propagating though the heterogeneous bone tissue and also through lacunae (yellow). A) Orthographic view of the SM with lacunae present. B) Orthographic view of the SM with 3D segmented lacunar structures removed so the remaining low stiffness (blue) portions of the lacunae are visible, revealing the stiffness reduction regions that lacunae add to the model. C) Front view of the SM with lacunae present and arrows highlighting a lacuna infiltrated by the microcrack in comparison to one that was not. D) Same as C) but with segmented lacunae removed so only the low stiffness regions that the lacunae introduce are visible. Lacuna with "severed" processes displayed as homogenous low stiffness "empty lacuna" (left), compared with lacunae without "severed" processes displayed as heterogeneous stiffness "full lacuna" derived from the image (right).

Both models were quantitatively evaluated to compare and contrast the MGM and the SM. The volume of the final microcrack in Table 3.3.2 was expressed as the total number of voxels that were deleted from the tissue sub-volume as a result of microcrack propagation. Overall, the total number of deleted voxels in the SM simulations was higher than in the MGM simulations. The iterations were held constant between the two models as a way to better compare the number of deleted voxels. The number of iterations was defined as the minimum amount required for one of the two models to reach failure. Therefore, the final applied compression was also similar except for the case of the 40-degree rotation where the SM failed at a 2.2% compression as opposed to the 2.4% MGM compression.

Table 3.3.2: Corresponding quantitative data with respect to Figure 3.3.4. Compression began at 2.0% and progressed as described in Figure 3.3.2 until failure for at least one of the models. The number of deleted voxels provide a quantification of the microcracks visualized in Figure 3.3.4.

Angle	Model type	Iterations	Final compression	Deleted voxels
0	MGM	100	2.2%	34,158
	SM	100	2.2%	35,452
20	MGM	53	2.4%	44,117
	SM	53	2.4%	75,768
40	MGM	89	2.4%	25,381
	SM	89	2.2%	58,614
60	MGM	117	2.1%	10,249
	SM	117	2.1%	40,133

Deleted voxels from the microcrack for both models were also expressed as damage to the tissue sub-volume as a percentage of the total cortical bone present in the sub-volume. Overall, the damage in the SM progressed much faster than in the MGM as seen in Figure 3.3.5. In the first 100 iterations, the SM reached peak damage rates of roughly 0.06% per iteration while the MGM never rose above 0.04% per iteration.

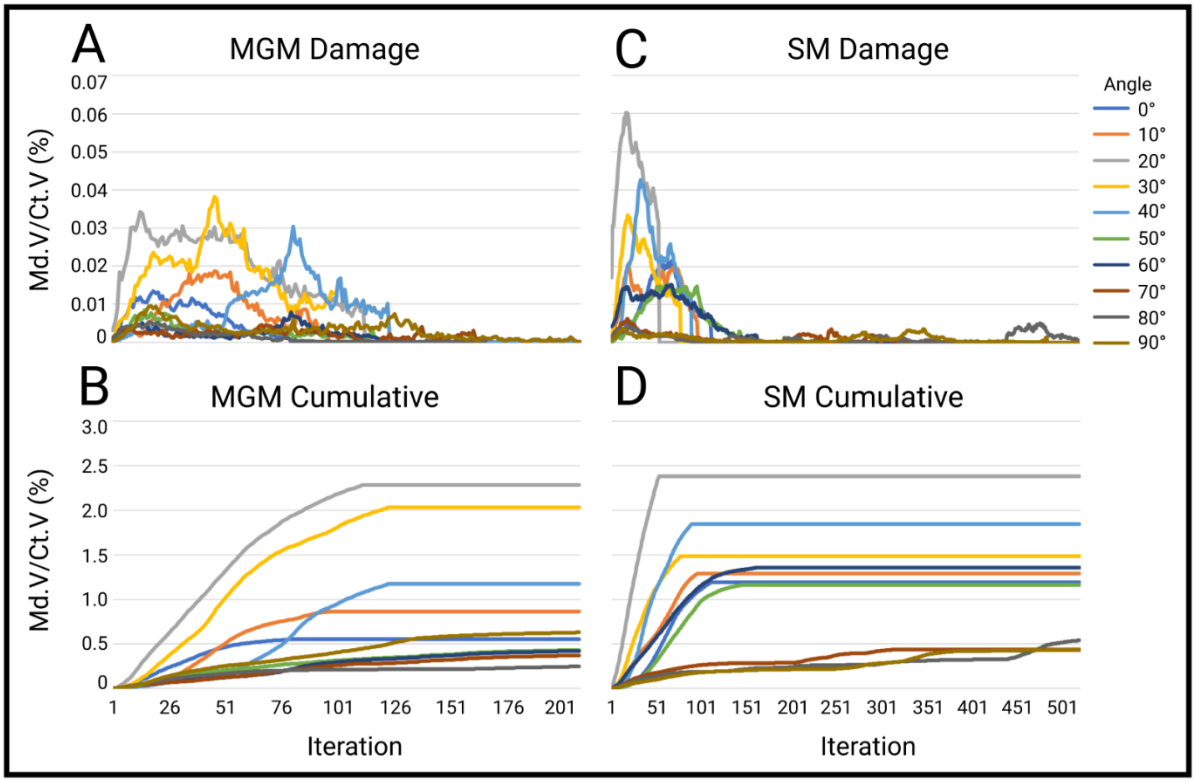

Figure 3.3.5: Quantification and comparison of the damage (Md.V/Ct.V) for both the MGM and SM for all rotations. A) MGM damage per iteration. B) MGM cumulative damage. C) SM damage per iteration. D) SM cumulative damage.

In both models, the 20-, 30-, and 40-degree rotations were damaged the most before failure while the 80- and 90-degree rotations were damaged the least before failure. All MGM simulations failed at the latest by iteration 201. Most SM simulations also failed at this point, yet three SM simulations progressed beyond 300 iterations and the 80-degree rotation continued to iteration 501 before failure. Cumulative damage was overall slightly higher for SM simulations (above 1.0% for most rotations) as compared with MGM simulations (below 1.0% for most rotations).

3.3.4 Discussion

In this study we investigated the biomechanical importance of lacunae for the densely connected LCN by simulating microcrack progression in ultra-high-resolution microCT images of human cortical bone with two distinct computational models: the microcrack gradient model (MGM) and the scissor model (SM). The MGM was based on static stress gradients that naturally emerged from the heterogeneity of density values present in the imaged bone tissue,

while the SM included a dynamic component: when the microcrack was near a lacuna, those voxels comprising the lacunar structure would be reduced to a near-zero value. Both models used a deletion direction vector (DDV) to emulate microcrack directionality as described in Figure 3.3.2E.

Lacunar structures are important for bone's resilience with respect to microcracking [11, 26, 48]. Microcracking within the bone typically follows a path of least resistance, which has been observed to be guided by lacunar structures as a means of energy absorption [31]. Because of this phenomenon, we hypothesized that the dense network of dendritic canaliculi comprising the LCN would also play a role in microcrack progression. Therefore, we constructed the SM to compare with the MGM as a means of evaluating this hypothesis. As depicted visually in Figure 3.3.2F, the SM included a conditional statement that roughly equated to the microcrack severing or damaging the canalicular dendrites. Specifically, if the microcrack entered a region of 21 voxels near a lacuna, the canaliculi (which were beyond the resolution of this study) were assumed to be damaged, the internal fluid released, and the resulting fluid pressure between the nearby osteocyte and its lacunar shell to be drastically reduced, thus creating a local stiffness minimum within the bone tissue. Ultimately, this resulted in the SM attracting the microcrack to specific lacunae at a greater rate than the MGM.

When comparing the MGM and SM visually in Figure 3.3.3B, the SM overall appeared to represent a more realistic microcrack progression than the MGM when visually comparing both models to previously conducted studies [30, 31]. Microcracks in both models originated on the vascular canal and parallel to the direction of loading; however, the microcracks in the SM at all rotations appeared to extend the entire width of the canal. This provided a strong contrast to the microcracks visualized in the MGM rotations in which they originated roughly in the center of the vascular canal and then showed "fingers" of the microcrack extending outwards to connect with lacunae. This was particularly apparent in the 40- and 60-degree rotations of the MGM. While microcrack propagation through lacunae is indeed a hallmark of experimentally observed microcracking, it did not include components of the microcrack such as these "fingers". Contrasting these odd microcracks, the SM in the 0- and 20-degree rotations exhibited microcracks that do connect with lacunae, but in a linear fashion that is distinctly different from the multiple "fingers" we observed in the MGM rotations. Furthermore, the microcrack in the MGM 0- and 20-degree rotations did not connect with the lacunae as we see

in the SM, additionally supporting the more realistic behavior of the SM. Admittedly, it was difficult to qualitatively describe these microcracks from several static perspectives.

Since the stiffness values of the image sub-volume were directly connected with the mineral density values from the image based on a previous published relationship [44], it was interesting to visualize the heterogeneity of the modeled stiffness values of the bone tissue in Figure 3.3.4. The heterogeneity was particularly important with respect to the lacunar structures and the surrounding perilacunar zones. Depending on the shape and orientation of the lacuna, the stiffness distribution varied and consequently so did the microcrack's attraction. Figure 3.3.4D clearly depicts the strength of the SM as we observed the microcrack to follow a path towards the "empty" lacuna (modeled as negligible fluid pressure) instead of the "full" lacuna (stiffness derived from the mineral density values). While our model did not possess the resolution required to visualize the canaliculi, the SM provided what we believe to be a likely estimation of the consequences of fluid release from the dendritic network.

From a quantitative perspective, we present the microcrack progression in terms of voxel deletion in Table 3.3.2 and microdamage per total cortical volume (Md.V/Ct.V) in Figure 3.3.5. In all rotations, the SM removes many more voxels (considered to be damaged) than the MGM. This was perhaps because the microcrack in the SM rotations appeared to extend the entire width of the vascular channel as visualized in Figure 3.3.3, thus damaging tissue at a far greater rate than the MGM, which appeared to be localized in the center of the canal and only extend through the tissue via small "fingers" towards the lacunae. The most damage for both models occurred in the 20-, 30-, and 40-degree rotations. One explanation for this could be that in these rotations the vascular canal was roughly perpendicular to the applied load. Therefore, the microcrack had a longer vascular canal to extend across in these rotations for both models.

The experimental work from Voide et al. remains the gold standard for microcracking within bone tissue [31]. They reported microcracking typically to be initiated at large canals, linearly progress parallel to the loading axis, and also guided by lacunar pores. We attempted to model this behavior, and both the MGM and SM similarly reproduced the findings of Voide et al. [31], and the SM possessed a slight advantage as it had fewer of the unrealistic microcrack "fingers". However, the MGM required a constraint to be set that prevented the microcrack from initiating at lacunae while the SM satisfied this requirement naturally. Furthermore, the microcracking produced by the SM visually bore a closer resemblance to the Voide et al. study.

Our microcrack modeling approach with both the MGM and SM models contained unique strengths. Prior to our investigation, the state-of-the-art modeling approach was defined by Donaldson et al. [43]. Many of our assumptions and decision criteria were based on their gradient model; however, our models went further and included the natural variation of stiffness values as defined by the heterogeneous mineral density of the bone as opposed to Donaldson's binarized images. Since both our models and the Donaldson et al. models were rooted in stress gradients, the behavior of both models was dramatically influenced by stress gradient variations. Improved by our heterogeneous distribution of image-based stiffness values, this level of detail is critical for microcrack progression and was a unique advantage of both our models and a novel contribution to the field. Furthermore, our SM continued beyond Donaldson's model by also including the importance of fluid loss in the canaliculi resulting from the microcrack damaging or severing the channels. While no experimental data exists yet to prove or disprove our fluid loss hypothesis, it provides an additional layer of detail to the model that produces realistic microcrack behavior from a qualitative perspective. Finally, our models separated the "stress limit" required for microcrack initiation and the "stress limit" required for microcrack propagation to model microcracking as is common practice in other types of fracture mechanics modeling approaches [49]. These were important criteria for the behavior of our simulated microcracks and was another important distinction between our models and previous studies.

Although our computational models allowed for novel explorations of microcrack behavior, there were several limitations that are important to acknowledge. First, both modeling approaches were simulated on a single sub-region of one biopsy. To compensate for the lack of additional regions, we rotated an expanded portion of our sub-region and isolated image volume rotations from 0 to 90 degrees of the original image. The advantage to this approach was that corner effects were avoided and the variation in simulated microcrack patterns could still be examined. However, while microcrack patterns varied widely between rotations, the basic configuration was relatively similar. This was quantified in Table 3.3.1 by examining changes such as canal volume (Ca.V/Ct.V) and lacunar density (Lc.N/Ct.V) per rotated image sub-volume, yet the variation we reported in Table 3.3.1 between rotations was small. Second, the complexity of both the MGM and SM approaches also reduced the pattern variety of simulated microcracks and generally over-constrained the models. However, simulating microcracking in 3D space within a heterogeneous material was complex and required a set of governing

principles. Some of these principles were derived from experimental findings such as the fact that microcracking does not initiate at lacunar pores, which had to be included in the MGM approach but was naturally satisfied in the SM approach. The complexity of these models also led to simulation times ranging from one week to one month. Since the initial conditions of each microcrack iteration depended on the previous iteration, parallelization of the processes was not possible. To compare the two modeling approaches, we reported microcrack damage vs. iteration in Figure 3.3.5; however, in hindsight it may have been more meaningful to investigate microcrack damage relative to apparent strain as Christen et al. had in their previous study [11]. Unfortunately, these data were not available in this study as our simulation code only output the final failure strain of each model as reported in Table 3.3.2.

Both our MGM and SM approaches approximated microcracking in bone and reproduced the general findings of Voide's experimental work [31]. The SM approach is to our knowledge the first simulation that approximated the importance of canalicular structures for microcracking within bone tissue. In this model, simulated microcracks propagated through "empty" lacunae instead of "full" lacunae and was the first step towards creating useful mechanical biomarkers from lacunar structures. It will be important to continue in this direction in future studies and investigate other potential mechanisms for the microcrack favoring specific lacunar structures as it propagates through the tissue. Perhaps the pattern of stress concentrations in the mineralized tissue surrounding lacunar structures could be condensed into a quantifiable mechanical biomarker that could be used later as an indicator for disease. Future microcrack simulations would also benefit by simplifying the model's set of governing rules. Complex simulations in other disciplines simplify by implementing cellular automata principles as a means of investigating complex behavior with a relatively simple set of rules [50]. To conclude, the two modeling approaches in our study explored the importance of lacunar structures from a biomechanical perspective in microcrack propagation. Our results suggest that the fluid release within the dense LCN as the microcrack progresses will influence the microcrack's directional path and the lacunar structures through which it ultimately propagates.

References

[1] M. Kerschnitzki, P. Kollmannsberger, M. Burghammer, G.N. Duda, R. Weinkamer, W. Wagermaier, P. Fratzl, Architecture of the osteocyte network correlates with bone material quality, Journal of Bone and Mineral Research 28(8) (2013) 1837-1845.

[2] M. Kerschnitzki, W. Wagermaier, P. Roschger, J. Seto, R. Shahar, G.N. Duda, S. Mundlos, P. Fratzl, The organization of the osteocyte network mirrors the extracellular matrix orientation in bone, J Struct Biol 173(2) (2011) 303-311.

[3] G.Y. Rochefort, S. Pallu, C.L. Benhamou, Osteocyte: the unrecognized side of bone tissue, Osteoporosis International 21(9) (2010) 1457-1469.

[4] D.M. Cooper, A.L. Turinsky, C.W. Sensen, B. Hallgrímsson, Quantitative 3D analysis of the canal network in cortical bone by micro-computed tomography, The Anatomical Record Part B: The New Anatomist: An Official Publication of the American Association of Anatomists 274(1) (2003) 169-179.

[5] L.F. Bonewald, The amazing osteocyte, J Bone Miner Res 26(2) (2011) 229-38.

[6] R.F. van Oers, H. Wang, R.G. Bacabac, Osteocyte shape and mechanical loading, Curr Osteoporos Rep 13(2) (2015) 61-6.

[7] V. Wu, R.F.M. van Oers, E. Schulten, M.N. Helder, R.G. Bacabac, J. Klein-Nulend, Osteocyte morphology and orientation in relation to strain in the jaw bone, Int J Oral Sci 10(1) (2018) 2.

[8] S.W. Verbruggen, T.J. Vaughan, L.M. McNamara, Strain amplification in bone mechanobiology: a computational investigation of the in vivo mechanics of osteocytes, Journal of the Royal Society Interface 9(75) (2012) 2735-2744.

[9] D.P. Nicolella, D.E. Moravits, A.M. Gale, L.F. Bonewald, J. Lankford, Osteocyte lacunae tissue strain in cortical bone, J Biomech 39(9) (2006) 1735-43.

[10] A.R. Stern, D.P. Nicolella, Measurement and estimation of osteocyte mechanical strain, Bone 54(2) (2013) 191-5.

[11] D. Christen, A. Levchuk, S. Schori, P. Schneider, S.K. Boyd, R. Muller, Deformable image registration and 3D strain mapping for the quantitative assessment of cortical bone microdamage, J. Mech. Behav. Biomed. Mater. 8 (2012) 184-193.

[12] A.R. Bonivtch, L.F. Bonewald, D.P. Nicolella, Tissue strain amplification at the osteocyte lacuna: a microstructural finite element analysis, Journal of biomechanics 40(10) (2007) 2199-2206.

[13] Y.L. Wang, L.M. McNamara, M.B. Schaffler, S. Weinbaum, A model for the role of integrins in flow induced mechanotransduction in osteocytes, P Natl Acad Sci USA 104(40) (2007) 15941-15946.

[14] F.A. Schulte, A. Zwahlen, F.M. Lambers, G. Kuhn, D. Ruffoni, D. Betts, D.J. Webster, R. Muller, Strain-adaptive in silico modeling of bone adaptation--a computer simulation validated by in vivo micro-computed tomography data, Bone 52(1) (2013) 485-92.

[15] Elliott Goff, Federica Buccino, Chiara Bregoli, Jonathan P. McKinley, Basil Aeppli, Robert R. Recker, Elizabeth Shane, Adi Cohen, Gisela Kuhn, Ralph Müller, Large-scale quantification of human osteocyte lacunar morphological biomarkers as assessed by ultra-high-resolution desktop micro-computed tomography, Bone 152 (2021) 116094.

[16] R.W. McCalden, J.A. McGeough, M.B. Barker, Age-related changes in the tensile properties of cortical bone. The relative importance of changes in porosity, mineralization, and microstructure, The Journal of bone and joint surgery. American volume 75(8) (1993) 1193-1205.

[17] Y.N. Yeni, C.U. Brown, Z. Wang, T.L. Norman, The influence of bone morphology on fracture toughness of the human femur and tibia, Bone 21(5) (1997) 453-459.

[18] K.L. Bell, N. Loveridge, J. Power, N. Garrahan, B.F. Meggitt, J. Reeve, Regional differences in cortical porosity in the fractured femoral neck, Bone 24(1) (1999) 57-64.

[19] G. Jordan, N. Loveridge, K. Bell, J. Power, N. Rushton, J. Reeve, Spatial clustering of remodeling osteons in the femoral neck cortex: a cause of weakness in hip fracture?, Bone 26(3) (2000) 305-313.

[20] P. Schneider, M. Stauber, R. Voide, M. Stampanoni, L.R. Donahue, R. Muller, Ultrastructural properties in cortical bone vary greatly in two inbred strains of mice as assessed

by synchrotron light based micro- and Nano-CT, Journal of Bone and Mineral Research 22(10) (2007) 1557-1570.

[21] P. Schneider, R. Voide, M. Stampanoni, L.R. Donahue, R. Muller, The importance of the intracortical canal network for murine bone mechanics, Bone 53(1) (2013) 120-8.

[22] B.R. Beck, Tibial stress injuries - An aetiological review for the purposes of guiding management, Sports Med. 26(4) (1998) 265-279.

[23] D.B. Burr, Bone, Exercise, and Stress Fractures, Exercise and Sport Sciences Reviews 25(1) (1997) 171-194.

[24] S.W. Donahue, N.A. Sharkey, K.A. Modanlou, L.N. Sequeira, R.B. Martin, Bone strain and microcracks at stress fracture sites in human metatarsals, Bone 27(6) (2000) 827-833.

[25] J.G. Peloso, J.P. Watkins, S.R. Keele, E.L. Morris, Bilateral stress-fractures of the tibia in a racing american quarter horse, J. Am. Vet. Med. Assoc. 203(6) (1993) 801-803.

[26] D. Taylor, J.G. Hazenberg, T.C. Lee, Living with cracks: Damage and repair in human bone, Nat. Mater. 6(4) (2007) 263-268.

[27] N.L. Fazzalari, M.R. Forwood, K. Smith, B.A. Manthey, P. Herreen, Assessment of cancellous bone quality in severe osteoarthrosis: Bone mineral density, mechanics, and microdamage, Bone 22(4) (1998) 381-388.

[28] T.C. Lee, S. Mohsin, D. Taylor, R. Parkesh, T. Gunnlaugsson, F.J. O'Brien, M. Giehl, W. Gowin, Detecting microdamage in bone, Journal of Anatomy 203(2) (2003) 161-172.

[29] F.J. O'Brien, D. Taylor, G.R. Dickson, T.C. Lee, Visualisation of three-dimensional microcracks in compact bone, Journal of Anatomy 197 (2000) 413-420.

[30] R. Voide, P. Schneider, M. Stauber, G.H. van Lenthe, M. Stampanoni, R. Muller, The importance of murine cortical bone microstructure for microcrack initiation and propagation, Bone 49(6) (2011) 1186-93.

[31] R. Voide, P. Schneider, M. Stauber, R. Wyss, M. Stampanoni, U. Sennhauser, G.H. van Lenthe, R. Muller, Time-lapsed assessment of microcrack initiation and propagation in murine cortical bone at submicrometer resolution, Bone 45(2) (2009) 164-173.

[32] D. Ruffoni, G. Van Lenthe, 3.10 Finite element analysis in bone research: a computational method relating structure to mechanical function, Compr. Biomater. II 3 (2017) 169-196.

[33] P. Christen, K. Ito, R. Ellouz, S. Boutroy, E. Sornay-Rendu, R.D. Chapurlat, B. van Rietbergen, Bone remodelling in humans is load-driven but not lazy, Nat Commun 5 (2014) 4855.

[34] P. Christen, K. Ito, A.A. Santos, R. Muller, R. Bert van, Validation of a bone loading estimation algorithm for patient-specific bone remodelling simulations, J Biomech 46(5) (2013) 941-8.

[35] B. van Rietbergen, H. Weinans, R. Huiskes, A. Odgaard, A New Method To Determine Trabecular Bone Elastic Properties And Loading Using Micromechanical Finite-Element Models, Journal of Biomechanics 28(1) (1995) 69-+.

[36] R. Muller, P. Ruegsegger, Three-Dimensional Finite-Element Modeling Of Noninvasively Assessed Trabecular Bone Structures, Med. Eng. Phys. 17(2) (1995) 126-133.

[37] T.M. Keaveny, E.F. Morgan, G.L. Niebur, O.C. Yeh, Biomechanics of trabecular bone, Annu. Rev. Biomed. Eng. 3 (2001) 307-333.

[38] G.L. Niebur, M.J. Feldstein, J.C. Yuen, T.J. Chen, T.M. Keaveny, High-resolution finite element models with tissue strength asymmetry accurately predict failure of trabecular bone, Journal of Biomechanics 33(12) (2000) 1575-1583.

[39] E. Verhulp, B. Van Rietbergen, R. Muller, R. Huiskes, Micro-finite element simulation of trabecular-bone post-yield behaviour - effects of material model, element size and type, Comput. Methods Biomech. Biomed. Eng. 11(4) (2008) 389-395.

[40] E. Verhulp, B. van Rietbergen, R. Muller, R. Huiskes, Indirect determination of trabecular bone effective tissue failure properties using micro-finite element simulations, Journal of Biomechanics 41(7) (2008) 1479-1485.

[41] P. Pankaj, F.E. Donaldson, Algorithms for a strain-based plasticity criterion for bone, Int. J. Numer. Meth. Biomed. 29(1) (2013) 40-61.

[42] M.R. Hardisty, R. Zauel, S.M. Stover, D.P. Fyhrie, The Importance of Intrinsic Damage Properties to Bone Fragility: A Finite Element Study, J Biomech Eng-T Asme 135(1) (2013) 9.

[43] F. Donaldson, D. Ruffoni, P. Schneider, A. Levchuk, A. Zwahlen, P. Pankaj, R. Muller, Modeling microdamage behavior of cortical bone, Biomech Model Mechanobiol 13(6) (2014) 1227-42.

[44] E.F. Morgan, H.H. Bayraktar, T.M. Keaveny, Trabecular bone modulus-density relationships depend on anatomic site, Journal of Biomechanics 36(7) (2003) 897-904.

[45] E.F. Morgan, T.M. Keaveny, Dependence of yield strain of human trabecular bone on anatomic site, Journal of biomechanics 34(5) (2001) 569-577.

[46] L. Wang, J. Dong, C.J. Xian, Strain amplification analysis of an osteocyte under static and cyclic loading: a finite element study, BioMed Research International 2015 (2015).

[47] L.G. Alexopoulos, L.A. Setton, F. Guilak, The biomechanical role of the chondrocyte pericellular matrix in articular cartilage, Acta Biomater 1(3) (2005) 317-25.

[48] J. O'Brien F, D.A. Hardiman, J.G. Hazenberg, M.V. Mercy, S. Mohsin, D. Taylor, T.C. Lee, The behaviour of microcracks in compact bone, Eur J Morphol 42(1-2) (2005) 71-9.

[49] D. Hahn, C. Wojtan, High-resolution brittle fracture simulation with boundary elements, ACM Transactions on Graphics (TOG) 34(4) (2015) 1-12.

[50] S. Wolfram, Cellular automata as models of complexity, Nature 311(5985) (1984) 419-424.

Chapter 4

Osteocyte lacunar biomarkers for the characterization of human rare bone diseases

4.1 Large-scale osteocyte lacunar morphological analysis of transiliac bone in normal and osteoporotic premenopausal women

Elliott Goff[1], Adi Cohen[2], Elizabeth Shane[2], Robert R. Recker[3], Gisela Kuhn[1], Ralph Müller[1]

[1] Institute for Biomechanics, ETH Zurich, Zurich, Switzerland

[2] Department of Medicine, Columbia University Vagelos College of Physicians & Surgeons, New York, NY, USA

[3] Department of Medicine, Creighton University Medical Center, Omaha, NE, USA

Preprint version on MedRXiv:

https://doi.org/10.1101/2021.12.13.21267731

Abstract

Bone's adaptation ability is governed by the network of embedded osteocytes that inhabit individual crevasses called lacunae. The morphology of these lacunae and their resident osteocytes are known to change with age and diseases such as postmenopausal osteoporosis. However, it is unclear whether alterations in lacunar morphology are present in younger populations with osteoporosis. To investigate this, we implemented a previously validated methodology to image and quantify the three-dimensional morphometries of lacunae on a large scale (26.2 million cells) with ultra-high-resolution micro-computed tomography (microCT) in transiliac bone biopsies from three groups of premenopausal women: control n=39; idiopathic osteoporosis (IOP) n=45; idiopathic low BMD (ILBMD) n=19. Important lacunar morphometric parameters were measured in both trabecular and cortical bone: lacunar density (Lc.N/BV), lacunar porosity (Lc.TV/BV), lacunar number (Lc.N), lacunar volume (Lc.V), lacunar surface area (Lc.S), lacunar alignment (Lc.θ), lacunar stretch (Lc.St), lacunar oblateness (Lc.Ob), lacunar equancy (Lc.Eq), and lacunar sphericity (Lc.Sr). These were then compared against each other and also with previously measured tissue morphometries including: bone volume density (BV/TV), trabecular separation (Tb.Sp), trabecular number (Tb.N), and trabecular thickness (Tb.Th), structure model index (SMI), cortical porosity (Ct.Po) and cortical pore spacing (Ct.Sp). We detected no differences in lacunar morphology between the IOP, ILBMD and healthy premenopausal women. In contrast, we did find significant differences between lacunar morphologies in cortical and trabecular regions within all three groups, which was consistent with our previous findings on a subgroup of the healthy group. Furthermore, we discovered strong correlations between Lc.Sr from both trabecular and cortical regions with the measured BV/TV. The findings and comprehensive lacunar dataset we present here will be a crucial foundation for future investigations of the relationship between osteocyte lacunar morphology and disease.

Keywords: micro-CT, lacuna, morphometry, osteoporosis, human, osteocyte

4.1.1 Introduction

Osteocytes are the cells within bone tissue that orchestrate bone remodeling via signaling to surface cells [1-5]. They are suspended in fluid and are ensconced within small pores in the mineralized bone matrix, called lacunae. When the bone matrix is compressed by mechanical loading (such as exercise), this results in micro-deformations and fluid-flow shear stress on the osteocyte cell body. The cells then transduce these mechanical signals into chemical ones such as nitric oxide (NO), prostaglandin E2 (PGE2), and bone morphogenic proteins (BMPs) [6, 7]. Consequently, the morphology and distribution of osteocytes and their lacunae is extremely important for the transmitted signal, and the strain concentrations between lacunar structures and extending canaliculi have been shown to drastically amplify the compression experienced at the tissue scale to the cell scale [8, 9]. Therefore, small changes to the lacunar morphology, number of lacunae, and density of the lacunar network could potentially alter the osteocyte's ability to transduce mechanical signals. Previous studies have demonstrated lacunar morphology differences in patients with low bone mineral density (BMD), such as increased volume and surface area, [10] while others have also shown lower lacunar density in osteoporotic patients relative to control groups [11, 12]. Aging has also been associated with decreased lacunar density, which may contribute to reduced bone remodeling in elderly populations [11, 13-17].

In this study, we investigated the lacunar morphology in iliac crest biopsy samples from premenopausal women with idiopathic osteoporosis (IOP) diagnosed based on history of adult low trauma fracture(s), or idiopathic low bone mineral density (ILBMD) without a history of adult low-trauma fracture, as well as premenopausal healthy non-osteoporotic controls, previously recruited for studies of premenopausal osteoporosis [18-20]. Although most premenopausal women with osteoporosis have a known condition or medication exposure that has caused bone fragility, the affected women recruited for these studies had normal gonadal function and no known disease or medication exposure associated with bone loss. Thus, their rare condition was considered idiopathic. [21].

Previous studies, including biochemistries, histological parameters, and the three-dimensional microarchitecture of transiliac biopsies, in these affected women with idiopathic osteoporosis based on low trauma fracture history (IOP) or very low BMD (ILBMD) have documented thinner, fewer, and more separated trabecular struts relative to the control cohort, as well as

thinner cortices [18-20]. Bone remodeling, assessed both by serum bone turnover markers and at the tissue level by transiliac bone biopsy, was quite variable, suggesting that the mechanism of osteoporosis in the affected women may be heterogeneous.

Lacunar morphometric parameters are ideal to investigate as these structures remain intact long after the biopsy has been extracted and the osteocytes have died. Based on these studies, and previous studies reporting differences in lacunae between older osteoporotic subjects and control groups, we hypothesized that differences between control, IOP, and ILBMD groups would also manifest within the 3D morphology of osteocyte lacunae. Additionally, we hypothesized that lacunar morphology would differ between cortical and trabecular regions, as has been previously described [22], as well as correlate with global morphometric parameters such as BV/TV. To test our hypotheses, we imaged and analyzed the same biopsies as the previous studies [18-20], using a validated ultra-high resolution micro-computed tomography (microCT) imaging method to evaluate lacunar morphology in both trabecular and cortical regions [22].

4.1.2 Materials and Methods

Patient population

Premenopausal women aged 18 – 48 years were recruited at Columbia University Irving Medical Center (New York, NY) and Creighton University (Omaha, NE) with previously reported inclusion and exclusion criteria as described in detail by Cohen et al. [18-20]. To summarize, 104 women were included in this study and composed three groups: healthy control n=40, IOP n=45, and ILBMD n=19. The IOP group included women who had sustained ≥1 low trauma adult fractures irrespective of their areal bone mineral density (aBMD). The ILBMD group included women with low aBMD as determined by dual-energy x-ray absorptiometry (DXA; T score ≤2.5 or Z score ≤ 2.0) who had no history of low trauma adult fractures. Healthy premenopausal women with no adult low trauma fractures and T score /Z score ≥ -1.0 comprised the control group. Secondary causes of osteoporosis were excluded by history and biochemical/hormonal evaluations in all affected subjects and controls. All subjects provided written informed consent and the institutional review boards of both institutions approved these studies.

MicroCT tissue analysis

Following surgical extraction, fresh biopsies were imaged with a microCT40 (Scanco Medical AG, Brüttisellen, Switzerland) at a nominal resolution of 8μm as previously detailed [18, 23, 24]. An earlier described direct 3D method was implemented to calculate the following trabecular parameters [25]: bone volume density (BV/TV), trabecular separation (Tb.Sp), trabecular number (Tb.N), and trabecular thickness (Tb.Th). Furthermore, the structure model index (SMI) was calculated according to Hildebrand et al. and quantifies the ratio of rod to plate structures within the 3D bone microarchitecture [26]. Cortical indices calculated were cortical porosity (Ct.Po) and cortical pore spacing (Ct.Sp) according to [27].

MicroCT lacunar analysis

Lacunar imaging and analysis were performed on a microCT50 (Scanco Medical AG, Brüttisellen, Switzerland) at a nominal resolution of 1.2μm as previously described by Goff et al. [22]. Briefly, biopsies were embedded in polymethylmethacrylate (PMMA), cut, and lathed into cylindrical subregions (3.8mm x 10mm) which included both cortical and trabecular regions of each biopsy. Cortical and trabecular 3D image stacks were acquired from each biopsy using optimized scanning parameters: 72 μA current, 4 W power, 55 kVp energy, 1.5 s integration time, level 6 data averaging, and 1500 x-ray projections [22]. Lacunae were segmented via image inversion after applying an individualized threshold based on the distribution of tissue mineral density (TMD) values of each sample. Morphometric parameters of segmented lacunae were calculated with a custom Python script (3.7.1, Python Software Foundation, Delaware, USA) used in combination with XamFlow (Lucid AG, Zürich, Switzerland) and included: Lacunar density (Lc.N/BV), lacunar porosity (Lc.TV/BV), lacunar number (Lc.N), lacunar volume (Lc.V), lacunar surface area (Lc.S), lacunar alignment (Lc.θ), lacunar stretch (Lc.St) and lacunar oblateness (Lc.Ob) as first defined by Mader et al. [28], lacunar equancy (Lc.Eq) as described by Carter et al. [29, 30], and lacunar sphericity (Lc.Sr) as defined by Akhter et al. [31]. Following the nomenclature from Stauber et al. [32], local lacunar parameters normalized to the number of lacunae were denoted as angle brackets (<>) while population lacunar parameters including the entire range of lacunae we labeled with square brackets ([]). The analysis pipeline was previously validated through measures of accuracy, reproducibility, and sensitivity [22]. One biopsy from the control group was excluded because not enough bone was present to scan at high resolution (resulting in n=39).

Statistical analysis

Student's t-tests including the required Bonferroni correction factor ($p<0.0083$) were performed using SPSS (IBM Corp., Version 24.0., Armonk, NY) with respect to the regional inter-group comparison presented in Figure 4.1.2. Pearson correlations were performed on the data presented in Figure 4.1.3 and significance of correlations were reported in Table 4.1.2. Pearson correlations including a linear and quadratic terms were performed on the data in Figure 4.1.4.

4.1.3 Results

Lacunar morphology

Local and population-based lacunar morphometric indices were measured and compared as presented in Figure 4.1.1. Scatter plots contain 103 data points, each representing a local (normalized) lacunar morphometric parameter for an individual patient, while the histograms contain the population-based lacunar morphometric parameters with all 22.6 million lacunae included. Important lacunar morphometric parameters included size dependent measures like volume and surface area (Lc.V and Lc.S) and also slightly more abstract shape tensors like stretch, oblateness, equancy, and sphericity (Lc.St, Lc.Ob, Lc.Eq, and Lc.Sr). Lacunar population distributions appeared to be slightly different between the groups for Lc.TV/BV and Lc.N/BV morphometric parameters, but differences were not significant. Correlations emerged in the scatter plots between parameters such as <Lc.S> and <Lc.V> as well as <Lc.St> and <Lc.Eq>. However, the calculations of these two sets of parameters were inter-related so the correlation was expected. Overall, the lacunar morphometric parameters from the control, IOP, and ILBMD groups were inseparable in the scatter plots in Figure 4.1.1. Furthermore, the distribution histograms of the entire lacunar population were indistinguishable among the three groups. This was true for both cortical and trabecular regions. Similar results persisted when IOP and ILBMD groups were combined into a single affected group to compare with controls.

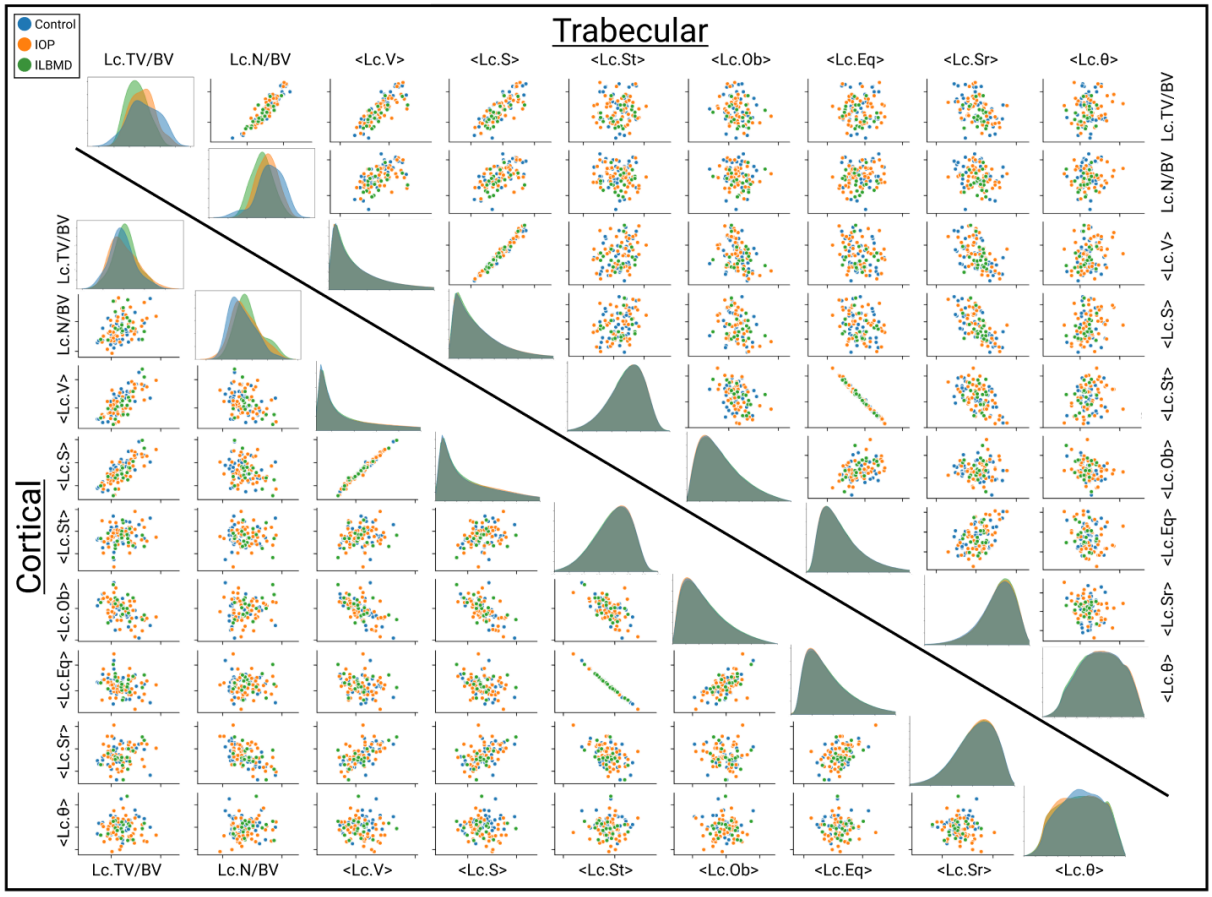

Figure 4.1.1: Overview of all measured lacunar morphometric parameters relative to each other. Morphometric parameter distributions and clustering for trabecular regions (top) and cortical regions (bottom). Each plotted point is the mean value of all lacunae from an individual biopsy region (Control, n=39; IOP, n=45; ILBMD, n=19). Histograms display the distribution of the entire lacuna population (n= 22,620,716) from each of the analyzed groups from both regions (Cortical: Control, n=8,371,890; IOP, n=7,206,171; ILBMD, n=3,385,960. Trabecular: Control, n=1,546,019; IOP, n= 1,601,880; ILBMD, n=508,796).

While the three groups were inseparable within the respective trabecular and cortical regions, clear differences emerged between the two regions for each of the three groups for key local lacunar indices such as Lc.N/BV, <Lc.V>, and <Lc.Sr>. Figure 4.1.2A-C illustrates significant differences ($p<0.001$) between cortical and trabecular regions for the control, IOP, and ILBMD groups. Lacunae in cortical regions were significantly larger (<Lc.V>) and more numerous per bone volume (Lc.N/BV) than in trabecular bone. Yet, the lacunae in trabecular bone were significantly more spherical (<Lc.Sr>) than those in the cortical regions. These three differences were consistent for all three groups. The quantitative findings in Figure 4.1.2A-C were then qualitatively corroborated by the 3D visualizations presented in Figure 4.1.2D-I in which the

individual lacunae from the median samples in Figure 4.1.2C were colored according to their sphericity. The trabecular lacunae in Figure 4.1.2G-I appear overall rounder, sparser, and smaller than in their cortical counterpart displayed in Figure 4.1.2D-F. Furthermore, the lacunae visualized in both trabecular and cortical regions appear to be aligned in semi-regular orientations, particularly the less spherical lacunae. Distributions of the ILBMD group appear narrower in Figure 4.1.2A-C; however, this may be an artifact present from the recruitment protocol for the group. By definition, ILBMD patients were patients with low bone mass (DXA; T score $\leq$2.5 or Z score $\leq$ 2.0) and interestingly a narrower distribution of bone tissue and lacunar morphometric parameters were present in the population as is shown here in Figure 4.1.22A-C and further described in Figure 4.1.3 and Figure 4.1.4. Subject characteristics were overall similar between the affected groups as presented in Table 4.1.1.

Table 4.1.1: Subject characteristics of each group. [a] $p<0.05$ vs. controls, [b] $p<0.01$ vs. controls, [c] $p<0.001$ vs. controls, [d] $p<0.01$ IOP vs. ILBMD.

Parameter	**Control (n=39)**	**IOP (n=45)**	**ILBMD (n=19)**
Anthropometric characteristics			
Age (yr)	37.5 ± 8.0	37.0 ± 7.7	39.6 ± 6.3
BMI (kg/m^2)	25.5 ± 4.1	23.4 ± 4.9[a]	21.6 ± 3.5[b]
BMD (Z score)			
Lumbar spine	0.74 ± 0.88	- 1.33 ± 1.28[c]	- 2.06 ± 0.73[c,d]
Total hip	0.48 ± 0.65	- 1.09 ± 1.12[c]	- 1.48 ± 0.69[c]
Femoral neck	0.35 ± 0.71	- 1.31 ± 1.15[c]	- 1.77 ± 0.76[c]
Distal radius (one third)	0.69 ± 0.89	0.26 ± 0.82[a]	0.01 ± 0.85[b]

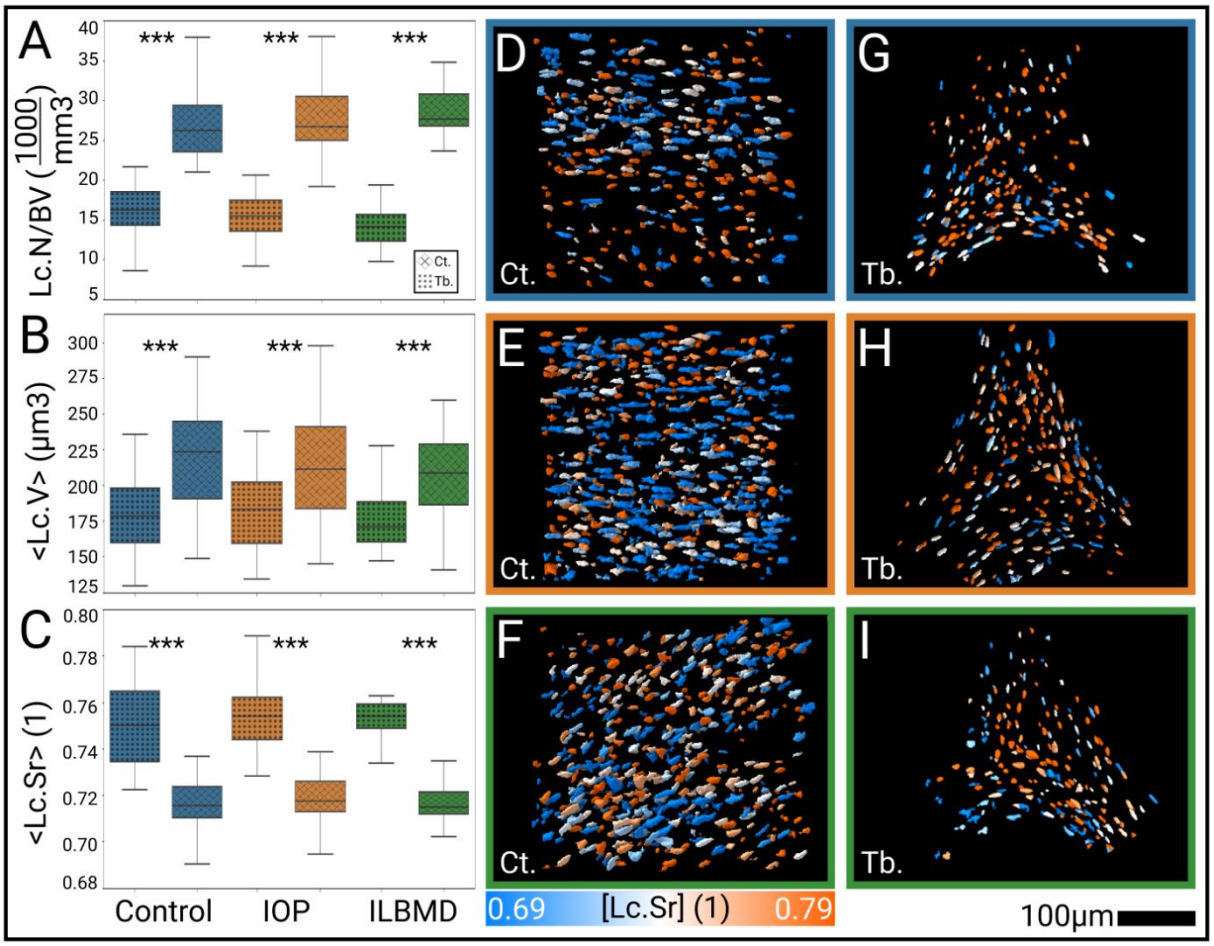

Figure 4.1.2: Mean distributions of selected lacunar parameters (A-C) and 3D visualizations of lacunae in both cortical regions (D-F) and trabecular regions (G-I). Local lacunar morphologies compared between region and group for A) lacunar density, B) lacunar volume, and C) lacunar sphericity. Differences between groups were not significant, yet differences between regions within groups were (***=p<0.001). D-F) 3D visualizations of biopsy subsection lacunae from cortical regions colored by [Lc.Sr] for control, IOP, and ILBMD groups respectively. G-I) 3D visualizations of biopsy subsection lacunae from trabecular regions colored by [Lc.Sr] for control, IOP, and ILBMD groups respectively. Biopsies selected for visualization were the median samples from each of the six groups plotted in C). Control (n=39); IOP (n=45); ILBMD (n=19).

Tissue Morphology

Lacunar morphometric indices for each of the subgroups were plotted against their trabecular and cortical tissue parameters in Figure 4.1.3A and 4.1.3B respectively. Each point represents the mean lacunar value from the individual biopsy. Clustering appeared to be tighter visually in the comparisons with trabecular tissue indices when compared to those with the cortical indices but were not significantly different. Apart from the strong and significant <Lc.Sr>

correlations in the right-most column in Figure 4.1.3A (listed in Table 4.1.2), weak correlations were present between several of the trabecular indices and lacunar indices such as volume <Lc.V>; however, none of these were significant.

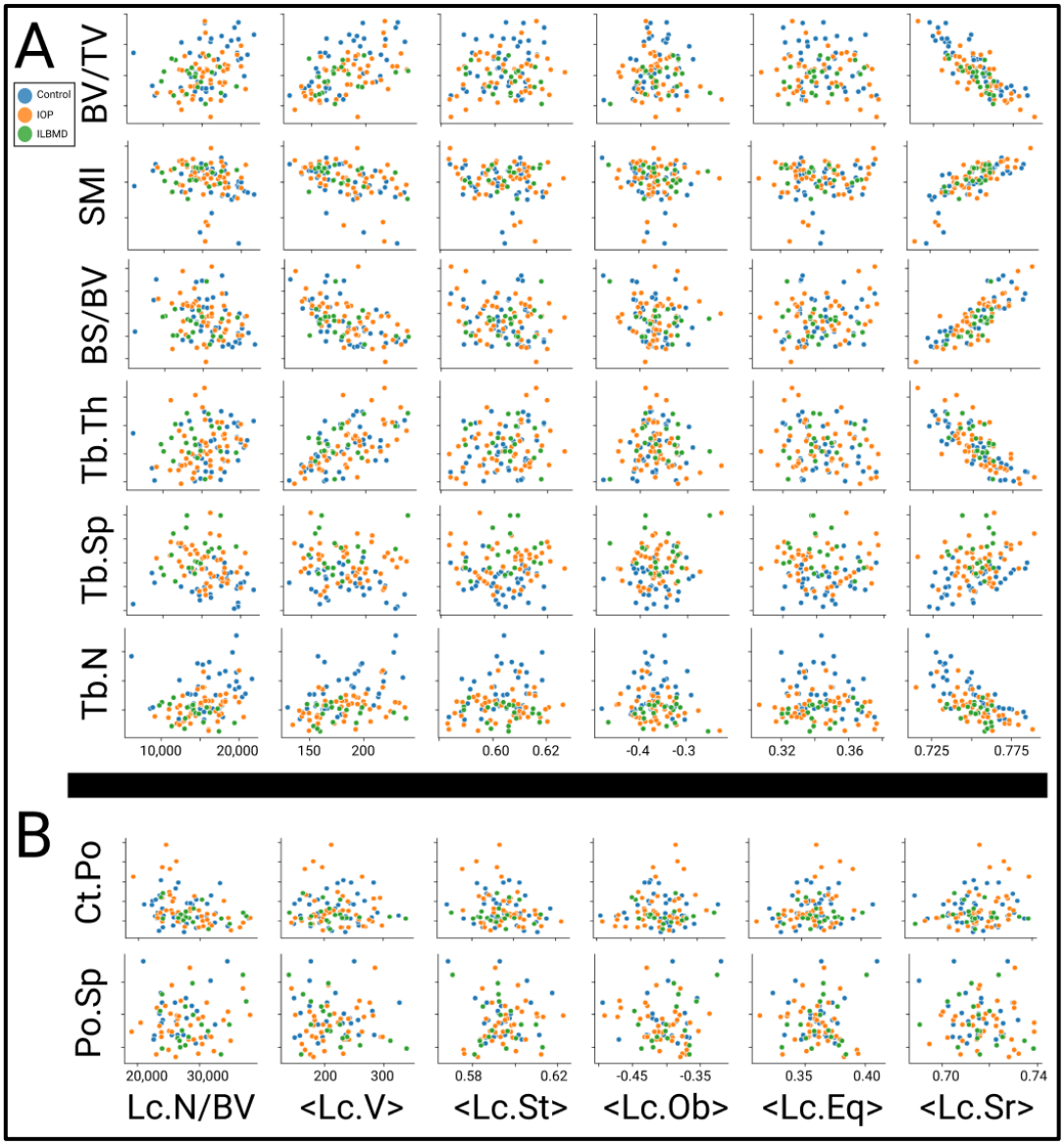

Figure 4.1.3: A) Two-parameter comparison between tissue parameters and lacunar morphometric parameters for lacunae from trabecular regions (n=103). B) Two-parameter comparison between tissue parameters and lacunar morphometric parameters for lacunae from cortical regions. Ct.Po measured in the 1.2µm images, while Po.Sp was measured in the 8µm images of biopsies where sufficient cortex was present for evaluation (n=79).

While no clear separation emerged between the control, IOP, and ILBMD groups, lacunar sphericity evaluated including all three groups was strongly correlated with all respective trabecular parameters as seen in Table 4.1.2. All correlations in Table 4.1.2 were significant except for the weakest correlations in the Tb.Sp and Tb.N groups. With respect to the cortical regions, Ct.Po was measured on the 1.2μm images while the Po.Sp values reflect the measurements from the 8μm images of which, only 79 biopsies contained a full cortex which was measurable at the tissue level.

Table 4.1.2: Correlations between <Lc.Sr> of lacunae in trabecular regions and measured global trabecular indices. * = p<0.05; **p<0.005; ***p<0.001.

Tissue Index	**Control (n=39)**	**IOP (n=45)**	**ILBMD (n=19)**	**Overall (n=103)**
BV/TV	R=0.88***	R=0.81***	R=0.76***	R=0.83***
SMI	R=0.75***	R=0.80***	R=0.71**	R=0.80*** (quadratic)
BS/BV	R=0.85***	R=0.82***	R=0.72**	R=0.82***
Tb.Th	R=-0.87***	R=-0.74***	R=-0.68**	R=-0.78***
Tb.Sp	R=0.54***	R=0.29	R=0.01	R=0.32**
Tb.N	R=-0.81***	R=-0.64***	R=-0.41	R=-0.68* (quadratic)

BV/TV percentages relative to grouping and the relationship between <Lc.Sr> and BV/TV were examined in greater detail in Figure 4.1.4. Figure 4.1.4A recapitulates the findings of Cohen et al. that IOP and ILBMD groups had significantly lower BV/TV relative to the control group (p<0.05; p<0.01) [18]. Significant differences did not emerge when comparing the same parameter between groups within the cortical regions in Figure 4.1.4B.

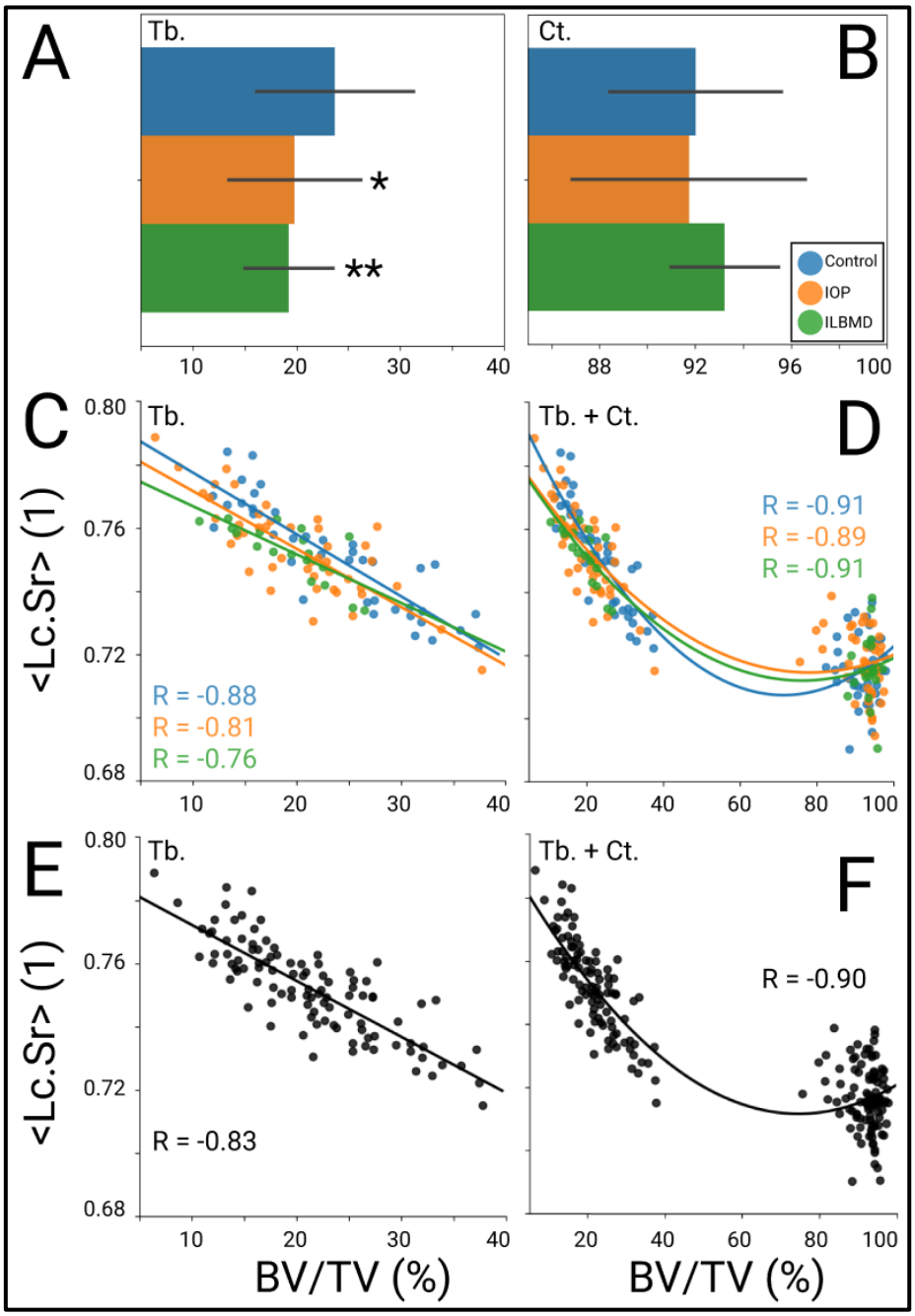

Figure 4.1.4: Comparisons and correlations of selected lacunar and tissue morphometric parameters. A) Tissue parameter comparisons between groups for trabecular BV/TV (adapted from Cohen et al. 2011; *=p<0.05, **=p<0.01) and B) cortical BV/TV. C) Linear relationship between <Lc.Sr> and BV/TV in trabecular regions for control (R=-0.88;p<0.001), IOP (R=-0.81;p<0.001), and ILBMD (R=-0.76;p<0.001) groups. D) Quadratic relationship between <Lc.Sr> and BV/TV including lacunae from both trabecular and cortical regions for control (R=-0.91;p<0.001), IOP (R=-0.89;p<0.001), and ILBMD (R=-0.91;p<0.001) groups. E) Linear relationship between <Lc.Sr> and BV/TV in trabecular regions irrespective of group (R=-0.83;p<0.001). F) Quadratic relationship between <Lc.Sr> and BV/TV including lacunae from both trabecular and cortical regions irrespective of group (R=-0.90;p<0.001). Control (n=39); IOP (n=45); ILBMD (n=19).

Sphericity <Lc.Sr> in trabecular regions was strongly linearly correlated with BV/TV within each group as seen in Figure 4.1.4C (R_control = -0.88, $p<0.001$; R_IOP = -0.81, $p<0.001$; R_ILBMD = -0.76, $p<0.001$) and also when evaluated irrespective of grouping in Figure 4.1.4E (R = -0.83, $p<0.05$). Lacunae from cortical regions were included in Figure 4.1.4D–F and revealed an even stronger, this time quadratic, correlation between <Lc.Sr> and BV/TV (R_control = -0.91, $p<0.001$; R_IOP = -0.89, $p<0.001$; R_ILBMD = -0.91, $p<0.001$). When evaluated irrespective of grouping, the correlations between <Lc.Sr> and BV/TV was R=-0.90, $p<0.001$ as presented in Figure 4.1.4F.

4.1.4 Discussion

In this study we investigated osteocyte lacuna distribution and morphology in transiliac biopsies from premenopausal women with IOP and ILBMD and a healthy control group. Contrary to previously published studies of postmenopausal osteoporotic women, lacunar morphology was not altered either in the entire group of affected subjects or when the IOP and ILBMD subgroups were compared to the control group [10-12]. Furthermore, there were no significant group differences with respect to the density of lacunae per bone volume (Lc.N/BV) or the total lacunar porosity (Lc.TV/BV). The inability to distinguish affected and control cohorts based on lacunar morphology was particularly intriguing because these groups differed significantly in previous studies when comparing their 3D microarchitecture, mechanical stiffness, histomorphometry, and biochemistry [18-20]. Yet our data suggest that these differences, which were present at larger spatial scales and in 2D analyses, did not extend to the cellular spatial scale in 3D in these distinct groups of women. These findings also point to the inherent difficulties that are typically associated with idiopathic conditions such as IOP, which may result from heterogeneous mechanisms and etiologies [33], as well as grouping otherwise healthy individuals into a low BMD group (ILBMD) [18]; the only criterion separating the two populations of IOP and ILBMD being an adult low-trauma fracture. This is also a reason to group the IOP and ILBMD subjects into a combined affected group for some analyses.

From a wider perspective, aging has been identified by many studies to be an important driver of osteocyte, lacunar, and canalicular morphology. Busse et al. have shown that lacunar density decreased linearly in humans with respect to age in periosteal and endosteal regions [16], which

has been corroborated by additional studies that reflect roughly a 15 to 30% reduction in lacunar density of aged cohorts [11, 14, 15, 34]. Animal studies, notably from Heveran et al., have found similar decreases in lacunar density with respect to age and also discovered lacunar volume to be smaller in old mice [35]. Considering the density of resident osteocytes in humans, a reduction with age has been shown to occur at an even greater pace than the reduction of lacunar density due to a large percentage of empty lacunae [36]. This percentage of empty lacunae has also been shown to increase with age in animal studies (roughly 20 – 30% more in old mice), further highlighting the importance of age in the reduction of viable osteocytes [37-39]. Compounding these two problems in old populations, the dendritic canalicular connections between lacunae have also been shown to decrease with age in both humans and mice [37, 40, 41].

These findings ultimately support the idea that age reduces the embedded network's functionality from an osteocyte, lacunae, and canalicular perspective. The fact that we find no differences in our lacunar morphometric analyses between affected and control groups of young subjects further strengthens the argument that lacunar changes are age-driven and that we observe our young IOP and ILBMD subjects do not have the characteristic traits of prematurely aged bone at the cellular scale. It is possible that IOP and ILBMD in young women are driven by completely different mechanisms than those causing postmenopausal osteoporosis. The origin of IOP and ILBMD could stem from a wide range of factors such as IGF-I imbalances or reduced osteoblast function, which ultimately may not be associated with morphological changes in osteocyte lacunae at all [42-46].

Within this large dataset of lacunar morphometric indices, strong differences were present between cortical and trabecular bone regions and were apparent both quantitatively and qualitatively as presented in Figure 4.1.2. Overall, lacunae were smaller, more spherical, and fewer per bone volume in trabecular bone when compared with cortical bone. Our previous publication detailing the imaging methodology, which was implemented in this study, examined a subset of the control biopsies (n=31) and found the same trends between trabecular and cortical lacunar measured morphometric parameters that we present here [22]. These regional differences extended beyond the healthy cohort and we noted similar differences in both IOP and ILBMD cohorts. The distribution of the lacunar morphometric parameters for the ILBMD cohort (Figure 4.1.2A-C) appeared slightly narrower than the other two groups; however, this may be due to the inclusion criteria for the recruitment with narrower DXA BMD

entry criteria (DXA; T score <= -2.5 or Z score <= -2.0) [18]. This was further confirmed by the narrow band of clustering of the ILBMD group in the scatter plots of the tissue morphometric indices (Figure 4.1.3). Figure 4.1.2D-I visually captured the regional differences between trabecular and cortical lacunae that we discovered and displayed the similarity between these lacunar characteristics in healthy, IOP, and ILBMD groups.

We observed strong correlations between <Lc.Sr> and trabecular tissue indices as described in Table 4.1.2 and visualized in Figure 4.1.3. Although every tissue index we reported is critical for bone microarchitecture quality, many are derived from each other, which also explains the similarities in correlation values in Table 4.1.2. BV/TV was the most clinically relevant tissue index we measured since bone mass is broadly used by clinicians to diagnose osteoporosis and osteopenia [47-50]. Therefore, we focused specifically on this relationship in Figure 4.1.4, demonstrating the strong, but similar, correlations between groups as well as the overall strong correlation when removing the grouping structure. These correlations between <Lc.Sr> and BV/TV were linear when considering lacunae from trabecular regions (Figure 4.1.4C&E). Yet when we included cortical lacunae, which were otherwise uncorrelated with <Lc.Sr> when evaluated alone (Figure 4.1.3B), we observed an even stronger, this time quadratic, relationship between <Lc.Sr> and BV/TV (Figure 4.1.4D&F). This connection between cortical and trabecular lacunae, which was independent of group (Figure 4.1.4F), suggests the possibility that osteocytes remodel their perilacunar space and adjust their lacunar shape similarly depending on the level of BV/TV, regardless of bone's deterioration at a global level. Furthermore, the quadratic trends we observed in Figure 4.1.4D&F emphasizes the importance of this relationship with respect to lacunae in low density, typically trabecular, regions of bone.

Specifically, we observed that lacunae were more spherical in patients with lower BV/TV. This variation in geometry may imply a change in mechanical sensitivity of the lacunar structure, and consequently on the resident osteocyte. Generalizing the range of lacunar shapes to include morphologies between a sphere and a prolate ellipsoid, we can estimate the hoop stress for these ideal geometries. Previously published work in the field of structural geology investigated this topic in porous inorganic material and found that hoop stresses in spherical geometries were roughly twice as high as those in prolate ellipsoids [51]. Applying this finding to our study, we infer that the stresses in spherical lacunae would be generally higher than those in more ellipsoidal lacunae. Furthermore, several previous studies have demonstrated the effect of lacunar stress amplification and its importance for the osteocyte mechanobiology, specifically

with respect to the transduction of cell signals [8, 9, 52]. Because of these findings and our correlations in Figure 4.1.4, it is a possibility that the osteocytes remodel their direct environment to create more spherical lacunae in regions of weak bone (low BV/TV) as a compensatory mechanism to amplify the mechanical signal. Even though the global remodeling of bone remains impaired, the osteocytes may attempt to correct for this by changing their shape to increase the relative mechanical signal, supporting previous assertions that osteocytes are capable of this type of modulation [10]. This was further supported by the correlation similarities between control, IOP, and ILBMD groups in Figure 4.1.4. Perhaps the bone remodeling process would be impaired further without these changes in lacunar sphericity. Yet, in general the changes in the osteocyte lacunar morphology did not appear to be a mechanism for global bone loss in this study, contrary to previously presented histomorphometric evidence in postmenopausal cohorts [13].

The results presented in this study build upon a decade of published findings from the biopsies performed in these premenopausal women [18-20]. The large cohort of healthy individuals (n=39) with which to compare IOP (n=45) and ILBMD (n=19) biopsies demonstrates the power present in our analysis. Within the 103 biopsies, ultimately 22.6 million osteocyte lacunae were measured and morphometrically evaluated. The scale of this lacunar dataset provides a new dimension of information to these biopsies in which the osteocytes were previously only analyzed with histology. Furthermore, our study was performed on a desktop microCT device providing ultra-high resolution and using a newly validated methodology, which illustrates the ability to perform a large-scale osteocyte lacuna imaging study without the need for synchrotron beam line facilities.

Our study also included several limitations, the largest of which being that this was a cross-sectional study and longitudinal data were not available. It is impossible to state definitively if osteocytes remodel their direct environment because of a reduction in BV/TV or if the converse is true: spherical lacunae drive the thinning trend of bone structures at a global level. Both longitudinal animal studies and improved computer simulations will be important to answer this question in future studies [53, 54]. Additionally, specific issues related to the clinical group definitions may have affected the results – since control and ILBMD subjects were recruited based on more narrow BMD criteria. Although the ILBMD group had microarchitectural findings that were quite similar to the IOP group, only the IOP group had a history of low trauma fractures in adulthood leading to greater certainty about a diagnosis of osteoporosis.

Furthermore, previous studies have shown that aBMD in small and thin women tends to be lower [55-59]. While the biopsies from our ILBMD group (the group with the lowest BMI) did contain microarchitectural defects [18], it is unknown whether this is an intrinsic characteristic of women with low aBMD and requires a larger population-based longitudinal study to assess further. Younger subjects also may have not yet attained their peak bone mass, and thus lacunar studies may have been affected by developmental changes. Measuring <Lc.Sr> with our previously published imaging method also included some uncertainty with respect to reproducibility (precision error = 0.24%), which manifested in the results we reported [22]. It will also be important for future studies to investigate lacunar morphologies in additional cohorts with different diseases and deficiencies. Perhaps disease driven lacunar changes only occur later in life and are not present in young populations. Additional diseases and hormonal states such as diabetes, osteonecrosis, renal osteodystrophy, and hyperparathyroidism are known to impact skeletal fragility, are associated with bone resorption, and thus, the lacunar morphologies from these populations will be important to compare with our dataset [60-65]. Furthermore, previous studies have suggested that in cohorts of men, IOP pathogenesis is associated with reduced osteoblast function – another important dataset to compare with lacunar morphometric parameters [45, 46].

Ultimately, we have successfully imaged 26.2 million lacunae in 103 human biopsies, which when coupled with previously measured 3D microarchitecture data, revealed a profound connection between lacunar sphericity and bone volume fraction. We also uncovered significant differences between lacunae in trabecular and cortical regions, which corroborates our previous findings within a subset of the control samples [22]. While we expected to discover differences in lacunar morphologies among the healthy, IOP and ILBMD groups, it is even more interesting to discover how consistent the distributions, trends, and relationships of lacunar morphologies remained across the three groups. Perhaps mechanisms leading to osteoporosis associated with aging are more likely to be associated with changes in lacunar morphology than the mechanisms underlying osteoporosis in younger cohorts with IOP and ILBMD. These findings provide a solid foundation for longitudinal studies, multiscale computer simulations of bone, and comparisons with other disease pathologies in the future.

References

[1] J. Gluhak-Heinrich, L. Ye, L.F. Bonewald, J.Q. Feng, M. MacDougall, S.E. Harris, D. Pavlin, Mechanical loading stimulates dentin matrix protein 1 (DMP1) expression in osteocytes in vivo, J Bone Miner Res 18(5) (2003) 807-17.

[2] A.G. Robling, P.J. Niziolek, L.A. Baldridge, K.W. Condon, M.R. Allen, I. Alam, S.M. Mantila, J. Gluhak-Heinrich, T.M. Bellido, S.E. Harris, C.H. Turner, Mechanical stimulation of bone in vivo reduces osteocyte expression of Sost/sclerostin, J Biol Chem 283(9) (2008) 5866-75.

[3] L. Lanyon, Osteocytes, strain detection, bone modeling and remodeling, Calcified tissue international 53(1) (1993) S102-S107.

[4] F.A. Schulte, D. Ruffoni, F.M. Lambers, D. Christen, D.J. Webster, G. Kuhn, R. Muller, Local mechanical stimuli regulate bone formation and resorption in mice at the tissue level, PLoS One 8(4) (2013) e62172.

[5] R. Huiskes, R. Ruimerman, G.H. van Lenthe, J.D. Janssen, Effects of mechanical forces on maintenance and adaptation of form in trabecular bone, Nature 405(6787) (2000) 704-6.

[6] L.D. You, S. Temiyasathit, P.L. Lee, C.H. Kim, P. Tummala, W. Yao, W. Kingery, A.M. Malone, R.Y. Kwon, C.R. Jacobs, Osteocytes as mechanosensors in the inhibition of bone resorption due to mechanical loading, Bone 42(1) (2008) 172-179.

[7] A. Santos, A.D. Bakker, H.M. Willems, N. Bravenboer, A.L. Bronckers, J. Klein-Nulend, Mechanical loading stimulates BMP7, but not BMP2, production by osteocytes, Calcif Tissue Int 89(4) (2011) 318-26.

[8] A.R. Bonivtch, L.F. Bonewald, D.P. Nicolella, Tissue strain amplification at the osteocyte lacuna: a microstructural finite element analysis, Journal of biomechanics 40(10) (2007) 2199-2206.

[9] A.R. Stern, D.P. Nicolella, Measurement and estimation of osteocyte mechanical strain, Bone 54(2) (2013) 191-5.

[10] R.P. van Hove, P.A. Nolte, A. Vatsa, C.M. Semeins, P.L. Salmon, T.H. Smit, J. Klein-Nulend, Osteocyte morphology in human tibiae of different bone pathologies with different bone mineral density - Is there a role for mechanosensing?, Bone 45(2) (2009) 321-329.

[11] M. Mullender, D. Van der Meer, R. Huiskes, P. Lips, Osteocyte density changes in aging and osteoporosis, Bone 18(2) (1996) 109-113.

[12] S. Qiu, D.S. Rao, S. Palnitkar, A.M. Parfitt, Reduced iliac cancellous osteocyte density in patients with osteoporotic vertebral fracture, Journal of bone and mineral research 18(9) (2003) 1657-1663.

[13] M. Mullender, S.D. Tan, L. Vico, C. Alexandre, J. Klein-Nulend, Differences in osteocyte density and bone histomorphometry between men and women and between healthy and osteoporotic subjects, Calcified tissue international 77(5) (2005) 291-296.

[14] D. Vashishth, O. Verborgt, G. Divine, M.B. Schaffler, D.P. Fyhrie, Decline in osteocyte lacunar density in human cortical bone is associated with accumulation of microcracks with age, Bone 26(4) (2000) 375-380.

[15] S. Qiu, D. Rao, S. Palnitkar, A. Parfitt, Age and distance from the surface but not menopause reduce osteocyte density in human cancellous bone, Bone 31(2) (2002) 313-318.

[16] B. Busse, D. Djonic, P. Milovanovic, M. Hahn, K. Püschel, R.O. Ritchie, M. Djuric, M. Amling, Decrease in the osteocyte lacunar density accompanied by hypermineralized lacunar occlusion reveals failure and delay of remodeling in aged human bone, Aging cell 9(6) (2010) 1065-1075.

[17] B. Busse, M. Hahn, T. Schinke, K. Püschel, G.N. Duda, M. Amling, Reorganization of the femoral cortex due to age-, sex-, and endoprosthetic-related effects emphasized by osteonal dimensions and remodeling, Journal of Biomedical Materials Research Part A: An Official Journal of The Society for Biomaterials, The Japanese Society for Biomaterials, and The Australian Society for Biomaterials and the Korean Society for Biomaterials 92(4) (2010) 1440-1451.

[18] A. Cohen, D.W. Dempster, R.R. Recker, E.M. Stein, J.M. Lappe, H. Zhou, A.J. Wirth, G.H. van Lenthe, T. Kohler, A. Zwahlen, R. Muller, C.J. Rosen, S. Cremers, T.L. Nickolas, D.J. McMahon, H. Rogers, R.B. Staron, J. LeMaster, E. Shane, Abnormal bone

microarchitecture and evidence of osteoblast dysfunction in premenopausal women with idiopathic osteoporosis, J Clin Endocrinol Metab 96(10) (2011) 3095-105.

[19] A. Cohen, X.S. Liu, E.M. Stein, D.J. McMahon, H.F. Rogers, J. LeMaster, R.R. Recker, J.M. Lappe, X.E. Guo, E. Shane, Bone Microarchitecture and Stiffness in Premenopausal Women with Idiopathic Osteoporosis, J. Clin. Endocrinol. Metab. 94(11) (2009) 4351-4360.

[20] A. Cohen, R.R. Recker, J. Lappe, D.W. Dempster, S. Cremers, D.J. McMahon, E.M. Stein, J. Fleischer, C.J. Rosen, H. Rogers, R.B. Staron, J. Lemaster, E. Shane, Premenopausal women with idiopathic low-trauma fractures and/or low bone mineral density, Osteoporos Int 23(1) (2012) 171-82.

[21] H.M. Heshmati, S. Khosla, Idiopathic osteoporosis: a heterogeneous entity, Ann. Med. Interne 149(2) (1998) 77-81.

[22] Elliott Goff, Federica Buccino, Chiara Bregoli, Jonathan P. McKinley, Basil Aeppli, Robert R. Recker, Elizabeth Shane, Adi Cohen, Gisela Kuhn, Ralph Müller, Large-scale quantification of human osteocyte lacunar morphological biomarkers as assessed by ultra-high-resolution desktop micro-computed tomography, Bone 152 (2021) 116094.

[23] A. Cohen, D.W. Dempster, R. Muller, X.E. Guo, T.L. Nickolas, X.S. Liu, X.H. Zhang, A.J. Wirth, G.H. van Lenthe, T. Kohler, D.J. McMahon, H. Zhou, M.R. Rubin, J.P. Bilezikian, J.M. Lappe, R.R. Recker, E. Shane, Assessment of trabecular and cortical architecture and mechanical competence of bone by high-resolution peripheral computed tomography: comparison with transiliac bone biopsy, Osteoporosis International 21(2) (2010) 263-273.

[24] P. Ruegsegger, B. Koller, R. Muller, A microtomographic system for the nondestructive evaluation of bone architecture, Calcified Tissue International 58(1) (1996) 24-29.

[25] T. Hildebrand, A. Laib, R. Muller, J. Dequeker, P. Ruegsegger, Direct three-dimensional morphometric analysis of human cancellous bone: Microstructural data from spine, femur, iliac crest, and calcaneus, Journal of Bone and Mineral Research 14(7) (1999) 1167-1174.

[26] T. Hildebrand, P. Ruegsegger, Quantification of Bone Microarchitecture with the Structure Model Index, Comput Methods Biomech Biomed Engin 1(1) (1997) 15-23.

[27] M.L. Bouxsein, S.K. Boyd, B.A. Christiansen, R.E. Guldberg, K.J. Jepsen, R. Muller, Guidelines for Assessment of Bone Microstructure in Rodents Using Micro-Computed Tomography, Journal of Bone and Mineral Research 25(7) (2010) 1468-1486.

[28] K.S. Mader, P. Schneider, R. Muller, M. Stampanoni, A quantitative framework for the 3D characterization of the osteocyte lacunar system, Bone 57(1) (2013) 142-54.

[29] Y. Carter, C.D.L. Thomas, J.G. Clement, A.G. Peele, K. Hannah, D.M.L. Cooper, Variation in osteocyte lacunar morphology and density in the human femur - a synchrotron radiation micro-CT study, Bone 52(1) (2013) 126-132.

[30] A. Carriero, M. Doube, M. Vogt, B. Busse, J. Zustin, A. Levchuk, P. Schneider, R. Muller, S.J. Shefelbine, Altered lacunar and vascular porosity in osteogenesis imperfecta mouse bone as revealed by synchrotron tomography contributes to bone fragility, Bone 61 (2014) 116-124.

[31] M.P. Akhter, D. Kimmel, J. Lappe, R. Recker, Effect of Macroanatomic Bone Type and Estrogen Loss on Osteocyte Lacunar Properties in Healthy Adult Women, Calcified Tissue International (2017) 1-12.

[32] M. Stauber, R. Muller, Volumetric spatial decomposition of trabecular bone into rods and plates - A new method for local bone morphometry, Bone 38(4) (2006) 475-484.

[33] S. Khosla, E.G. Lufkin, S.F. Hodgson, L.A. Fitzpatrick, L.J. Melton, Epidemiology and clinical features of osteoporosis in young individuals, Bone 15(5) (1994) 551-555.

[34] S. Mori, R. Harruff, W. Ambrosius, D. Burr, Trabecular bone volume and microdamage accumulation in the femoral heads of women with and without femoral neck fractures, Bone 21(6) (1997) 521-526.

[35] C.M. Heveran, A. Rauff, K.B. King, R.D. Carpenter, V.L. Ferguson, A new open-source tool for measuring 3D osteocyte lacunar geometries from confocal laser scanning microscopy reveals age-related changes to lacunar size and shape in cortical mouse bone, Bone 110 (2018) 115-127.

[36] S. Qiu, D. Rao, S. Palnitkar, A. Parfitt, Relationships between osteocyte density and bone formation rate in human cancellous bone, Bone 31(6) (2002) 709-711.

[37] L.M. Tiede-Lewis, Y.X. Xie, M.A. Hulbert, R. Campos, M.R. Dallas, V. Dusevich, L.F. Bonewald, S.L. Dallas, Degeneration of the osteocyte network in the C57BL/6 mouse model of aging, Aging-US 9(10) (2017) 2187-+.

[38] M. Piemontese, M. Almeida, A.G. Robling, H.-N. Kim, J. Xiong, J.D. Thostenson, R.S. Weinstein, S.C. Manolagas, C.A. O'Brien, R.L. Jilka, Old age causes de novo intracortical bone remodeling and porosity in mice, JCI insight 2(17) (2017).

[39] L.B. Meakin, G.L. Galea, T. Sugiyama, L.E. Lanyon, J.S. Price, Age-related impairment of bones' adaptive response to loading in mice is associated with sex-related deficiencies in osteoblasts but no change in osteocytes, Journal of Bone and Mineral Research 29(8) (2014) 1859-1871.

[40] P. Milovanovic, E.A. Zimmermann, M. Hahn, D. Djonic, K. Puschel, M. Djuric, M. Amling, B. Busse, Osteocytic Canalicular Networks: Morphological Implications for Altered Mechanosensitivity, ACS Nano 7(9) (2013) 7542-7551.

[41] K. Kobayashi, H. Nojiri, Y. Saita, D. Morikawa, Y. Ozawa, K. Watanabe, M. Koike, Y. Asou, T. Shirasawa, K. Yokote, Mitochondrial superoxide in osteocytes perturbs canalicular networks in the setting of age-related osteoporosis, Sci Rep 5(1) (2015) 1-11.

[42] E.S. Kurland, C.J. Rosen, F. Cosman, D. McMahon, F. Chan, E. Shane, R. Lindsay, D. Dempster, J.P. Bilezikian, Insulin-like growth factor-I in men with idiopathic osteoporosis, J. Clin. Endocrinol. Metab. 82(9) (1997) 2799-2805.

[43] Y. Pernow, E.M. Hauge, K. Linder, E. Dahl, M. Saaf, Bone Histomorphometry in Male Idiopathic Osteoporosis, Calcified Tissue International 84(6) (2009) 430-438.

[44] B.Y. Reed, J.E. Zerwekh, K. Sakhaee, N.A. Breslau, F. Gottschalk, C.Y.C. Pak, Serum Igf-1 Is Low And Correlated With Osteoblastic Surface In Idiopathic Osteoporosis, Journal of Bone and Mineral Research 10(8) (1995) 1218-1224.

[45] P.J. Marie, M.C. Devernejoul, D. Connes, M. Hott, Decreased Dna-Synthesis By Cultured Osteoblastic Cells In Eugonadal Osteoporotic Men With Defective Bone-Formation, J. Clin. Invest. 88(4) (1991) 1167-1172.

[46] S. Khosla, Idiopathic osteoporosis - Is the osteoblast to blame?, J. Clin. Endocrinol. Metab. 82(9) (1997) 2792-2794.

[47] J.A. Kanis, L.J. Melton III, C. Christiansen, C.C. Johnston, N. Khaltaev, The diagnosis of osteoporosis, Journal of bone and mineral research 9(8) (1994) 1137-1141.

[48] G. Karaguzel, M.F. Holick, Diagnosis and treatment of osteopenia, Reviews in endocrine and metabolic disorders 11(4) (2010) 237-251.

[49] G.M. Blake, I. Fogelman, The role of DXA bone density scans in the diagnosis and treatment of osteoporosis, Postgraduate medical journal 83(982) (2007) 509-517.

[50] A. El Maghraoui, C. Roux, DXA scanning in clinical practice, QJM: An International Journal of Medicine 101(8) (2008) 605-617.

[51] T. Davis, D. Healy, A. Bubeck, R. Walker, Stress concentrations around voids in three dimensions: The roots of failure, J. Struct. Geol. 102 (2017) 193-207.

[52] T.M. Skerry, L. Bitensky, J. Chayen, L.E. Lanyon, Early strain-related changes in enzyme activity in osteocytes following bone loading in vivo, J Bone Miner Res 4(5) (1989) 783-8.

[53] F.M. Lambers, G. Kuhn, F.A. Schulte, K. Koch, R. Muller, Longitudinal assessment of in vivo bone dynamics in a mouse tail model of postmenopausal osteoporosis, Calcif Tissue Int 90(2) (2012) 108-19.

[54] S.D. Badilatti, P. Christen, I. Parkinson, R. Müller, Load-adaptive bone remodeling simulations reveal osteoporotic microstructural and mechanical changes in whole human vertebrae, Journal of biomechanics 49(16) (2016) 3770-3779.

[55] M.R. Rubin, D.H. Schussheim, C.A.M. Kulak, E.S. Kurland, C.J. Rosen, J.P. Bilezikian, E. Shane, Idiopathic osteoporosis in premenopausal women, Osteoporosis International 16(5) (2005) 526-533.

[56] M.L. Gourlay, S.A. Brown, Clinical considerations in premenopausal osteoporosis, Arch. Intern. Med. 164(6) (2004) 603-614.

[57] K.E. Bainbridge, M. Sowers, X.H. Lin, S.D. Harlow, Risk factors for low bone mineral density and the 6-year rate of bone loss among premenopausal and perimenopausal women, Osteoporosis International 15(6) (2004) 439-446.

[58] C.A.M. Kulak, D.H. Schussheim, D.J. McMahon, E. Kurland, S.J. Silverberg, E.S. Siris, J.P. Bilezikian, E. Shane, Osteoporosis and low bone mass in premenopausal and perimenopausal women, Endocrine Practice 6(4) (2000) 296-304.

[59] M.R. Sowers, B. Shapiro, M.A. Gilbraith, M. Jannausch, Health And Hormonal Characteristics Of Premenopausal Women With Lower Bone Mass, Calcified Tissue International 47(3) (1990) 130-135.

[60] L. Karim, J. Moulton, M. Van Vliet, K. Velie, A. Robbins, F. Malekipour, A. Abdeen, D. Ayres, M.L. Bouxsein, Bone microarchitecture, biomechanical properties, and advanced glycation end-products in the proximal femur of adults with type 2 diabetes, Bone 114 (2018) 32-39.

[61] E.M. Lewiecki, P.D. Miller, Skeletal effects of primary hyperparathyroidism: bone mineral density and fracture risk, J. Clin. Densitom. 16(1) (2013) 28-32.

[62] K.J. Martin, K. Olgaard, J.W. Coburn, G.M. Coen, M. Fukagawa, C. Langman, H.H. Malluche, J.T. McCarthy, S.G. Massry, O. Mehls, Diagnosis, assessment, and treatment of bone turnover abnormalities in renal osteodystrophy, American journal of kidney diseases 43(3) (2004) 558-565.

[63] B. Hesse, M. Langer, P. Varga, A. Pacureanu, P. Dong, S. Schrof, N. Männicke, H. Suhonen, C. Olivier, P. Maurer, Alterations of mass density and 3D osteocyte lacunar properties in bisphosphonate-related osteonecrotic human jaw bone, a synchrotron µCT study, PloS one 9(2) (2014) e88481.

[64] J.R. Furst, L.C. Bandeira, W.W. Fan, S. Agarwal, K.K. Nishiyama, D.J. McMahon, E. Dworakowski, H. Jiang, S.J. Silverberg, M.R. Rubin, Advanced Glycation Endproducts and Bone Material Strength in Type 2 Diabetes, J Clin Endocrinol Metab 101(6) (2016) 2502-10.

[65] T. Rodic, E.M. Wölfel, P. Milovanovic, I.A. Fiedler, D. Cvetkovic, K. Jähn, M. Amling, J. Sopta, S. Nikolic, V. Zivkovic, Bone quality analysis of jaw bones in individuals with type 2 diabetes mellitus—post mortem anatomical and microstructural evaluation, Clinical Oral Investigations (2021) 1-24.

4.2 Investigation of clinical adiposity using lacunar biomarkers

Elliott Goff[1], Adi Cohen[2], Elizabeth Shane[2], Robert R. Recker[3], Gisela Kuhn[1], Ralph Müller[1]

[1] Institute for Biomechanics, ETH Zurich, Zurich, Switzerland

[2] Department of Medicine, Columbia University Vagelos College of Physicians & Surgeons, New York, NY, USA

[3] Department of Medicine, Creighton University Medical Center, Omaha, NE, USA

In preparation

Abstract

Visceral adipose tissue (VAT) has been linked with bone microarchitecture quality in previous studies: subjects with higher rates of VAT also had reduced bone volume density (BV/TV) as well as both fewer and thinner trabecular struts. Yet, whether this inverse relationship between VAT and bone quality persists at a cellular level remains an open question. Previous preliminary data suggest lower bone turnover as well as lower physical activity and higher levels of osteocyte secreted sclerostin in subjects with higher trunk fat. We hypothesized that the morphology of the lacunae, the fossilized shells of the mechanosensitive osteocytes, would change according to the subject's VAT. To test this hypothesis, we implemented a previously validated high-resolution micro-computed tomography (microCT) methodology to prepare, image, and measure three-dimensional lacunar morphometry on a large scale (9.92 million cells) in transiliac bone biopsies from a cohort of 39 healthy premenopausal women. We measured a collection of lacunar morphometric parameters: lacunar density (Lc.N/BV), lacunar porosity (Lc.TV/BV), lacunar number (Lc.N), lacunar volume (Lc.V), lacunar surface area (Lc.S), lacunar alignment (Lc.θ), lacunar stretch (Lc.St), lacunar oblateness (Lc.Ob), lacunar equancy (Lc.Eq), and lacunar sphericity (Lc.Sr). These lacunar measurements were evaluated

together with tissue parameters: bone volume density (BV/TV), trabecular separation (Tb.Sp), trabecular number (Tb.N), and trabecular thickness (Tb.Th), structure model index (SMI), cortical porosity (Ct.Po) and cortical pore spacing (Ct.Sp). VAT was approximated by trunk fat that was previously measured by dual x-ray absorptiometry (DXA), which allowed us to divide the cohort into tertile groups. While we did not uncover lacunar differences between central adiposity tertiles, we did discovered several significant correlations between Lc.Sr and BV/TV in both trabecular and cortical regions – indicating that perilacunar remodeling could be a local compensatory mechanism for a global reduction in bone quality. Moderate correlations were found in trabecular regions between Lc.Sr and age in low adiposity subjects as well as between Lc.Sr and overall adiposity. These relationships and the large dataset of lacunar morphometries generated in this study will be important for future inquiries regarding the connection between adiposity and bone quality.

4.2.1 Introduction

Obesity rates have exploded over the past several decades and have become a distinct challenge in the healthcare sector [1]. This unhealthy increase of body weight has been shown to increase fracture risk in patients of all ages, ethnicities, and sexes [2-6]. However, body weight has also been previously demonstrated to positively correlate with bone mineral density (BMD) as measured by dual-energy Xray absorptiometry (DXA) [7-10]. Recent studies have explored this seemingly paradoxical relationship between BMD and body fat by examining relationships with fat in different compartments. Abdominal fat, in particular, is inversely related to BMD, particularly after controlling for BMI [11-17]. The abdominal fat lining internal organs, known as visceral adipose tissue (VAT) and the fat located directly beneath the skin, subcutaneous adipose tissue (SAT), can be differentiated with quantitative computed tomography (CT). Comparing the two types of fat, VAT appears to be more strongly linked with a reduction in bone quality and BMD [12, 14, 18, 19]. VAT also has been shown to correlate strongly with trunk fat measured by DXA [20].

Many individuals struggling with abdominal obesity also tend to live a sedentary lifestyle, which leads to a reduction of the mechanical stimulation of bone: a crucial component for bone remodeling and overall bone health [21]. Bone senses and responds to mechanical stimulation on a cellular level via the osteocytes [22]. These osteocytes sit within individual ellipsoidal

structures called lacunae, which together compose bone's osteocyte lacunar network. Deformation of and fluid flow within the lacunar network via mechanical stimulation (i.e. exercise) is transduced by the osteocytes into chemical signals, which are sent to the surface cells (osteoblasts and osteoclasts) to orchestrate remodeling [23-25]. Therefore, the morphology of the individual lacunae which comprise this network are extremely important for what level of stimulus the resident osteocytes experience.

Cohen et al. recently investigated the relationship between adiposity and bone quality in a cohort of 40 healthy women [20]. They combined trunk fat data from full body DXA with a variety of tissue-level histomorphometric data from transiliac biopsies and discovered that women with high levels of central adiposity exhibited reduced bone quality: mainly lower trabecular bone volume (BV/TV), stiffness, and both fewer and thinner trabeculae. This trend continued in cortical regions as cortical porosity was higher in women with high adiposity. Histology also revealed a reduction in bone formation rate in women with high adiposity. Additionally, women with higher abdominal adiposity reported less physical activity and had higher serum sclerostin levels [26]. Osteocyte-secreted sclerostin is a negative regulator of bone formation that has been demonstrated to be down-regulated by mechanical stimulation [27]. These findings suggest that osteocytes and mechanoreception mediated by the lacunae may underlie the low bone formation/low bone volume phenotype seen in subjects with high abdominal adiposity. Therefore, we hypothesized that the morphology of the lacunar structures would change relative to levels of adiposity, a logical extension of the differences in sclerostin and the differences that exist at the tissue spatial scale.

To test this hypothesis, we used a new ultra-high resolution microCT methodology to acquire 3D images and a custom analysis tool to extract the morphological parameters of lacunae for this same cohort of women [28]. Overall, 9.92 million lacunae from 39 trans iliac crest bone biopsies (one excluded) were analyzed.

4.2.2 Materials and Methods

Patient population

A cohort of 40 premenopausal women (37 ± 8 yrs; BMI 20-39 kg/m^2) were recruited at Columbia University Medical Center (New York, New York, USA) and Creighton University

(Omaha, Nebraska, USA) as a control group to compare with cohorts of women with idiopathic osteoporosis (IOP) and idiopathic low bone mineral density (ILBMD) in previous research investigations. All subjects had not previously sustained adult low-trauma fractures and possessed normal areal bone mineral density (aBMD) measured with DXA (T score ≥ 1.0 or Z score ≥ 1.0). Whole-body fat and trunk fat (%) were measured by DXA. Additional information regarding the methods and selected subjects were previously reported in detail by Cohen et al. [29]. All subjects provided written informed consent. The institutional review boards of both institutions approved these studies.

MicroCT tissue analysis

Transiliac biopsies were surgically extracted and scanned with a microCT40 (Scanco Medical AG, Brüttisellen, Switzerland) with an 8μm nominal voxel resolution as previously described [30, 31]. Morphometric parameters of trabecular bone were measured using a direct 3D approach [32] and included: bone volume per total volume (BV/TV), trabecular thickness (Tb.Th), trabecular separation (Tb.Sp), and trabecular number (Tb.N). Structure model index (SMI) was also ascertained with the previously published method [33]. Finally, the morphometric parameters of cortical bone including porosity (Ct.Po) and pore spacing (Ct.Sp) were measured as previously described [34].

MicroCT lacunar analysis

Imaging and evaluation of lacunar morphometry was performed using a microCT50 (Scanco Medical AG, Brüttisellen, Switzerland) with a 1.2μm nominal voxel resolution as described in detail by Goff et al. [28]. As an overview, fresh biopsies were embedded in polymethylmethacrylate (PMMA) and machined into cylindrical subregions (3.8mm diameter x 10mm length). These subregions included both trabecular and cortical regions of each biopsy. One biopsy was excluded because it was too small (resulting in n=39). The trabecular and cortical 3D images were produced with the following scanning parameters which were optimized for this specific application: 72 μA current, 4 W power, 55 kVp energy, 1.5 s integration time, level 6 data averaging, and 1500 x-ray projections [28]. Following image acquisition, an individualized threshold rooted in the tissue mineral density (TMD) distribution was applied, and the image inverted, for the 3D image stack of each biopsy. The morphometric parameters of all segmented lacunae were determined using a combination of a custom Python

script (3.7.1, Python Software Foundation, Delaware, USA) and a scientific image evaluation software, XamFlow (Lucid AG, Zürich, Switzerland). The following morphometric indices were calculated: Lacunar porosity (Lc.TV/BV), lacunar density (Lc.N/BV), lacunar surface area (Lc.S), lacunar volume (Lc.V), lacunar alignment (Lc.θ), lacunar oblateness (Lc.Ob) and lacunar stretch (Lc.St) as described by Mader et al. [35], lacunar sphericity (Lc.Sr) as described by Akhter et al. [36], and lacunar equancy as defined by Carter et al. [37, 38]. Validation was performed on each of the aforementioned morphometric parameters via accuracy, reproducibility, and sensitivity [28].

Statistical analysis

Subjects were grouped into tertiles based on trunk fat as assessed by DXA. SPSS (IBM Corp., Version 24.0., Armonk, NY) was used to perform several Student's t-test including the necessary Bonferroni correction factor ($p<0.0083$) for all regional comparisons within adiposity (trunk fat) tertiles as seen in Figure 4.2.2. Pearson correlations were performed between tissue and lacunar indices and reported in Table 4.2.2. The relationship between <Lc.Sr> and BV/TV was evaluated in detail in Figure 4.2.4 also by means of Pearson correlations.

4.2.3 Results

Subject characteristics

Subjects were categorized by trunk fat as measured by full-body DXA and were grouped into tertiles accordingly. General characteristics of the subjects grouped by tertiles of trunk fat are reported in Table 4.2.1. Tertile groupings were applied from a previously published study, with one sample excluded from tertile 3, resulting in a total of n=39 (low tertile, n=13; middle tertile, n=14; high tertile, n=12).

Table 4.2.1: Characteristics of the Subjects Grouped by Tertiles of Trunk Fat by DXA.

Tertiles based upon DXA Trunk fat	**Low Tertile (n=13)**	**Mid Tertile (n=14)**	**High Tertile (n=12)**
Age (yrs)	33.3 ± 7.6	38.9 ± 8.8	40.5 ± 6.2
BMI (kg/m^2)	21.6 ± 1.3	26.0 ± 3.1	29.0 ± 3.7
DXA Trunk fat (%)	22.3 ± 3.5	32.9 ± 3.2	41.8 ± 2.8
BMD by DXA (g/cm^2)			
Lumbar Spine	1.11 ± 0.12	1.09 ± 0.06	1.09 ± 0.10
Total Hip	1.01 ± 0.09	0.96 ± 0.06	0.98 ± 0.08
Femoral Neck	0.88 ± 0.08	0.86 ± 0.07	0.85 ± 0.07

Lacunar morphology

As displayed in Figure 4.2.1, lacunar morphometric parameters were compared with each other in both cortical and trabecular regions. Histograms reveal the distribution of all 9.92 million lacunae for each specific morphometric parameter, and the scatter plots each contain 39 data points, which represent an average value (normalized to the number of lacunae present) for each subject. Individual lacunar morphometric parameters were reported including: Lc.V, Lc.S, Lc.St, Lc.Ob, Lc.Eq, Lc.Sr. The distributions of these parameters between the three central adiposity groups were very similar, and correlations between parameters (other than related variables such as Lc.V and Lc.S) did not readily emerge. The distributions of the entire populations of lacunae appeared different between the central adiposity groups for global lacunar parameters such as Lc.TV/BV and Lc.N/BV, however these differences were not significant. In general, no separations could be made between the adiposity groups of the lacunar morphometric parameters in Figure 4.2.1, and the same was also true for the population distributions of the three central adiposity groups in the same Figure.

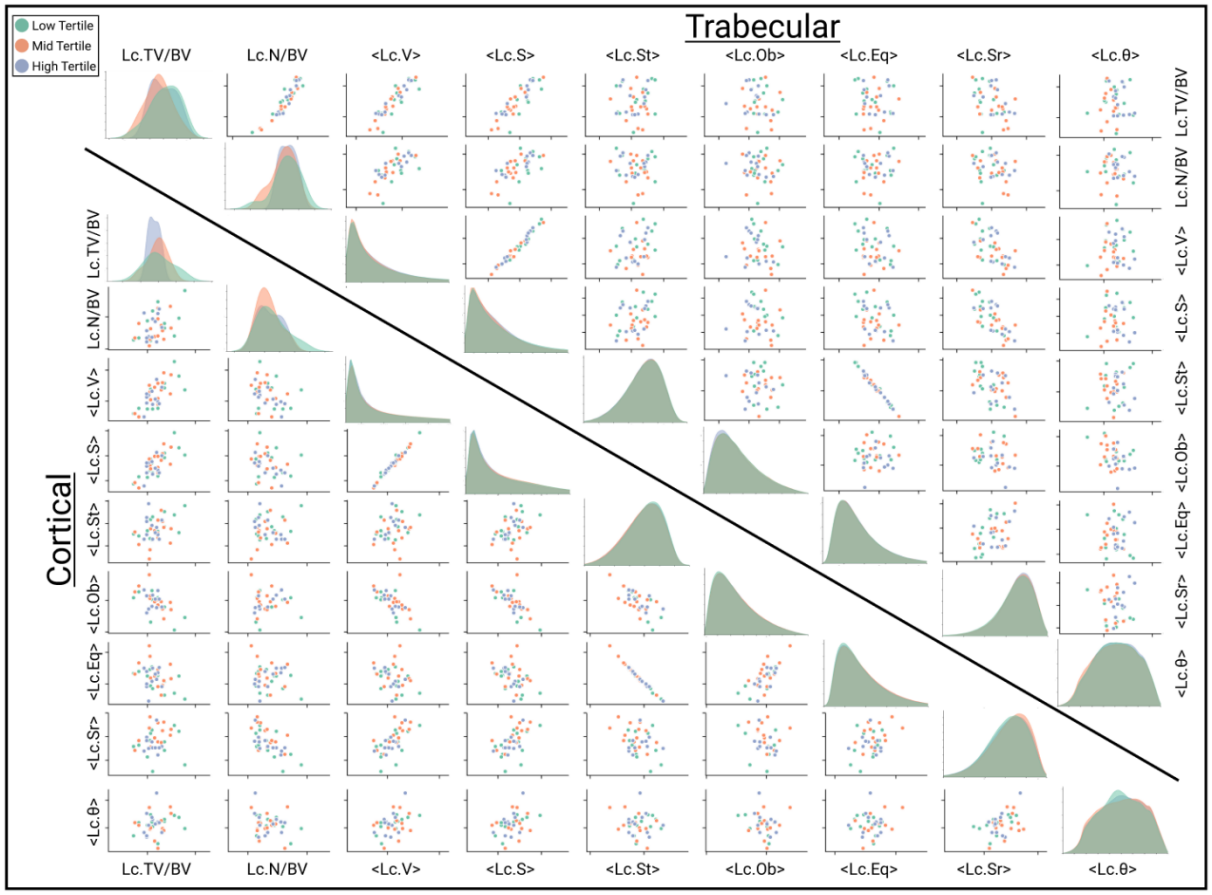

Figure 4.2.1: Lacunar morphometric parameters overview relative to one another. Morphometric parameter clustering and distributions for trabecular regions (top) and cortical regions (bottom). Each scatter plot point is the mean value of all lacunae from an individual biopsy region (low tertile, n=13; middle tertile, n=14; high tertile, n=12). Histograms display the distribution of the total lacuna population (n= 9,917,909) from each of the analyzed groups from both regions (Cortical: low tertile, n=3,165,213; middle tertile, n=2,615,541; high tertile, n=2,591,136. Trabecular: low tertile, n=608,454; middle tertile, n=525,032; high tertile, n=412,533).

Although differences between the lacunar morphometric parameters were not found within the respective cortical and trabecular regions for the central adiposity subgroups, differences were present when comparing the morphometric indices between the cortical and trabecular regions as a whole. This was true for all three adiposity groups with respect to Lc.N/BV and Lc.Sr ($p<0.001$) as seen in Figure 4.2.2A-C. With respect to Lc.V, only the middle adiposity group was significantly different between cortical and trabecular regions (Figure 4.2.2B). In general, the trend for lacunar size was to be larger in cortical regions and more lacunae per bone volume were found as well. However, lacunar structures were significantly more spherical in trabecular regions across the three adiposity groups. These differences (Figure 4.2.2A-C) are visualized

in 3D (Figure 4.2.2D-I) for qualitative inspection and comparison. In these 3D visualizations, the median samples from Figure 4.2.2C were selected and colored based on sphericity. Overall, the cortical lacunae in Figure 4.2.2D-F look to be flatter, larger, and more densely packed together than the lacunae in their trabecular counterpart in Figure 4.2.2G-I.

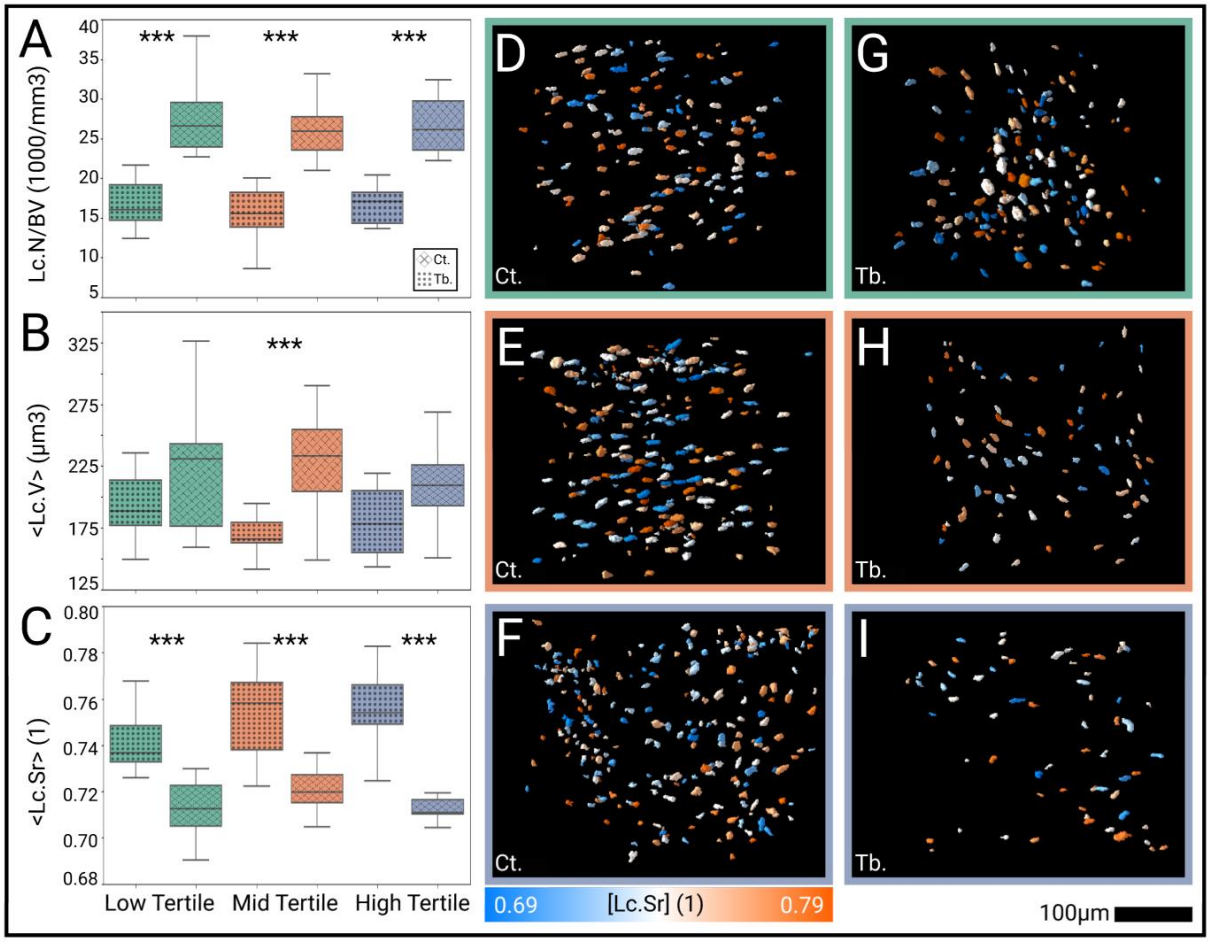

Figure 4.2.2: Mean distributions of selected lacunar parameters (A-C) and 3D visualizations of lacunae in both cortical regions (D-F) and trabecular regions (G-I). Local lacunar morphologies compared between region and group for A) lacunar density, B) lacunar volume, and C) lacunar sphericity. Differences between groups were not significant, yet differences between regions within groups were (***=$p<0.001$) in most cases. D-F) 3D visualizations of biopsy subsection lacunae from cortical regions colored by [Lc.Sr] for low, mid-, and high adiposity groups, respectively. G-I) 3D visualizations of biopsy subsection lacunae from trabecular regions colored by [Lc.Sr] for low, mid, and high adiposity groups respectively. Biopsies selected for visualization were the median samples from each of the six groups plotted in C). Low tertile (n=13); Middle tertile (n=14); High tertile (n=12).

Tissue Morphology

Trabecular and cortical morphometric indices were compared with lacunar morphometric parameters in Figure 4.2.3A and B. Similar to Figure 4.2.1, each plotted point represents a mean value from each individual biopsy which was normalized to the number of lacunae present. In trabecular regions, lacunar morphometric parameters did not correlate with tissue indices except for Lc.Sr. These correlations and their respective significance are presented in Table 4.2.2. Lc.Sr was also loosely correlated with overall adiposity in the group as a whole (R=0.39) as well as with age in the low adiposity group (R=0.56). Clear demarcations between the data points in the adiposity scatter plots are visible; however, this is to be expected because the tertile groupings are based on rates of trunk fat adiposity as measured by DXA.

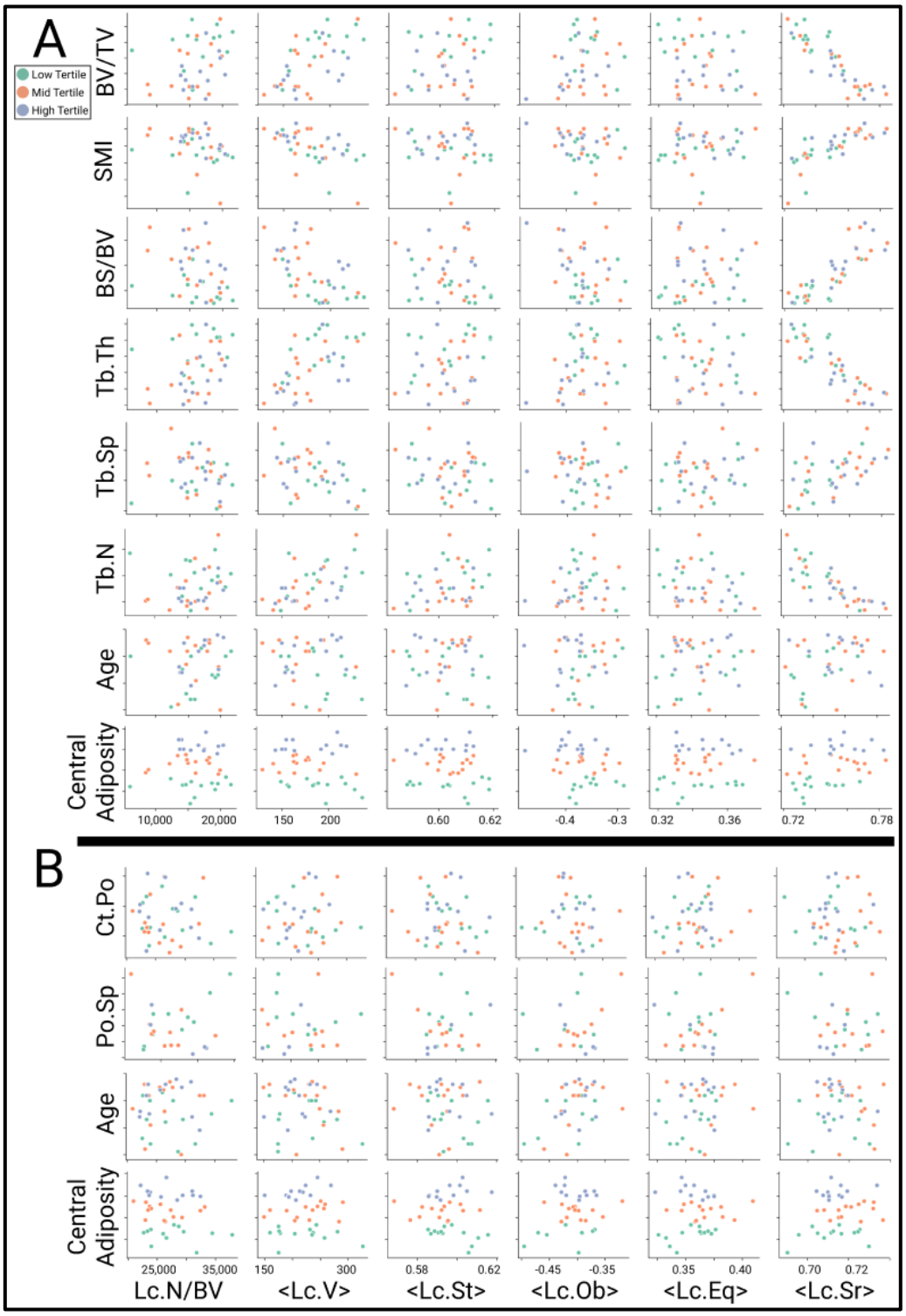

Figure 4.2.3: A) Two-parameter comparison between lacunar morphometric parameters and tissue parameters for lacunae from trabecular regions (n=1,546,019). B) Two-parameter comparison between lacunar morphometric parameters and tissue parameters. Ct.Po was calculated locally from the 1.2um images while Po.Sp was calculated from the 8um images in samples where sufficient cortex was present for evaluation (n=25).

The cortical parameter Po.Sp was only evaluated for 25 biopsies since not all 39 samples contained an optimal cortex to measure. However, age and adiposity were compared for all 39 biopsies since lacunae were measurable in all samples.

Table 4.2.2: Correlations between <Lc.Sr> of lacunae in trabecular regions and measured trabecular indices as well as age and central adiposity tertiles based on DXA trunk fat and in the group as a whole (overall). * = p<0.05; **p<0.005; ***p<0.001.

Tissue Index	**Low Tertile (n=13)**	**Mid Tertile (n=14)**	**High Tertile (n=12)**	**Overall (n=39)**
BV/TV	R=-0.80**	R=-0.92***	R=-0.83**	R=-0.88***
SMI	R=0.58*	R=0.87***	R=0.67*	R=0.75***
BS/BV	R=0.76**	R=0.81***	R=0.86***	R=0.85***
Tb.Th	R=-0.63**	R=-0.87***	R=-0.88***	R=-0.87***
Tb.Sp	R=0.54*	R=0.65*	R=0.18	R=0.54***
Tb.N	R=-0.76**	R=-0.89***	R=-0.61*	R=-0.81***
Age	R=0.56*	R=0.28	R=-0.42	R=0.29
Central Adiposity	R=0.30	R=0.15	R=0.04	R=0.39*

The relationship between <Lc.Sr> and BV/TV as well as BV/TV percentages relative to adiposity tertile group were investigated further in Figure 4.2.4. Figure 4.2.4A and B explore the differences between BV/TV in the different adiposity groups in trabecular and cortical bone, respectively. The middle and high central adiposity groups were significantly different from the low central adiposity tertile in trabecular bone. However, these significant differences did not extend to cortical regions although the high adiposity group did tend to be lower than the low adiposity group but this was not significant.

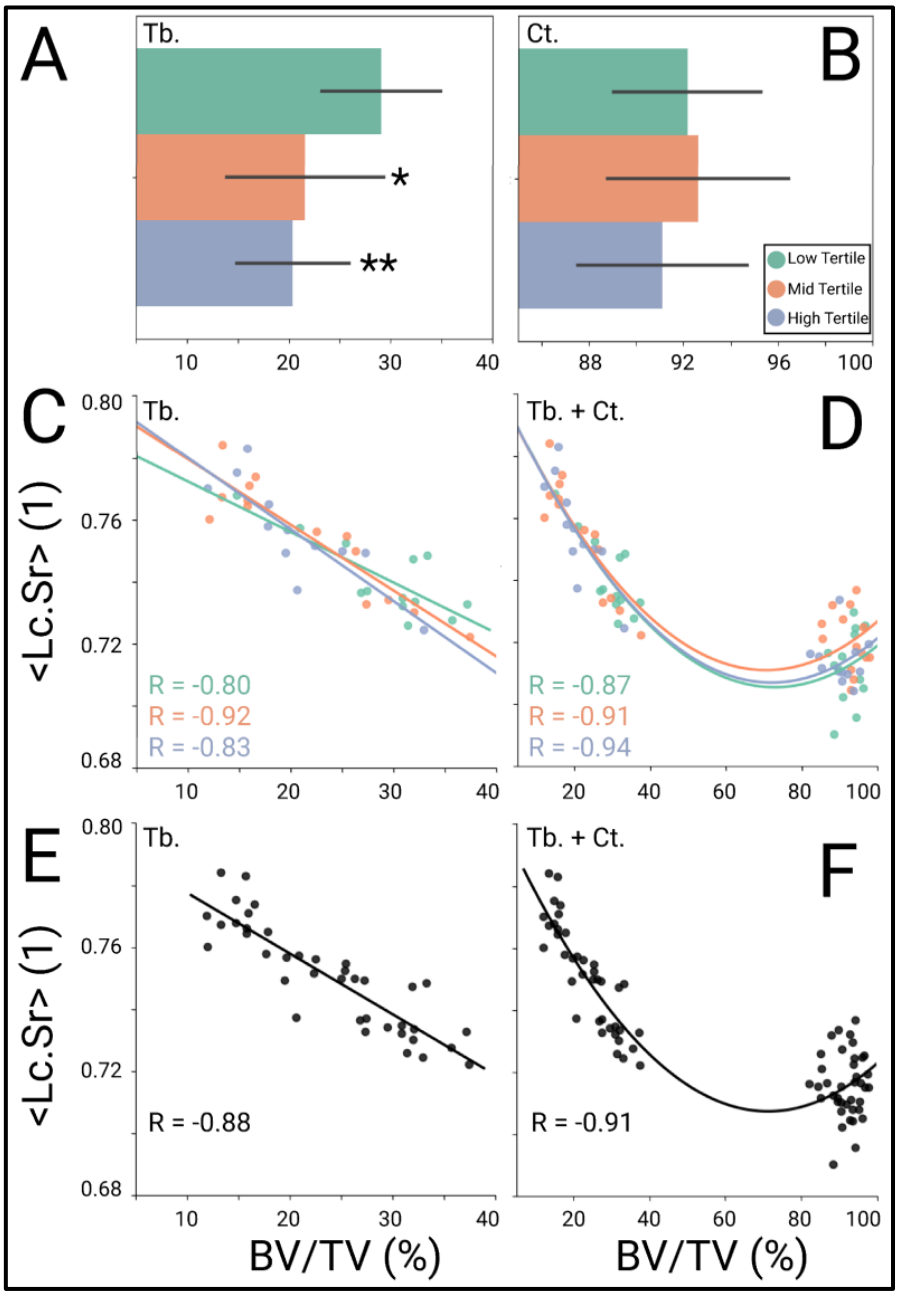

Figure 4.2.4: Comparisons and correlations of selected lacunar and tissue morphometric parameters. A) Tissue parameter comparisons between groups for trabecular BV/TV (*=p<0.05, **=p<0.01) and B) cortical BV/TV. C) Linear relationship between <Lc.Sr> and BV/TV in trabecular regions for low tertile (R=-0.80;p<0.001), mid tertile (R=-0.92;p<0.001), and high tertile (R=-0.83;p<0.001) groups. D) Quadratic relationship between <Lc.Sr> and BV/TV including lacunae from both trabecular and cortical regions for low tertile (R=-0.87;p<0.001), mid tertile (R=-0.91;p<0.001), and high tertile (R=-0.94;p<0.001) groups. E) Linear relationship between <Lc.Sr> and BV/TV in trabecular regions irrespective of group (R=-0.88;p<0.001). F) Quadratic relationship between <Lc.Sr> and BV/TV including lacunae from both trabecular and cortical regions irrespective of group (R=-0.91;p<0.001). Low tertile (n=13); Mid tertile (n=14); High tertile (n=12).

In trabecular regions lacunar sphericity <Lc.Sr> was strongly correlated in a linear fashion with BV/TV within each adiposity group (R_low = -0.80, p<0.001; R_mid = -0.92, p<0.001; R_high = -0.83, p<0.001) and also when removing the group structure as seen in Figures 4.2.4C and E, respectively (R = -0.88, p<0.05). When also including lacunae from cortical regions with the lacunae from trabecular regions and performing the same correlation (Figure 4.2.4D), the relationship became quadratic and was even stronger between BV/TV and <Lc.Sr> (R_low = -0.87, p<0.001; R_mid = -0.91, p<0.001; R_high = -0.94, p<0.001) and also when removing the grouping structure (R=-0.91, p<0.001) as seen in Figure 4.2.4F.

4.2.4 Discussion

In this study we explored the distribution and morphology of osteocyte lacunae from transiliac biopsies of a healthy group of women with different central adiposity levels. The cohort was divided into tertiles based on DXA-measured trunk fat. Contrasting a previous study on the same cohort that uncovered significant differences between DXA trunk fat and tissue morphometric parameters, histomorphometry, and biochemistry [20], differences at the lacunar level between adiposity rates in this study did not readily emerge. The similarity between the adiposity tertiles was apparent even when comparing morphometric parameters that consider all lacunae such as lacunar density per bone volume (Lc.N/BV) and lacunar porosity (Lc.TV/BV). This was surprising because several studies have previously published results demonstrating that central adiposity is strongly linked with a reduction in BMD and overall bone quality [12, 14, 18, 19]. However, the data from this lacunar analysis using HR-microCT provide evidence that the differences discovered at the tissue scale, within blood markers, and in histomorphometric analyses relative to central adiposity do not extend to the 3D lacunar level within this specific cohort of 39 women.

Regional differences emerged when comparing lacunae from trabecular and cortical images both qualitatively and quantitatively (Figure 4.2.2). In cortical bone, there were more lacunae per bone volume that were less spherical than in their trabecular counterpart in all central adiposity tertiles. Lacunae were significantly smaller in trabecular bone when compared with cortical bone in the middle adiposity tertile, however, this trend was not significant in the high and low adiposity tertiles. These findings agree with our previous publications in which we discovered the same differences in lacunar morphometric parameters between cortical and

trabecular lacunae when examining a subset of our healthy cohort (n=31) as well as two additional diseased cohorts (n=45, n=19) [28]. Therefore, the fact that these trends continue even when the cohort was separated into adiposity tertiles indicates that these regional differences are a fundamental aspect of osteocyte lacunae, conserved in many different populations. These quantitative differences were displayed visually in Figure 4.2.2D-I, which both depicted the similarities between adiposity tertiles as well as the differences between the cortical and trabecular regions within the tertiles.

Trabecular tissue indices were strongly correlated with <Lc.Sr> in each of the adiposity tertiles as well as when all biopsies were evaluated together. We extended these <Lc.Sr> correlations to include age and adiposity in Table 4.2.2; however, these correlations were much weaker and only significant correlations were between <Lc.Sr> in the first tertile ($R=0.56$, $p<0.05$) and between <Lc.Sr> in the overall comparison ($R=0.39$, $p<0.05$). Considering all the indices we evaluated, bone mass (BV/TV) held the most clinical relevance since it is regularly used to diagnose diseases such as osteoporosis and osteopenia and was strongly correlated with <Lc.Sr> overall ($R=-0.88$, $p<0.001$) [39-42]. Because of this, we explored the correlation in greater detail as seen in Figure 4.2.4, which illustrates the strong correlations within each adiposity tertile individually and also the strong correlation when considering all biopsies independently of tertile group. Lacunae from trabecular regions were linearly correlated (Figure 4.2.4C&E), yet when adding lacunae from cortical regions, the relationship between <Lc.Sr> and BV/TV became quadratic (Figure 4.2.4D&F). This is interesting because no correlation was present between <Lc.Sr> and BV/TV when evaluating cortical lacunae alone (Figure 4.2.3B). The strong connection between lacunae from both regions suggests that regardless of the adiposity tertile, osteocyte lacunae adjust their shape via perilacunar remodeling.

In patients with lower BV/TV we discovered that lacunae were more spherical across all adiposity tertiles. We extrapolate this geometric change to also indicate a change in the mechanical sensitivity of the lacunar shape and of the ensconced osteocyte. Lacunar morphology can be estimated as a range between a prolate ellipsoid and a sphere; consequently, we can calculate the hoop stress for the range of idealized 3D geometries. This topic was previously investigated in a study of structural geology and the authors estimated that the hoop stresses in prolate ellipsoids were roughly half as high as those in spherical geometries [43]. This result can be applied to our study and consequently we assume that the stresses in ellipsoidal lacunae would be generally lower than those in more spherical ones. Additionally,

lacunar stress amplification and its implications for osteocyte mechanobiology, specifically cell signaling, has been confirmed by several previous studies [44-46]. Based on these previous studies and the strong correlations we present in Figure 4.2.4, we assert the possibility that osteocytes engage in perilacunar remodeling to create more spherical morphologies in regions of low BV/TV to amplify the applied mechanical signal regardless of the subject's adiposity. However, from an anatomical perspective, the iliac crest is likely less weight dependent than other bones such as the femur and this should be further investigated. Lacunar compensation is perhaps less necessary in bones that experience higher loads. Finally, in trabecular bone there was a slight positive correlation between central adiposity and <Lc.Sr> indicating that lacunae become more spherical in patients with higher central adiposity, which Cohen et al. also showed have reduced bone microarchitecture quality [20]. Perhaps these correlations could be indicative of a compensatory mechanism at the cell level to correct for reduced bone quality at the global level or even to account for less physical activity of the individual. However, while previous studies in postmenopausal cohorts demonstrate changes in lacunar morphology as a mechanism for bone loss, we did not observe such broad changes in the lacunar morphology of our cohort [47]. Yet, we did observe a moderate correlation between age and <Lc.Sr> in the low adiposity tertile, which alludes to the possibility of lacunar morphology being age dependent.

Our lacunar morphological analysis in relation to adiposity levels adds a new 3D perspective to the previously published 2D histological lacunar data from this cohort of healthy premenopausal women [20]. 9.92 million osteocyte lacunae were morphometrically evaluated within these 39 biopsies, demonstrating the power of our analysis. Furthermore, this investigation of lacunar morphology relative to adiposity adds to the growing body of literature surrounding lacunar analysis using a newly developed and validated desktop microCT imaging methodology, bypassing the need for synchrotron beamline facilities as has been required by similar previous studies [28, 35].

The lack of longitudinal data to pair with our cross-sectional study was a large limitation of this analysis. Perilacunar remodeling could be driven by strongly and/or weakly correlated parameters such as BV/TV, age, and adiposity; however, the converse could also be true and the driving factor (BV/TV) of these global parameters could be the shape of the lacunae. Longitudinal animal experiments and high-resolution computer simulations will be required to uncover a causal relationship [48, 49]. Furthermore, the demarcation of adiposity tertiles was

chosen to create roughly equal sample sizes and assumes that the 39 subjects are representative of the adiposity range in the general population. Subjects with very high BMI (BMI > 40) were excluded from the biopsy study, which limits what can be ascertained about that population. Recruitment for our subjects was not based on adiposity and this will be an important experimental design criterion in future adiposity studies. A key finding in this study was the strong relationship between <Lc.Sr> and clinically relevant tissue measures including BV/TV, yet it is important to mention that a level of uncertainty was included in this morphometric measurement (precision error = 0.24%) and was explained in greater detail in our methods paper [28]. We found a moderate correlation between age and <Lc.Sr> in the low adiposity group which suggests that perhaps this correlation would continue in a future study considering postmenopausal women.

In this study, we imaged 9.92 million lacunae in 39 human biopsies of premenopausal women. We discovered a strong connection between <Lc.Sr> and BV/TV, while also uncovering weaker correlations between <Lc.Sr> and age as well as adiposity. The regional differences in lacunar morphology that we observed in all adiposity groups confirm our previous findings in a subset of these 39 biopsies [28] as well as similar differences in IOP and ILBMD disease cohorts. Although we expected to see differences in lacunar morphology between the adiposity tertile groups, as have been previously demonstrated with other measurements for this cohort, it is intriguing that what we observed was a high degree of consistency between the tertiles for all measures. This investigation of high-resolution lacunar images from the perspective of adiposity in premenopausal women adds a new layer to our understanding of this cohort and will provide a foundation for future endeavors in this direction.

References

[1] K.M. Flegal, M.D. Carroll, B.K. Kit, C.L. Ogden, Prevalence of obesity and trends in the distribution of body mass index among US adults, 1999-2010, Jama 307(5) (2012) 491-497.

[2] J.E. Compston, J. Flahive, D.W. Hosmer, N.B. Watts, E.S. Siris, S. Silverman, K.G. Saag, C. Roux, M. Rossini, J. Pfeilschifter, Relationship of weight, height, and body mass index with fracture risk at different sites in postmenopausal women: the Global Longitudinal study of Osteoporosis in Women (GLOW), Journal of Bone and Mineral Research 29(2) (2014) 487-493.

[3] J.E. Compston, N.B. Watts, R. Chapurlat, C. Cooper, S. Boonen, S. Greenspan, J. Pfeilschifter, S. Silverman, A. Díez-Pérez, R. Lindsay, Obesity is not protective against fracture in postmenopausal women: GLOW, The American journal of medicine 124(11) (2011) 1043-1050.

[4] C.M. Nielson, L.M. Marshall, A.L. Adams, E.S. LeBlanc, P.M. Cawthon, K. Ensrud, M.L. Stefanick, E. Barrett-Connor, E.S. Orwoll, O.F.i.M.S.R. Group, BMI and fracture risk in older men: the osteoporotic fractures in men study (MrOS), Journal of Bone and Mineral Research 26(3) (2011) 496-502.

[5] L. Laslett, S.J. nee Foley, S. Quinn, T. Winzenberg, G. Jones, Excess body fat is associated with higher risk of vertebral deformities in older women but not in men: a cross-sectional study, Osteoporosis International 23(1) (2012) 67-74.

[6] A. Goulding, A.M. Grant, S.M. Williams, Bone and body composition of children and adolescents with repeated forearm fractures, Journal of Bone and Mineral Research 20(12) (2005) 2090-2096.

[7] K.O. Klein, K.A. Larmore, E. de Lancey, J.M. Brown, R.V. Considine, S.G. Hassink, Effect of obesity on estradiol level, and its relationship to leptin, bone maturation, and bone mineral density in children, The journal of clinical endocrinology & metabolism 83(10) (1998) 3469-3475.

[8] I.R. Reid, L.D. Plank, M.C. Evans, Fat mass is an important determinant of whole body bone density in premenopausal women but not in men, The Journal of Clinical Endocrinology & Metabolism 75(3) (1992) 779-782.

[9] C. Albala, M. Yanez, E. Devoto, C. Sostin, L. Zeballos, J. Santos, Obesity as a protective factor for postmenopausal osteoporosis, International journal of obesity and related metabolic disorders: journal of the International Association for the Study of Obesity 20(11) (1996) 1027-1032.

[10] M. Yamauchi, T. Sugimoto, T. Yamaguchi, D. Nakaoka, M. Kanzawa, S. Yano, R. Ozuru, T. Sugishita, K. Chihara, Plasma leptin concentrations are associated with bone mineral density and the presence of vertebral fractures in postmenopausal women, Clinical endocrinology 55(3) (2001) 341-347.

[11] L.-J. Zhao, Y.-J. Liu, P.-Y. Liu, J. Hamilton, R.R. Recker, H.-W. Deng, Relationship of obesity with osteoporosis, The Journal of Clinical Endocrinology & Metabolism 92(5) (2007) 1640-1646.

[12] M.A. Bredella, M. Torriani, R.H. Ghomi, B.J. Thomas, D.J. Brick, A.V. Gerweck, L.M. Harrington, A. Breggia, C.J. Rosen, K.K. Miller, Determinants of bone mineral density in obese premenopausal women, Bone 48(4) (2011) 748-754.

[13] M.A. Bredella, M. Torriani, R.H. Ghomi, B.J. Thomas, D.J. Brick, A.V. Gerweck, C.J. Rosen, A. Klibanski, K.K. Miller, Vertebral bone marrow fat is positively associated with visceral fat and inversely associated with IGF-1 in obese women, Obesity 19(1) (2011) 49-53.

[14] V. Gilsanz, J. Chalfant, A.O. Mo, D.C. Lee, F.J. Dorey, S.D. Mittelman, Reciprocal relations of subcutaneous and visceral fat to bone structure and strength, The Journal of Clinical Endocrinology & Metabolism 94(9) (2009) 3387-3393.

[15] N.K. Pollock, E. Laing, M.W. Hamrick, C. Baile, D. Hall, R. Lewis, Bone and fat relationships in postadolescent black females: a pQCT study, Osteoporosis international 22(2) (2011) 655-665.

[16] A. Janicka, T.A. Wren, M.M. Sanchez, F. Dorey, P.S. Kim, S.D. Mittelman, V. Gilsanz, Fat mass is not beneficial to bone in adolescents and young adults, The Journal of Clinical Endocrinology & Metabolism 92(1) (2007) 143-147.

[17] Y. Sheu, J.A. Cauley, The role of bone marrow and visceral fat on bone metabolism, Curr. Osteoporos. Rep. 9(2) (2011) 67-75.

[18] M. Russell, N. Mendes, K.K. Miller, C.J. Rosen, H. Lee, A. Klibanski, M. Misra, Visceral fat is a negative predictor of bone density measures in obese adolescent girls, The Journal of Clinical Endocrinology & Metabolism 95(3) (2010) 1247-1255.

[19] H.S. Choi, K.J. Kim, K.M. Kim, N.W. Hur, Y. Rhee, D.S. Han, E.J. Lee, S.-K. Lim, Relationship between visceral adiposity and bone mineral density in Korean adults, Calcified tissue international 87(3) (2010) 218-225.

[20] A. Cohen, D.W. Dempster, R.R. Recker, J.M. Lappe, H. Zhou, A. Zwahlen, R. Muller, B. Zhao, X. Guo, T. Lang, I. Saeed, X.S. Liu, X.E. Guo, S. Cremers, C.J. Rosen, E.M. Stein, T.L. Nickolas, D.J. McMahon, P. Young, E. Shane, Abdominal fat is associated with lower bone formation and inferior bone quality in healthy premenopausal women: a transiliac bone biopsy study, J Clin Endocrinol Metab 98(6) (2013) 2562-72.

[21] R. Huiskes, R. Ruimerman, G.H. van Lenthe, J.D. Janssen, Effects of mechanical forces on maintenance and adaptation of form in trabecular bone, Nature 405(6787) (2000) 704-6.

[22] L.F. Bonewald, The amazing osteocyte, J Bone Miner Res 26(2) (2011) 229-38.

[23] A.G. Robling, P.J. Niziolek, L.A. Baldridge, K.W. Condon, M.R. Allen, I. Alam, S.M. Mantila, J. Gluhak-Heinrich, T.M. Bellido, S.E. Harris, C.H. Turner, Mechanical stimulation of bone in vivo reduces osteocyte expression of Sost/sclerostin, J Biol Chem 283(9) (2008) 5866-75.

[24] L.D. You, S. Temiyasathit, P.L. Lee, C.H. Kim, P. Tummala, W. Yao, W. Kingery, A.M. Malone, R.Y. Kwon, C.R. Jacobs, Osteocytes as mechanosensors in the inhibition of bone resorption due to mechanical loading, Bone 42(1) (2008) 172-179.

[25] A. Santos, A.D. Bakker, H.M. Willems, N. Bravenboer, A.L. Bronckers, J. Klein-Nulend, Mechanical loading stimulates BMP7, but not BMP2, production by osteocytes, Calcif Tissue Int 89(4) (2011) 318-26.

[26] A. Cohen, A. Costa, R. Recker, J. Lappe, S. Cremers, D. Dempster, H. Zhou, A. Zwahlen, R. Mueller, E. Stein, Lower Bone Volume Fraction and Bone Formation Rate in Premenopausal Women with Abdominal Obesity Are Associated with Less Physical Activity and Higher Serum Sclerostin, Journal Of Bone And Mineral Research, Wiley-Blackwell 111 River St, Hoboken 07030-5774, NJ USA, 2013.

[27] G.L. Galea, A. Sunters, L.B. Meakin, G. Zaman, T. Sugiyama, L.E. Lanyon, J.S. Price, Sost down-regulation by mechanical strain in human osteoblastic cells involves PGE2 signaling via EP4, FEBS Lett 585(15) (2011) 2450-4.

[28] Elliott Goff, Federica Buccino, Chiara Bregoli, Jonathan P. McKinley, Basil Aeppli, Robert R. Recker, Elizabeth Shane, Adi Cohen, Gisela Kuhn, Ralph Müller, Large-scale quantification of human osteocyte lacunar morphological biomarkers as assessed by ultra-high-resolution desktop micro-computed tomography, Bone 152 (2021) 116094.

[29] A. Cohen, R.R. Recker, J. Lappe, D.W. Dempster, S. Cremers, D.J. McMahon, E.M. Stein, J. Fleischer, C.J. Rosen, H. Rogers, R.B. Staron, J. Lemaster, E. Shane, Premenopausal women with idiopathic low-trauma fractures and/or low bone mineral density, Osteoporos Int 23(1) (2012) 171-82.

[30] P. Ruegsegger, B. Koller, R. Muller, A microtomographic system for the nondestructive evaluation of bone architecture, Calcified Tissue International 58(1) (1996) 24-29.

[31] A. Cohen, D.W. Dempster, R. Muller, X.E. Guo, T.L. Nickolas, X.S. Liu, X.H. Zhang, A.J. Wirth, G.H. van Lenthe, T. Kohler, D.J. McMahon, H. Zhou, M.R. Rubin, J.P. Bilezikian, J.M. Lappe, R.R. Recker, E. Shane, Assessment of trabecular and cortical architecture and mechanical competence of bone by high-resolution peripheral computed tomography: comparison with transiliac bone biopsy, Osteoporosis International 21(2) (2010) 263-273.

[32] T. Hildebrand, A. Laib, R. Muller, J. Dequeker, P. Ruegsegger, Direct three-dimensional morphometric analysis of human cancellous bone: Microstructural data from spine, femur, iliac crest, and calcaneus, Journal of Bone and Mineral Research 14(7) (1999) 1167-1174.

[33] T. Hildebrand, P. Ruegsegger, Quantification of Bone Microarchitecture with the Structure Model Index, Comput Methods Biomech Biomed Engin 1(1) (1997) 15-23.

[34] M.L. Bouxsein, S.K. Boyd, B.A. Christiansen, R.E. Guldberg, K.J. Jepsen, R. Muller, Guidelines for assessment of bone microstructure in rodents using micro-computed tomography, J Bone Miner Res 25(7) (2010) 1468-86.

[35] K.S. Mader, P. Schneider, R. Muller, M. Stampanoni, A quantitative framework for the 3D characterization of the osteocyte lacunar system, Bone 57(1) (2013) 142-54.

[36] M.P. Akhter, D. Kimmel, J. Lappe, R. Recker, Effect of Macroanatomic Bone Type and Estrogen Loss on Osteocyte Lacunar Properties in Healthy Adult Women, Calcified Tissue International (2017) 1-12.

[37] Y. Carter, C.D.L. Thomas, J.G. Clement, A.G. Peele, K. Hannah, D.M.L. Cooper, Variation in osteocyte lacunar morphology and density in the human femur - a synchrotron radiation micro-CT study, Bone 52(1) (2013) 126-132.

[38] A. Carriero, M. Doube, M. Vogt, B. Busse, J. Zustin, A. Levchuk, P. Schneider, R. Muller, S.J. Shefelbine, Altered lacunar and vascular porosity in osteogenesis imperfecta mouse bone as revealed by synchrotron tomography contributes to bone fragility, Bone 61 (2014) 116-124.

[39] J.A. Kanis, L.J. Melton III, C. Christiansen, C.C. Johnston, N. Khaltaev, The diagnosis of osteoporosis, Journal of bone and mineral research 9(8) (1994) 1137-1141.

[40] G. Karaguzel, M.F. Holick, Diagnosis and treatment of osteopenia, Reviews in endocrine and metabolic disorders 11(4) (2010) 237-251.

[41] G.M. Blake, I. Fogelman, The role of DXA bone density scans in the diagnosis and treatment of osteoporosis, Postgraduate medical journal 83(982) (2007) 509-517.

[42] A. El Maghraoui, C. Roux, DXA scanning in clinical practice, QJM: An International Journal of Medicine 101(8) (2008) 605-617.

[43] T. Davis, D. Healy, A. Bubeck, R. Walker, Stress concentrations around voids in three dimensions: The roots of failure, J. Struct. Geol. 102 (2017) 193-207.

[44] A.R. Bonivtch, L.F. Bonewald, D.P. Nicolella, Tissue strain amplification at the osteocyte lacuna: a microstructural finite element analysis, Journal of biomechanics 40(10) (2007) 2199-2206.

[45] A.R. Stern, D.P. Nicolella, Measurement and estimation of osteocyte mechanical strain, Bone 54(2) (2013) 191-5.

[46] T.M. Skerry, L. Bitensky, J. Chayen, L.E. Lanyon, Early strain-related changes in enzyme activity in osteocytes following bone loading in vivo, J Bone Miner Res 4(5) (1989) 783-8.

[47] M. Mullender, S.D. Tan, L. Vico, C. Alexandre, J. Klein-Nulend, Differences in osteocyte density and bone histomorphometry between men and women and between healthy and osteoporotic subjects, Calcified tissue international 77(5) (2005) 291-296.

[48] F.M. Lambers, G. Kuhn, F.A. Schulte, K. Koch, R. Muller, Longitudinal assessment of in vivo bone dynamics in a mouse tail model of postmenopausal osteoporosis, Calcif Tissue Int 90(2) (2012) 108-19.

[49] S.D. Badilatti, P. Christen, I. Parkinson, R. Müller, Load-adaptive bone remodeling simulations reveal osteoporotic microstructural and mechanical changes in whole human vertebrae, Journal of biomechanics 49(16) (2016) 3770-3779.

Chapter 5

Synthesis

5.1. Background

According to a report from the United Nations, the population above age 65 is expected to double by 2050 with an estimated total of 1.5 billion people globally in this age range [1]. Today, women are overrepresented in this age range amounting to 55% of the global total. When considering global population above 80 years of age, women's representation rises to 62% [1]. These statistics should motivate a global refocus of current medical resources towards the elderly with a strong emphasis on women. The skeletal system undergoes a steep physiological decline with age, which disproportionately affects the elderly and often gives rise to diseases such as osteoporosis. Patients with osteoporosis have an associated increase risk of fracture, and it is estimated that an osteoporotic fracture will occur to 1 in 3 women over 50 years of age as compared to 1 in 5 men in the same age category [2]. Studies involving postmenopausal cohorts have observed osteoporotic bone to consist of fewer, thinner, and more separated trabecular struts as well as thinner cortices relative to healthy bone [3-7]. However, osteoporosis also affects younger subjects, and the disease is broadly described as a disruption of the remodeling process, ultimately leading to fragile bone [8]. Rare forms of osteoporosis, including idiopathic osteoporosis (IOP), have been observed in younger, premenopausal, women. IOP is characterized by low bone mineral density (BMD) combined with a history of adult low trauma fracture(s) and has an estimated incidence rate of 2828/year [9, 10]. Formally considered to be an orphan disease (prevalence fewer than 200,000), relatively few studies have characterized bone from IOP patients [11-13]. Therefore, the goal of this thesis was to investigate the tissue and cellular micro-architecture of IOP bone to better understand the disease and propose biomarkers that could potentially differentiate between IOP and healthy bone.

Bone tissue is continuously remodeled, and the process is inextricably linked with the mechanical environment in which it is immersed [14-16]. Regions which are highly loaded form additional bone while the organ adapts its lowly loaded regions by removing bone [17, 18]. This delicate orchestration is primarily conducted by the osteocytes – a densely connected network of cells embedded within the bone tissue matrix that are sensitive to their mechanical environment [19, 20] [20, 21]. Each osteocyte resides within an individual lacunar structure, which mimics the geometry of the osteocyte and can be roughly estimated as an ellipsoid. Lacunae are typically between 10 and 20 micrometers in diameter, and their resident osteocytes

are connected through dendritic processes within canalicular sheaths, which together comprise the osteocyte lacunar-canalicular network (LCN) [22-24]. Because the morphology of the lacuna is related to the ensconced osteocyte and remains intact after cell death, the lacuna is an ideal structure to designate as a biomarker. Additionally, a wide variety of high-resolution imaging techniques are available to capture lacunar morphology as it is not dependent on osteocyte viability and can be imaged ex-vivo.

Therefore, the first part of this thesis, chapter 3, aimed to develop and validate an imaging methodology to perform large-scale quantification of osteocyte lacunar morphologies. Based on morphological indices from a similar previous study [25], a methodology using desktop micro-computed tomography (microCT) was created to image lacunae on a large scale. The validation of this method included measures of accuracy, reproducibility, and sensitivity relative to the segmented lacunar structures. These lacunar structures were examined again in the final section of this first chapter using micro-finite element (microFE) modeling to explore the mechanical relationship between lacunae and microcracking. Two microFE models were created based on previously published computational models [26] and experimental results [27, 28].

The second part of this thesis, chapter 4, aimed to apply the lacunar imaging methodology developed in chapter 3 to a large set of clinically relevant biopsies. This set of 103 transiliac biopsies included idiopathic osteoporosis (IOP, n=45), idiopathic low bone mineral density (ILBMD, n=19), and healthy cohorts (n=39). As lacunar morphometric parameters have been shown to significantly differ (i.e. lacunar density decreases) between aged postmenopausal osteoporotic subjects and control subjects [29-32], it was important to examine the differences between younger premenopausal osteoporotic subjects (IOP) and control subjects to see if this effect persisted. This research direction was further supported by several previous studies that discovered tissue level morphometric differences between these two cohorts [11-13]. Finally, an additional goal of this chapter was to investigate the relationship between lacunar morphometric parameters and adiposity in the control cohort. Again, tissue-level differences have been previously identified [33] and hence it was important to compare lacunar morphologies just as we had in the first part of this chapter to better understand if these differences also existed at the cellular level.

5.2 Main findings and implications

To the best of our knowledge, this was the first study to measure lacunar morphology in human biopsies on a large scale using desktop microCT. We reported global, local, and population-based lacunar morphometries following along and expanding upon previously defined lacunar metrics [25, 34-41]. Resulting lacunar morphometries were comparable with previous studies [42], and the general shape was also in line with animal studies that used other imaging technologies such as SR-CT and CLSM [25, 43].

Rigorous validation of our imaging method was important and was also a key achievement in this chapter. We calculated accuracy by manually comparing machine-identified lacunar structures with human-identified lacunar structures in 2D and 3D images. Ultimately we were able to achieve rates of true positives (TP), false positives (FP), and false negatives (FN) that were in the same acceptable range as in previous lacunar studies [44]. With respect to the reproducibility of our imaging method, we calculated both precision errors (PE) and intraclass correlation coefficients (ICC). The values for PE and ICC were low and high, respectively, and were also in the same range as reported by a previous study that used desktop microCT to investigate murine lacunae [45]. Finally, the sensitivity with respect to biological differences was evaluated by comparing known differences between lacunar morphologies from cortical and trabecular regions [42, 46, 47]. Our successful sensitivity analysis was based on the vascular imaging analysis conducted by Nebuloni et al. in which they also defined sensitivity as the ability to detect known biological differences [48]. Currently, Akhter et al. have published the only study comparing lacunar morphometries between cortical and trabecular bone in human iliac crest biopsies [42]. Our findings differed from theirs in that we reported higher lacunar density (Lc.N/BV) and porosity (Lc.TV/BV) in cortical bone compared with trabecular bone [49]. Yet, Akhter et al. were only able to analyze 72 thousand lacunae compared with our truly large-scale analysis of 7.7 million lacunae (chapter 3), giving our analysis added weight. Furthermore, we were able to uncover significant differences between both local <Lc.V>, <Lc.S> and population-based [Lc.St], [Lc.Sr] lacunar morphometric parameters between cortical and trabecular regions.

Another strength is that we chose to develop our imaging method using microCT: a mature technology that has been used to image bone for decades [50-53]. Consequently, microCT systems are widely available in laboratories throughout the world, making the technology

accessible to many researchers. As we demonstrate in this chapter, newer microCT systems are capable of imaging complete bone biopsies with a resolution on the order of one micrometer with an acceptable image quality. This provides a reasonable balance between CLSM imaging technology, which is unable to scale beyond a few hundred lacunae, and SR-CT, which is a scarce resource with limited availability on the order of several hours per year, depending on the capacity at the beamline facility.

The final important finding in chapter 3 was with respect to our computational modeling of microcracking in bone. Of the two models we proposed, the scissor model (SM) simulated the behavior of microcrack progression through bone most realistically. Just as previous experimental studies have established [27, 28], our simulated microcracks also typically initiated at a large canal, propagated parallel to the applied compression, and were guided by lacunar pores. While our model was based on a previous computational approach of microcrack progression in a binarized image of murine bone governed by stress gradients [54], we imaged human bone and included the natural mineralization patterns of the heterogeneous bone matrix by translating the density of each image voxel into an element of corresponding stiffness based on a previously published relationship by Morgan et al. [55]. Although more computationally intensive, this produced a more realistic microcrack progression, which was comparable to experimental results [27, 28] and was based on the true heterogeneous nature of the tissue, canal, and lacunar structures. Furthermore, our SM approach included an approximation of the canalicular network by incorporating a conditional statement into the model: when the microcrack was within 21 voxels of a lacunar structure, the nearby canalicular connections would be assumed to be damaged or severed, thus releasing the interstitial fluid, and ultimately softening the lacunae in proximity. We observed in our simulations that the microcrack would indeed follow the path towards and through the “empty” lacunae as compared with the “full” lacunae. Although our image resolution was not enough to resolve these canalicular structures, our SM illustrated the importance of mechanics within the lacunar structures as well as the surrounding perilacunar matrix with respect to microcrack progression. Our modeled microcrack behavior and interaction with lacunar structures are important steps towards the creation of future mechanical lacunar biomarkers.

Applying our validated imaging method to a large set of clinically relevant transiliac biopsies in chapter 4 was another major achievement of this thesis. In total, we imaged 26.2 million lacunae in 103 human biopsies with respect to IOP (n=45), ILBMD (n=19), and control (n=39)

cohorts. For each lacunar structure, we measured morphometric parameters: lacunar density (Lc.N/BV), lacunar porosity (Lc.TV/BV), lacunar number (Lc.N), lacunar volume (Lc.V), lacunar surface area (Lc.S), lacunar alignment (Lc.θ), lacunar stretch (Lc.St), lacunar oblateness (Lc.Ob), lacunar equancy (Lc.Eq), and lacunar sphericity (Lc.Sr). This was the first study to elucidate differences in lacunar morphometric parameters (Lc.N/BV, Lc.V, Lc.Sr) between cortical and trabecular bone with respect to these three specific cohorts. Our results in this chapter corroborated our findings in the previous chapter (Lc.N/BV higher in cortical bone), which remain at odds with the findings of the smaller study performed by Akhter et al. (Lc.N/BV higher in trabecular bone). Our study was also the first to illustrate an extremely strong correlation between Lc.Sr and BV/TV, which is particularly noteworthy since BV/TV is the main morphometric parameter that clinicians use to diagnose osteoporosis [56-59]. Furthermore, calculating Lc.Sr also allowed us to create a rough comparison of lacunar shape between our study and a previous materials study [60] that equated a variety of pore geometries with a range of mechanics. For example, pores with spherical geometries have been shown to experience roughly double the hoop stress as compared with prolate ellipsoids [60]. We extended this logic to our lacunar structures which also consist of an approximate range of spheres to prolate ellipsoids. This allowed us to hypothesize that spherical lacunae could be indicative of highly mechanosensitive resident osteocytes, which supports the strong negative correlation we found between Lc.Sr and BV/TV as well as being in line with previous studies that highlight the importance of lacunar stress amplification on osteocyte cellular signaling [61-63]. Finally, we discovered that the lacunar morphologies in general were extremely similar between IOP, ILBMD, and control cohorts. This was an important finding because while we originally set out to use lacunae as biomarkers to differentiate between these cohorts, our data indicate that perhaps osteocytes function normally even in diseased or mechanically compromised bone. This finding extended to the final analysis in this chapter, which illustrated that lacunar morphologies were also indifferentiable between biopsies with varying levels of adiposity.

5.3 Limitations and future research

With respect to our imaging methodology in chapter 3, there are several important limitations that must be acknowledged. While our landmark-based threshold approach for lacunar segmentation provided an acceptable level of accuracy, which was in line with similar studies that segmented lacunae with a threshold offset [44], we still were not able to include all lacunar structures in our analysis nor omit all non-lacunar structures from it. This was unfortunately an inherent problem of our approach in choosing a single threshold for lacunar identification. We explored a multiple threshold approach using a watershed method [64] to include lacunae with density values slightly above and below our selected single threshold, however, we concluded there was no significant improvement over our single landmark-based threshold approach. It would be interesting to explore machine-learning approaches such as convoluted neural networks (CNN), which have shown remarkable success in automated machine detection in images involving landmarks used for diagnosing breast cancer [65].

False inclusion and exclusion of lacunar structures also stemmed from the volumetric size range we chose to include in our analysis. Lacunar volume range has been shown to vary substantially with some studies declaring it as narrow as 50-610μm^3 while others as wide as 175-2000μm^3 [22, 25, 35, 42, 66, 67]. We chose a wide volumetric range (50μm^3 – 2000μm^3) for maximum inclusion, yet the problems we encountered with our selection existed around the 50μm^3 lower limit due to several factors: the limited 1.2 micrometer resolution of our desktop microCT system, resulting inclusion of partial volume effects, and the inherent difficulties associated with a relatively low-photon-count x-ray beam. Compared with SR-CT studies [22, 25], image projections from desktop microCT are created with fewer photons, leading to additional image noise and ultimately making small lacunae difficult to visualize. It will be important in future studies to image the same biopsy in both desktop microCT and SR-CT systems to compare the lacunar structures at 50μm^3 and below to characterize and perhaps even eliminate the noise that is introduced with desktop microCT. Furthermore, we only calculated the accuracy of lacunar identification and did not address the accuracy of lacunar segmentation. This is another direction that should be investigated in a future study comparing lacunar images between desktop microCT and a higher resolution imaging technology such as SR-CT.

Another limitation from chapter 3 was that our imaging method was only validated for trabecular bone and has not yet been validated for cortical bone. Because cortical bone is denser

than trabecular bone, it is likely that beam-hardening effects were included in our images of cortical bone and consequently affected the image quality. While not detrimental to our study, perhaps imaging cortical bone in the future with a higher beam energy could ameliorate some of the beam-hardening effects. Ultimately, it will be important in future desktop microCT lacunar studies to quantify these differences, calibrate accordingly, and validate the resulting images. Finally, we must reiterate the fact that our imaging method was only optimized and validated for human transiliac biopsies of young premenopausal women. If our method is to be applied to different cohorts or biopsy sites, it will be imperative for these future studies to optimize and validate accordingly.

Our microcrack modeling approaches in the second part of chapter 3 also included several shortcomings. While the main goal of our microFE models was to create lacunar mechanical biomarkers to apply to our diseased and control cohorts in chapter 4, we were only able to identify directions towards developing lacunar mechanical biomarkers. This was in part due to the complexity of our models. Our approach was to create microFE models to simulate microcracking in bone, and then to identify the mechanical patterns around lacunae through which the microcrack propagated. However, the computational time required for each simulation was on the order of weeks, due to the inability to parallelize the simulation code since each iteration was dependent on the previous. This resulted in very few lacunae connecting with the microcrack, and ultimately an inability to generalize the surrounding lacunar mechanics into a succinct biomarker. Cellular automata approaches have a wide variety of applications [68] and could be a viable avenue to reduce the complexity of the model while maintaining the behavior and should be investigated in future studies as a means of model simplification.

We explored an additional model (SM) to compare with our first model (MGM), which included the canalicular structures and the theoretical release of fluid pressure when they were severed by the microcrack. While the microcrack appeared to be more similar to the experimental work from Voide et al. [27, 28], it was also difficult to deduce if the microcrack was truly attracted to specific “empty” lacunae and if so, how their mechanical nature should be captured. One possible direction for a future experiment would be to evaluate the stiffness gradient or stress concentrations in the immediate vicinity of lacunae connected with the microcrack and create a scalar value to describe it. This would also require the crack to be simulated in a larger volume where more than only one or two lacunae intersect the

microcrack's path as we observed in our approach. Furthermore, our analysis was limited as we only simulated microcracking on a subregion of a single biopsy image. We attempted to maneuver around this problem by performing multiple simulations on rotated versions of the single image; however, the same vascular canal and many similar lacunae were included in each simulation which substantially limited the variability that could be included in the behavior of the microcrack propagation.

Chapter 4, which demonstrates the application of our imaging method to clinical studies, also includes several limitations and possible directions for future experiments that are important to discuss. Our original goal was to use the lacunar morphometric parameters defined in the first part of chapter 3 to differentiate between diseased and control human biopsies. Yet, we pursued this avenue only to discover that our lacunar morphological biomarkers, while exposing differences between cortical and trabecular regions, were remarkably similar between healthy and diseased cohorts. We discovered important relationships between tissue parameters (BV/TV) and lacunar parameters (Lc.Sr) across all cohorts, which contains important implications for the lacunar structure as a biomarker from a mechanobiological perspective, yet not from a disease perspective as we anticipated. However, our inability to differentiate between disease and control subjects may be related to the specific disease we investigated. While lacunar morphology did not differ between control, IOP, and ILBMD cohorts, it could potentially change more substantially in other disease cohorts and will be important for future studies to investigate this [69-72]. Furthermore, the iliac crest biopsy site was not ideal since the directionality of the mechanical load on the ilium is complex and typically lower relative to sites such as the femur and tibia. Investigations of additional biopsy sites would behoove further researchers.

The second limitation of this chapter is the fact that our study was cross-sectional, and that longitudinal data were not available. Because our analysis was based upon a single time-point, it was impossible to address the causal directionality of lacunar remodeling. It was equally possible that osteocytes remodeled their direct environment to compensate for a reduction in bone quality and that the reduction in bone quality was driven by lacunar remodeling. This will be an important topic to address in future studies with improved computer simulations and longitudinal datasets [73, 74].

The final part of chapter 4 applied the same analysis as the first part but instead compared between tertiles of the control cohort based on rates of adiposity. Therefore, many of the same

limitations we encountered when comparing lacunae between IOP, ILBMD, and control cohorts also appeared here including the important fact that this, too, was a cross-sectional study. Yet, a limitation unique to this analysis occurred relative to the grouping of adiposity. In line with a previous study on this cohort [33], we created three equal groups that equated to low, middle, and high rates of adiposity. However, these groupings were defined only to maintain equal sample sizes and did not connect with a larger context of adiposity rates across entire populations of women. Recruiting a cohort of women based on rates of adiposity and analyzing their lacunar morphology would be an important study to conduct in the future and would give a broader context to adiposity beyond our limited group of 39 women.

5.4 Conclusion

In conclusion, the approach to analyze lacunar morphology on a large scale using ultra-high-resolution desktop microCT was successful. Since this was a novel approach, rigorous validation was required and reported high levels of accuracy, reproducibility, and sensitivity. By implementing this approach on human iliac crest bone biopsies, lacunar morphological differences between cortical and trabecular regions were uncovered, providing evidence that the lacunar shape is related to the type of bone it inhabits. From another perspective, the biomechanical importance of lacunar morphology was evaluated by creating two computational models, which simulated microcrack progression and propagation through lacunar pores. In the latter half of the thesis, this large-scale lacunar analysis methodology was successfully applied to clinically relevant bone biopsies to better understand rare bone diseases and how they relate to healthy subjects. Finally, the methodology was applied to a subgroup of healthy subjects to evaluate the relationship between adiposity and lacunar morphology. While lacunar morphology in healthy subjects did not differ significantly from affected subjects nor between healthy subjects with different rates of adiposity, the reported findings provide substantial evidence that lacunar morphology is not altered in IOP or ILBMD subjects relative to healthy subjects, nor with respect to adiposity within healthy subjects. However, it is also important to highlight the possibility that lacunar morphological differences may yet exist in cohorts with other pathologies, and future studies must investigate this possibility. Furthermore, the strong correlation between lacunar sphericity and BV/TV indicates a profound mechanobiological link between the cell and tissue spatial scales and must be further examined in future longitudinal studies.

References

[1] U. Nations, World Population Ageing 2020 (ST/ESA/SER. A/444), Department of Economic and Social Affairs, Population Division. New York, USA (2021).

[2] T. Sözen, L. Özışık, N.Ç. Başaran, An overview and management of osteoporosis, European journal of rheumatology 4(1) (2017) 46.

[3] A.M. Parfitt, C.H.E. Mathews, A.R. Villanueva, M. Kleerekoper, B. Frame, D.S. Rao, Relationships Between Surface, Volume, And Thickness Of Iliac Trabecular Bone In Aging And In Osteoporosis - Implications For The Microanatomic And Cellular Mechanisms Of Bone Loss, J. Clin. Invest. 72(4) (1983) 1396-1409.

[4] E. Legrand, D. Chappard, C. Pascaretti, M. Duquenne, S. Krebs, V. Rohmer, M.F. Basle, M. Audran, Trabecular bone microarchitecture, bone mineral density, and vertebral fractures in male osteoporosis, Journal of Bone and Mineral Research 15(1) (2000) 13-19.

[5] S. Majumdar, H. Genant, S. Grampp, D. Newitt, V.H. Truong, J. Lin, A. Mathur, Correlation of trabecular bone structure with age, bone mineral density, and osteoporotic status: in vivo studies in the distal radius using high resolution magnetic resonance imaging, Journal of Bone and Mineral Research 12(1) (1997) 111-118.

[6] H. Ritzel, M. Amling, M. Pösl, M. Hahn, G. Delling, The thickness of human vertebral cortical bone and its changes in aging and osteoporosis: A histomorphometric analysis of the complete spinal column from thirty-seven autopsy specimens, Journal of Bone and Mineral Research 12(1) (1997) 89-95.

[7] D. Hans, A.L. Goertzen, M.A. Krieg, W.D. Leslie, Bone microarchitecture assessed by TBS predicts osteoporotic fractures independent of bone density: the Manitoba study, Journal of Bone and Mineral Research 26(11) (2011) 2762-2769.

[8] J.A. Kanis, L.J. Melton, C. Christiansen, C.C. Johnston, N. Khaltaev, Perspective - The Diagnosis of Osteoporosis, Journal of Bone and Mineral Research 9(8) (1994) 1137-1141.

[9] S. Khosla, E.G. Lufkin, S.F. Hodgson, L.A. Fitzpatrick, L.J. Melton, Epidemiology and clinical features of osteoporosis in young individuals, Bone 15(5) (1994) 551-555.

[10] U.S.B.o.t. Census, Census 2010, U.S. Government Printing Office, Washington, DC, 2010.

[11] A. Cohen, D.W. Dempster, R.R. Recker, E.M. Stein, J.M. Lappe, H. Zhou, A.J. Wirth, G.H. van Lenthe, T. Kohler, A. Zwahlen, R. Muller, C.J. Rosen, S. Cremers, T.L. Nickolas, D.J. McMahon, H. Rogers, R.B. Staron, J. LeMaster, E. Shane, Abnormal bone microarchitecture and evidence of osteoblast dysfunction in premenopausal women with idiopathic osteoporosis, J Clin Endocrinol Metab 96(10) (2011) 3095-105.

[12] A. Cohen, X.S. Liu, E.M. Stein, D.J. McMahon, H.F. Rogers, J. LeMaster, R.R. Recker, J.M. Lappe, X.E. Guo, E. Shane, Bone Microarchitecture and Stiffness in Premenopausal Women with Idiopathic Osteoporosis, J. Clin. Endocrinol. Metab. 94(11) (2009) 4351-4360.

[13] A. Cohen, R.R. Recker, J. Lappe, D.W. Dempster, S. Cremers, D.J. McMahon, E.M. Stein, J. Fleischer, C.J. Rosen, H. Rogers, R.B. Staron, J. Lemaster, E. Shane, Premenopausal women with idiopathic low-trauma fractures and/or low bone mineral density, Osteoporos Int 23(1) (2012) 171-82.

[14] J. Wolff, Das Gesetz der Transformation der Knochen, DMW-Deutsche Medizinische Wochenschrift 19(47) (1892) 1222-1224.

[15] W. Roux, Der Kampf der Theile im Organismus: ein Beitrag zur Vervollständigung der mechanischen Zweckmässigkeitslehre, W. Engelmann1881.

[16] J.Y. Rho, L. Kuhn-Spearing, P. Zioupos, Mechanical properties and the hierarchical structure of bone, Med. Eng. Phys. 20(2) (1998) 92-102.

[17] H.M. Frost, Bone "mass" and the "mechanostat": a proposal, Anat Rec 219(1) (1987) 1-9.

[18] R. Huiskes, R. Ruimerman, G.H. van Lenthe, J.D. Janssen, Effects of mechanical forces on maintenance and adaptation of form in trabecular bone, Nature 405(6787) (2000) 704-6.

[19] S.L. Dallas, M. Prideaux, L.F. Bonewald, The osteocyte: an endocrine cell ... and more, Endocr Rev 34(5) (2013) 658-90.

[20] L.F. Bonewald, The amazing osteocyte, J Bone Miner Res 26(2) (2011) 229-38.

[21] L. Lanyon, Osteocytes, strain detection, bone modeling and remodeling, Calcified tissue international 53(1) (1993) S102-S107.

[22] F.L. Bach-Gansmo, A. Bruel, M.V. Jensen, E.N. Ebbesen, H. Birkedal, J.S. Thomsen, Osteocyte lacunar properties and cortical microstructure in human iliac crest as a function of age and sex, Bone 91 (2016) 11-19.

[23] P. Dong, S. Haupert, B. Hesse, M. Langer, P.J. Gouttenoire, V. Bousson, F. Peyrin, 3D osteocyte lacunar morphometric properties and distributions in human femoral cortical bone using synchrotron radiation micro-CT images, Bone 60 (2014) 172-185.

[24] H. Kamioka, T. Honjo, T. Takano-Yamamoto, A three-dimensional distribution of osteocyte processes revealed by the combination of confocal laser scanning microscopy and differential interference contrast microscopy, Bone 28(2) (2001) 145-9.

[25] K.S. Mader, P. Schneider, R. Muller, M. Stampanoni, A quantitative framework for the 3D characterization of the osteocyte lacunar system, Bone 57(1) (2013) 142-54.

[26] F. Donaldson, D. Ruffoni, P. Schneider, A. Levchuk, A. Zwahlen, P. Pankaj, R. Muller, Modeling microdamage behavior of cortical bone, Biomech Model Mechanobiol 13(6) (2014) 1227-42.

[27] R. Voide, P. Schneider, M. Stauber, G.H. van Lenthe, M. Stampanoni, R. Muller, The importance of murine cortical bone microstructure for microcrack initiation and propagation, Bone 49(6) (2011) 1186-93.

[28] R. Voide, P. Schneider, M. Stauber, R. Wyss, M. Stampanoni, U. Sennhauser, G.H. van Lenthe, R. Muller, Time-lapsed assessment of microcrack initiation and propagation in murine cortical bone at submicrometer resolution, Bone 45(2) (2009) 164-173.

[29] S. Mori, R. Harruff, W. Ambrosius, D. Burr, Trabecular bone volume and microdamage accumulation in the femoral heads of women with and without femoral neck fractures, Bone 21(6) (1997) 521-526.

[30] M. Mullender, D. Van der Meer, R. Huiskes, P. Lips, Osteocyte density changes in aging and osteoporosis, Bone 18(2) (1996) 109-113.

[31] S. Qiu, D. Rao, S. Palnitkar, A. Parfitt, Age and distance from the surface but not menopause reduce osteocyte density in human cancellous bone, Bone 31(2) (2002) 313-318.

[32] D. Vashishth, O. Verborgt, G. Divine, M.B. Schaffler, D.P. Fyhrie, Decline in osteocyte lacunar density in human cortical bone is associated with accumulation of microcracks with age, Bone 26(4) (2000) 375-380.

[33] A. Cohen, D.W. Dempster, R.R. Recker, J.M. Lappe, H. Zhou, A. Zwahlen, R. Muller, B. Zhao, X. Guo, T. Lang, I. Saeed, X.S. Liu, X.E. Guo, S. Cremers, C.J. Rosen, E.M. Stein, T.L. Nickolas, D.J. McMahon, P. Young, E. Shane, Abdominal fat is associated with lower bone formation and inferior bone quality in healthy premenopausal women: a transiliac bone biopsy study, J Clin Endocrinol Metab 98(6) (2013) 2562-72.

[34] H.M. Britz, Y. Carter, J. Jokihaara, O.V. Leppanen, T.L.N. Jarvinen, G. Belev, D.M.L. Cooper, Prolonged unloading in growing rats reduces cortical osteocyte lacunar density and volume in the distal tibia, Bone 51(5) (2012) 913-919.

[35] Y. Carter, C.D.L. Thomas, J.G. Clement, A.G. Peele, K. Hannah, D.M.L. Cooper, Variation in osteocyte lacunar morphology and density in the human femur - a synchrotron radiation micro-CT study, Bone 52(1) (2013) 126-132.

[36] P. Schneider, M. Stauber, R. Voide, M. Stampanoni, L.R. Donahue, R. Muller, Ultrastructural properties in cortical bone vary greatly in two inbred strains of mice as assessed by synchrotron light based micro- and Nano-CT, Journal of Bone and Mineral Research 22(10) (2007) 1557-1570.

[37] Y. Sugawara, H. Kamioka, T. Honjo, K. Tezuka, T. Takano-Yamamoto, Three-dimensional reconstruction of chick calvarial osteocytes and their cell processes using confocal microscopy, Bone 36(5) (2005) 877-883.

[38] R.P. van Hove, P.A. Nolte, A. Vatsa, C.M. Semeins, P.L. Salmon, T.H. Smit, J. Klein-Nulend, Osteocyte morphology in human tibiae of different bone pathologies with different bone mineral density - Is there a role for mechanosensing?, Bone 45(2) (2009) 321-329.

[39] A. Vatsa, R.G. Breuls, C.M. Semeins, P.L. Salmon, T.H. Smit, J. Klein-Nulend, Osteocyte morphology in fibula and calvaria - Is there a role for mechanosensing?, Bone 43(3) (2008) 452-458.

[40] S. Suniaga, T. Rolvien, A. vom Scheidt, I.A.K. Fiedler, H.A. Bale, A. Huysseune, P.E. Witten, M. Amling, B. Busse, Increased mechanical loading through controlled swimming exercise induces bone formation and mineralization in adult zebrafish, Sci Rep 8 (2018) 13.

[41] B. Ay, K. Parolia, R.S. Liddell, Y.S. Qiu, G. Grasselli, D.M.L. Cooper, J.E. Davies, Hyperglycemia compromises Rat Cortical Bone by Increasing Osteocyte Lacunar Density and Decreasing Vascular Canal Volume, Commun. Biol. 3(1) (2020) 9.

[42] M.P. Akhter, D. Kimmel, J. Lappe, R. Recker, Effect of Macroanatomic Bone Type and Estrogen Loss on Osteocyte Lacunar Properties in Healthy Adult Women, Calcified Tissue International (2017) 1-12.

[43] C.M. Heveran, A. Rauff, K.B. King, R.D. Carpenter, V.L. Ferguson, A new open-source tool for measuring 3D osteocyte lacunar geometries from confocal laser scanning microscopy reveals age-related changes to lacunar size and shape in cortical mouse bone, Bone 110 (2018) 115-127.

[44] E.N. Cresswell, T.M. Nguyen, M.W. Horsfield, A.J. Alepuz, T.A. Metzger, G.L. Niebur, C.J. Hernandez, Mechanically induced bone formation is not sensitive to local osteocyte density in rat vertebral cancellous bone, J Orthop Res (2017).

[45] H. Hemmatian, M.R. Laurent, S. Ghazanfari, D. Vanderschueren, A.D. Bakker, J. Klein-Nulend, G.H. van Lenthe, Accuracy and reproducibility of mouse cortical bone microporosity as quantified by desktop microcomputed tomography, Plos One 12(8) (2017).

[46] P. Milovanovic, B. Busse, Inter-site Variability of the Human Osteocyte Lacunar Network: Implications for Bone Quality, Curr Osteoporos Rep (2019).

[47] C.D. Kegelman, J.C. Coulombe, K.M. Jordan, D.J. Horan, L. Qin, A.G. Robling, V.L. Ferguson, T.M. Bellido, J.D. Boerckel, YAP and TAZ Mediate Osteocyte Perilacunar/Canalicular Remodeling, J Bone Miner Res 35(1) (2020) 196-210.

[48] L. Nebuloni, G.A. Kuhn, J. Vogel, R. Muller, A Novel In Vivo Vascular Imaging Approach for Hierarchical Quantification of Vasculature Using Contrast Enhanced Micro-Computed Tomography, Plos One 9(1) (2014) 10.

[49] Elliott Goff, Federica Buccino, Chiara Bregoli, Jonathan P. McKinley, Basil Aeppli, Robert R. Recker, Elizabeth Shane, Adi Cohen, Gisela Kuhn, Ralph Müller, Large-scale quantification of human osteocyte lacunar morphological biomarkers as assessed by ultra-high-resolution desktop micro-computed tomography, Bone 152 (2021) 116094.

[50] L.P. Bakalova, C.M. Andreasen, J.S. Thomsen, A. Bruel, E.M. Hauge, B.J. Kiil, J.M. Delaisse, T.L. Andersen, D.M. Ph, Relating Intracortical Bone Mechanics to Pore Morphology and Remodeling Characteristics in the Human Fibula, J Bone Miner Res (2018).

[51] M.L. Bouxsein, S.K. Boyd, B.A. Christiansen, R.E. Guldberg, K.J. Jepsen, R. Muller, Guidelines for Assessment of Bone Microstructure in Rodents Using Micro-Computed Tomography, Journal of Bone and Mineral Research 25(7) (2010) 1468-1486.

[52] T. Hildebrand, A. Laib, R. Muller, J. Dequeker, P. Ruegsegger, Direct three-dimensional morphometric analysis of human cancellous bone: Microstructural data from spine, femur, iliac crest, and calcaneus, Journal of Bone and Mineral Research 14(7) (1999) 1167-1174.

[53] R. Muller, H. Van Campenhout, B. Van Damme, G. Van Der Perre, J. Dequeker, T. Hildebrand, P. Ruegsegger, Morphometric analysis of human bone biopsies: A quantitative structural comparison of histological sections and micro-computed tomography, Bone 23(1) (1998) 59-66.

[54] E.F. Morgan, T.M. Keaveny, Dependence of yield strain of human trabecular bone on anatomic site, Journal of biomechanics 34(5) (2001) 569-577.

[55] E.F. Morgan, H.H. Bayraktar, T.M. Keaveny, Trabecular bone modulus-density relationships depend on anatomic site, Journal of Biomechanics 36(7) (2003) 897-904.

[56] J.A. Kanis, L.J. Melton III, C. Christiansen, C.C. Johnston, N. Khaltaev, The diagnosis of osteoporosis, Journal of bone and mineral research 9(8) (1994) 1137-1141.

[57] G. Karaguzel, M.F. Holick, Diagnosis and treatment of osteopenia, Reviews in endocrine and metabolic disorders 11(4) (2010) 237-251.

[58] G.M. Blake, I. Fogelman, The role of DXA bone density scans in the diagnosis and treatment of osteoporosis, Postgraduate medical journal 83(982) (2007) 509-517.

[59] A. El Maghraoui, C. Roux, DXA scanning in clinical practice, QJM: An International Journal of Medicine 101(8) (2008) 605-617.

[60] T. Davis, D. Healy, A. Bubeck, R. Walker, Stress concentrations around voids in three dimensions: The roots of failure, J. Struct. Geol. 102 (2017) 193-207.

[61] T.M. Skerry, L. Bitensky, J. Chayen, L.E. Lanyon, Early strain-related changes in enzyme activity in osteocytes following bone loading in vivo, J Bone Miner Res 4(5) (1989) 783-8.

[62] A.R. Bonivtch, L.F. Bonewald, D.P. Nicolella, Tissue strain amplification at the osteocyte lacuna: a microstructural finite element analysis, Journal of biomechanics 40(10) (2007) 2199-2206.

[63] A.R. Stern, D.P. Nicolella, Measurement and estimation of osteocyte mechanical strain, Bone 54(2) (2013) 191-5.

[64] E.G. D. Betts, M. Casanova, Z. Li, P. Christen and R. Müller, Segmentation of osteocyte lacuna within ultra-high resolution desktop micro-CT images: sensitivity and precision reveal issues with current state of the art, 21st International Bone Densitometry Workshop (IBDW) and the 7th European Symposium on Ultrasonic Characterization of Bone (ESUCB), Banz (Germany), 2017, p. 98.

[65] J.R. Burt, N. Torosdagli, N. Khosravan, H. RaviPrakash, A. Mortazi, F. Tissavirasingham, S. Hussein, U. Bagci, Deep learning beyond cats and dogs: recent advances in diagnosing breast cancer with deep neural networks, The British journal of radiology 91(1089) (2018) 20170545.

[66] A. Levchuk, P. Schneider, M. Meier, P. Vogel, F. Donaldson, R. Muller, An Automated Step-Wise Micro-Compression Device for 3D Dynamic Image-Guided Failure Assessment of Bone Tissue on a Microstructural Level Using Time-Lapsed Tomography, Frontiers in Materials 5 (2018) 14.

[67] S.M. Tommasini, A. Trinward, A.S. Acerbo, F. De Carlo, L.M. Miller, S. Judex, Changes in intracortical microporosities induced by pharmaceutical treatment of osteoporosis as detected by high resolution micro-CT, Bone 50(3) (2012) 596-604.

[68] S. Wolfram, Cellular automata as models of complexity, Nature 311(5985) (1984) 419-424.

[69] L. Karim, J. Moulton, M. Van Vliet, K. Velie, A. Robbins, F. Malekipour, A. Abdeen, D. Ayres, M.L. Bouxsein, Bone microarchitecture, biomechanical properties, and advanced glycation end-products in the proximal femur of adults with type 2 diabetes, Bone 114 (2018) 32-39.

[70] J.R. Furst, L.C. Bandeira, W.W. Fan, S. Agarwal, K.K. Nishiyama, D.J. McMahon, E. Dworakowski, H. Jiang, S.J. Silverberg, M.R. Rubin, Advanced Glycation Endproducts and Bone Material Strength in Type 2 Diabetes, J Clin Endocrinol Metab 101(6) (2016) 2502-10.

[71] T. Rodic, E.M. Wölfel, P. Milovanovic, I.A. Fiedler, D. Cvetkovic, K. Jähn, M. Amling, J. Sopta, S. Nikolic, V. Zivkovic, Bone quality analysis of jaw bones in individuals with type 2 diabetes mellitus—post mortem anatomical and microstructural evaluation, Clinical Oral Investigations (2021) 1-24.

[72] B. Hesse, M. Langer, P. Varga, A. Pacureanu, P. Dong, S. Schrof, N. Männicke, H. Suhonen, C. Olivier, P. Maurer, Alterations of mass density and 3D osteocyte lacunar properties in bisphosphonate-related osteonecrotic human jaw bone, a synchrotron µCT study, PloS one 9(2) (2014) e88481.

[73] F.M. Lambers, G. Kuhn, F.A. Schulte, K. Koch, R. Muller, Longitudinal assessment of in vivo bone dynamics in a mouse tail model of postmenopausal osteoporosis, Calcif Tissue Int 90(2) (2012) 108-19.

[74] S.D. Badilatti, P. Christen, I. Parkinson, R. Müller, Load-adaptive bone remodeling simulations reveal osteoporotic microstructural and mechanical changes in whole human vertebrae, Journal of biomechanics 49(16) (2016) 3770-3779.